STUDY OF DOMAIN WALL DEVICES IN MAGNETIC NANOWIRES

KULOTHUNGASAGARAN NARAYANAPILLAI
(B.Eng. (Hons.), Multimedia University, Malaysia)

A THESIS SUBMITTED FOR THE DEGREE OF DOCTOR OF PHILOSOPHY

DEPARTMENT OF ELECTRICAL AND COMPUTER ENGINEERING

NATIONAL UNIVERSITY OF SINGAPORE
2013

DECLARATION

I hereby declare that the thesis is my original work and it has been written by me in its entirety. I have duly acknowledged all the sources of information which have been used in the thesis.

This thesis has also not been submitted for any degree in any university previously.

Kulothungasagaran Narayanapillai
August 6, 2013

ACKNOWLEDGEMENTS

I would like to take this opportunity to thank everyone who made this work possible. First and foremost, I would like to express my utmost gratitude to my mentor and supervisor, Prof. Hyunsoo Yang, for giving me this wonderful opportunity to be part of his multidisciplinary research team. Throughout the last four years of my study period, his continuous guidance, encouragement and kind support have greatly shaped me into what I am today. In fact, I am quite lucky to be part of this ambitious research team.

I would like to extend my gratitude to Prof. Charanjit Singh Bhatia for his continued support. I would like to thank my thesis committee Prof. Thomas Liew and Prof. Teo Kie Leong for their valuable suggestions. I am grateful to my seniors Xuepeng, Sankha, Gopinadhan, Jan, Surya, Ajeesh, Young Jun, Jae Hyun, Jae Sung, Mustafa and Mahdi for teaching me the art of scientific research and collaborating with me in my research endeavors. I also cherish the moments with my colleagues Praveen, Siddharth, Niu Jing, Shreya, Karan, Wu Yang and Li Ming for the fun and adventures in the lab, late dinners and fruitful discussions. Naganivetha, Junjia, Xinming, Shimon, Anil, Arkajit, Sandeep, Mridul, Sajid, Reuben, Shawn, Ramanathan Ghandi, Panneerselvam and Jungbum are few of the wonderful friends I made during the PhD journey. I would like to extend my special thanks to our lab managers Robert and Ms. Fong Leong. Over and above, I would like to thank each and every SEL and ISML members for their unconditional support through the years.

Most importantly, I would like to extend my thanks to my family members, especially my parents for their love, support and blessings. Also, thanks to my lovely wife Sulekha for her love and patience over these years.

TABLE OF CONTENTS

SUMMARY

Domain wall based devices have been intensively studied recently for the next generation 3-dimensional memories and logic systems. In this thesis, we have studied in-plane and out-of-plane anisotropy systems for domain wall device applications. For the in-plane anisotropy, NiFe has been investigated. It has a large anisotropic magnetoresistance as well as a very low magnetostriction coefficient. Co/Pd multilayers and CoFeB based tri-layer systems such as Pt/CoFeB/MgO and Ta/CoFeB/MgO are utilized for the perpendicular anisotropy. Tri-layer systems are a popular choice for future spintronics applications including domain wall devices due to the ability to tailor the magnetic properties such as perpendicular anisotropy, magnetostriction, critical current density as well as the newly discovered current induced spin orbit torques. Important aspects in the domain wall based devices such as domain wall generation, propagation, and detection are studied.

The design of pinning sites is crucial for the control of domain walls in nanowires. The most common approach to pin a domain wall is by introducing a constriction along the lateral edge of the nanowire. The parameters such as pinning fields and pinning potentials highly depend on the notch dimensions. The reproducibility and control of lateral dimensions are quite challenging in lithography. An alternative approach to pin a domain wall is investigated in this work. The pinning sites are created by etching out a selected portion of the magnetic nanowire, thus forming a vertical nanotrench across the whole width of the nanowire in contrast to the conventional approaches with a lateral trench across the small portion of the nanowire. The micromagnetic simulations show that the pinning strength can be effectively controlled by a proper selection of nanotrench dimensions. Different shapes of the potential profile are observed for transverse and vortex type domain walls. The symmetric nature of the nanotrench pining site offers less complicated domain wall evolution at the pinning site compared to the conventional the lateral V-notches. In permalloy nanowires with nanotrench pinning sites, both vortex and transverse types of domain walls have been experimentally shown to exist. Reliable pinning and depinning behaviors from a vertical nanotrench are observed. Compared to the

lateral constrictions, our proposed method has a higher precision in defining the dimensions of the pinning sites in the sub-nanoscale.

An alternative method to generate domain walls at predefined positions along the nanowire with the assistance of Joule heating is investigated in perpendicular anisotropy trilayers. The nanowire coercivity (H_C) is reduced by the Joule heating. When the assist field overcomes H_C, the part of the nanowire that experiences Joule heating undergoes magnetization reversal. The required current densities to generate domain walls are effectively controlled by the proper selection of the pulse width and the constant assist field, which is applied during the current pulse. The statistical analysis shows that this method allows to selectively generate a domain wall at a predefined location in perpendicular magnetic anisotropy nanowires with great reproducibility. This is challenging with other DW generation procedures based on random nucleation sites. The pulse width dependent analysis using modified Sharrock's equation confirms the Joule heating process. The proposed method can be extended to generate any desired number of domain walls in a single nanowire with relative ease compared to the Oersted field generation method.

Magnetic domain wall induced capacitance variation is investigated as a tool for the detection of magnetic reversal in magnetic nanowires for in-plane (NiFe) and out-of-plane (Co/Pd) magnetization configurations. The switching fields in the capacitance measurements match with that of the magnetoresistance measurements in the opposite sense. The capacitive behavior of the nanowire system is analyzed based on the modified Maxwell-Wagner capacitance model. The origin of the magnetocapacitance has been attributed to magnetoresistance. This magnetocapacitance detection technique can be useful for magnetic domain wall studies.

List of Tables

List of Figures

Chapter 1 : Introduction

1.1 Introduction to storage and logic devices

The ability to manipulate the electron's spin has paved the way for the next emerging branch in electronics – spintronics. Information is stored in the form of spin orientation in storage devices such as hard disks. Recent developments in nano-lithography have enabled applications of spin based devices in nano-scale. Advances in generating, manipulating and detecting spin-polarized electrons and electrical currents make possible new classes of spin based sensor, memory, and logic devices. The discovery of giant magneto-resistive (GMR) spin valve sensors has had an enormous impact on hard disk sensors [1-3]. The areal density of the hard disk shot up to 10 times in a short span of time [4]. The development of magnetic tunnel junction (MTJ) has further driven the areal density. A MTJ is a sandwich of thin layers of metallic ferromagnetic electrodes separated by a tunneling barrier (typically an oxide material) of a few atoms thick. Furthermore, a new class of memory based on MTJs is also under development which promises a high performance memory with a high density, speed, and non-volatility [5, 6]. However, the current developments in industrial products are approaching lithography limits. One of the possibilities to overcome this lithography limitation is to store information in 3-dimensional structures as in the proposed race-track memory system, where information is stored in the form of domain walls (DWs) [7]. The DW based memory system is widely heralded as a future storage system due to its inherent superior qualities such as a higher storage density, projected reliability, and lifetime of the devices. These DW based devices have a wider range of applications which can be extended to nano-oscillators and logic devices [8-10].

One of the challenges to realize DW based devices is the higher critical current density to move the DW in the direction of the electron flow. NiFe has been studied extensively as the basic material due to its ease of detection via anisotropic magnetoresistance (AMR) and negligible magnetostriction. However, NiFe suffers from issues such as the high critical current density, large domain wall size, etc. The solution lies in engineering the materials stacks as well as looking into new detection techniques other than AMR, which would pave a way for implementation of new material systems.

Perpendicular material structures have been proposed due to its superior properties over in-plane anisotropy materials. There have been considerable research in Co/Ni and Co/Pt perpendicular structures for DW studies, where the film is ultra-thin [11]. While this ultra-thin material stacks could be challenging to implement due to the sensitive dependence on the layer structures, it also offers the possibility of improving the heat dissipation by choosing appropriate layers. The recent discoveries of the Rashba [12] and spin Hall effect [13, 14] in metallic systems have shown another degree of freedom to engineer such material structures where an effective magnetic field appears to oppose or support the direction of the spin transfer torque. These effects also provide means to reduce the critical current density coupled with the existence of Dzyaloshinskii-Moriya interaction (DMI).

Another challenge is the design of pinning sites for DWs in nanowires. The DW behavior at the pinning site strongly depends on its geometry. Pinning sites in the shape of triangles and rectangles forming lateral constrictions along the nanowire are widely studied [15]. These pinning sites increase the potential barrier to overcome for motion of DWs. Even though the pinning potential can be modeled with software assistance, the real phenomena where the current density significantly changes around the notch will be difficult to model due to the spurious effects of the Joule heating. Moreover, the pinning notches could be implemented in vertical dimensions. However, a systematic study in three dimensional systems such as a vertical notch in nanowires has been not reported yet.

In order to realize DW based devices, improving DW generation, control, and detection are a few important aspects which should be taken into

consideration. In this thesis, we study and implement new strategies to address these challenges.

1.2 Magnetic nanowire based storage and logic devices

IBM scientists have envisioned a new memory system where bits of information are stored as magnetic domains in nano-sized magnetic wires known as "racetrack memory". This is an example of three-dimensional microelectronics devices. This new class of memory promises features such as high performance, low cost, and non-volatility [7].

Short pulses of spin polarized currents are used to move DWs between pinning sites. This memory scheme offers high performance, endurance of a conventional solid-state memory device, and lower cost than flash drives.

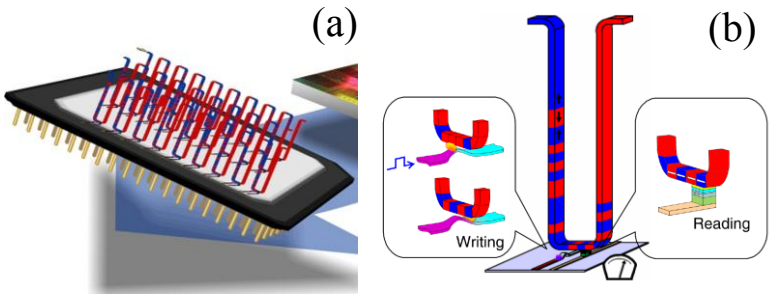

Figure 1-1: (a) Example of an innately three-dimensional microelectronics device. (b) Schematics and working principle of a vertical racetrack [7].

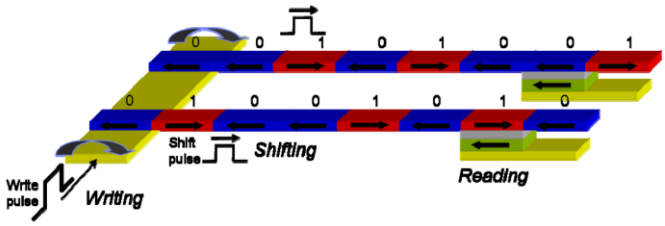

Figure 1-2: Schematics of a DW based storage device – lateral racetrack memory (RM) [16].

Arrays of nanowires can be used to form the racetrack device where these nanowires can be placed horizontally or vertically as in Fig. 1-1 or 1-2. A single data bit can be stored in DWs between two successive magnetic regions, which can be differentiated by the direction of local magnetization, or by the presence and absence of DWs between these two regions.

Mechanisms can be worked out to implement this device with writing and reading schemes. A writing device can be used to inject DWs into the nanowire, while a magnetic tunnel junction (MTJ) can be used as a read sensor. Each racetrack (nanowire) requires only one pair of a read sensor and a writing device. The magnetic bits/patterns can be moved around the nanowire by applying nanosecond long pulses. Many DWs (as many as 10 – 100) can be stored in a single racetrack. As a result, the stored number of data bits per unit area can be increased dramatically compared to the conventional 2D random access memories (RAM based technologies). It is expected that the vertical racetrack memory could accommodate the storage density comparable to that of a magnetic disk drive. Also, for the horizontal race track, the cell size can be much smaller than the typical MRAM cell. It has been estimated that with a proper selection of the materials, a data rate of 500 Mb/s can be reached in the horizontal racetrack memory with power smaller than 1mW per racetrack during the writing/shifting processes. There are a few demonstrations on prototype of racetrack memories [16, 17].

Magnetic DW based logic devices are also proposed. Simple logical operations such as NOT, AND, and signal cross-over elements are demonstrated in permalloy by magnetic field rotation [8]. There are proposals for extension of racetrack memories for logic applications [18]. A current controlled magnetic DW nanowire shift register was experimentally verified by Hayashi *et al.* A three-bit unidirectional magnetic DW shift register was also demonstrated [9].

Recent developments in perpendicular magnetic anisotropy (PMA) materials have significantly contributed to the improvements in DW based devices and it has taken a step closer in realizing these proposals. Recent developments in DW based systems are discussed in section 1.7.

1.3 Theory of ferromagnetic domains

1.3.1 The concept of magnetic domains

Ferromagnetic domain concept was developed by Weiss who suggested the existence of magnetic domains in a ferromagnet. Based on the

small regions (ferromagnetic domains), Weiss was able to explain the existence of demagnetized state. A domain configuration is a resultant consequence of the various contributions to the total energy of the ferromagnetic body. The total energy of the ferromagnetic body consists of the energy terms such as exchange energy, magnetocrystalline anisotropic energy, magnetoelastic energy, and magnetostatic energy. Large magnetostatic energy which is associated with the stray field can be decreased by forming a domain structure. The domain structure can remove the uncompensated poles on the surface of the specimen.

The magnetostatic energy associated with a stray field is given by, $E_s = \frac{\mu_0}{2}\int H_s^2 dV$, where H_s is the stray field and dV is the volume of space. The magnetostatic energy is due to the interaction between magnetic dipoles. The magnetic dipole-dipole interaction is very small compared to the strong exchange interaction which is a very short range interaction. However, the magnetic dipole-dipole interaction is long range and so this interaction is important for magnetic moments that are separated by large distances. The uncompensated free poles lead to the formation of a domain structure to reduce the magnetostatic energy.

The structures shown in Fig. 1-3 clearly explain the formation of domains. Figure 1-3(a) shows a single domain area which has higher stray field, thus higher magnetostatic energy. In Fig. 1-3(b) the stray field is reduced by approximately half. Similarly, in Fig. 1-3(c), the stray field is reduced to a quarter of the value of (a), and in (d) the stray field is almost completely removed.

However, forming domain structures take place at the expense of increase in other energy components such as exchange energy. Eventually, further subdivision into domains will continue only until the expense of energy terms are equated by the reduction in magnetostatic energy, and subsequently an equilibrium domain size will be attained. The energy terms in this competition are discussed in the next section.

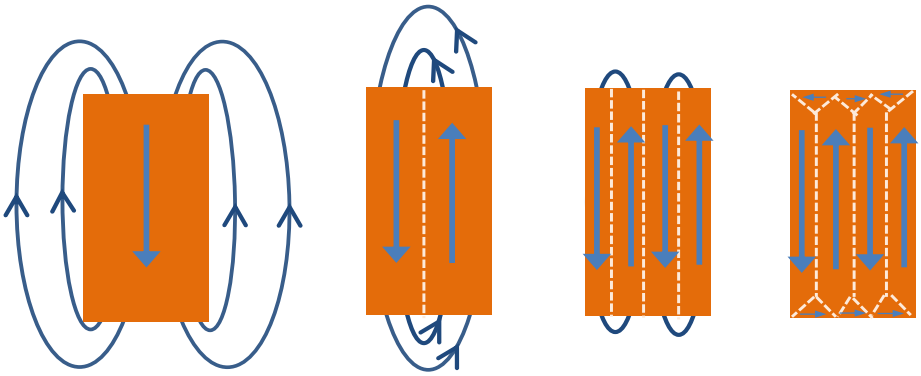

Figure 1-3: (a) A saturated structure with higher magnetostatic energy contribution. The magnetostatic energy is reduced by forming domain structures from (b) to (d). There considerable reduction in stray field in (d) is due to the lack of free poles on the sample surface.

1.4 The energetic contributions to a ferromagnet

1.4.1 The total free energy of a ferromagnet

The total free energy (E_{total}) of a ferromagnetic system in thermodynamic equilibrium is given by

$$E_{total} = \int_V \phi_{total} dV = 0 \tag{1.1}$$

where ϕ_{total} is the total free energy density of the system and V is the sample volume. The total free energy density comprises of 5 energy terms which is given by

$$\phi_{total} = \phi_A + \phi_K + \phi_\sigma + \phi_S + \phi_{Zeeman} \tag{1.2}$$

The components are exchange (ϕ_A), magnetocrystalline anisotropy (ϕ_K), magnetoelastic (ϕ_σ), magnetostatic (ϕ_S), and Zeeman (ϕ_{Zeeman}) energy densities [19].

1.4.2 Exchange energy

A quantitative expression for exchange energy is obtained by the following analysis. Assume two atoms with i and j have spin angular momentum S_i and S_j. The exchange energy is given by the Vleck formula [20]

$$E_{ex} = -2J_{ex}\sum S_i \cdot S_j = -2J_{ex}S^2\sum \cos\phi_{i,j} \tag{1.3}$$

where J_{ex} is the exchange integral and ϕ is the angle between adjacent spins. In the case of ferromagnetic materials, exchange integral is positive. Therefore, the exchange energy is negative when adjacent spins are parallel, and positive when the spins are anti-parallel. Exchange stiffness parameter, A is defined as

$$A = \frac{J_{ex}S^2}{a} \tag{1.4}$$

where a is the lattice parameter. The exchange stiffness parameter gives a measure of the energy, when nearest neighbor spins are not completely parallel. For permalloy, the exchange stiff constant is 1.3×10^{13} J/m [21].

1.4.3 Magneto crystalline anisotropy energy

The magnetocrystalline anisotropy energy prefers the magnetization to be directed along certain definite crystallographic axes, which are also the directions of "easy" axes of magnetization. On the other hand, the directions which are difficult to align the magnetization in a crystal are called "hard" axes. The cost of energy to align the magnetization in the hard axis rather than the easy axis is known as the magnetocrystalline anisotropy energy.

For uniaxial crystals the magnetocrystalline anisotropy energy density is given by

$$\phi_K = K_1 \sin^2\theta + K_2 \sin^4\theta \tag{1.5}$$

where θ is the angle between the easy axis and the magnetization. Here, higher order terms are neglected.

Magnetocrystalline energy is dominant in single crystal specimens. For polycrystalline samples with random orientation of crystalline grains, this energy averages out. Therefore, such samples exhibit no net magnetocrystalline anisotropy, although there will be local distribution of magnetization influenced by the local magnetocrystalline energy. However, most of the polycrystalline samples have a preferred orientation or texture which can be enhanced by the preparation technique. For permalloy, K_1 is very

small and slightly negative, which indicates that easy axes of magnetization corresponds to the [111] set of directions.

1.4.3.1 Surface anisotropy

The local environment of atoms differs at both surfaces of a thin film with respect to the bulk one. Néel suggested that this breaking of symmetry induced another magnetic anisotropy which is later known as surface magnetic anisotropy or interface anisotropy. This effect becomes negligible if the thickness is more than a few nanometers. In magnetic ultrathin films, the anisotropy density is given by

$$\phi_{KA} = K_{eff} \sin^2 \theta \tag{1.6}$$

where θ is the angle between the normal to the plane and the magnetization. K_{eff} is given by

$$K_{eff} = K_V + \frac{2K_S}{t} \tag{1.7}$$

where K_V is the effective volume anisotropy constant (containing magnetocrystalline terms) and K_S is the effective surface or interface anisotropy. The relationship is derived for the magnetic layer bounded by two identical interfaces accounting for the prefactor 2. When K_S favors the alignment of magnetization along the normal to a thin film ($K_S < 0$), it induces perpendicular magnetic anisotropy. In such systems (Co/Pd, Co/Pt, Co/Au multilayers), the typical thickness of the magnetic layer is less than 2 nm.

1.4.4 Magnetoelastic energy

The magnetoelastic energy arises from the interaction between the magnetization and the mechanical strain of the crystal lattice. An applied field re-orientates the spin moments and changes the magnetization direction. In response to that, due to the spin-orbit interaction, the electron orbitals also try to re-orientate. For 3*d* ferromagnetic elements, this effect is less. However, in the rare-earth metals where the spin-orbit coupling is strong, this results in a large reorientation of the electron orbits, when the magnetization direction is changed. Magnetostrictive coefficient is (λ) the fractional change in length as

the magnetization increases from zero to its saturation value. Therefore, magnetostrictive effects in the rare-earth metals can cause considerable distortion.

In general, the magnetoelastic energy density is given by

$$\phi_\sigma = \frac{3}{2}\left(\lambda_s \sigma \sin^2\theta\right) \tag{1.8}$$

where σ is the magnetoelastic tensor, θ is the angle between the saturation magnetization and magnetoelastic tensor, and λ_s is the average value of saturation magnetostriction. For permalloy films above 7 nm thickness, it is observed that the magnetostriction vanishes [22].

1.4.5 Magnetostatic energy

Magnetostatic energy is associated with stray field originating from the sample due to the dipole – dipole interaction (as discussed in section 1.3.1). Therefore, this energy is associated with the magnetic field generated by the magnetic sample itself. The stray field tends to oppose the saturation magnetization.

The magnetostatic energy density is given by

$$\phi_s = \frac{\mu_0}{2} H_s \cdot M_s \tag{1.9}$$

where H_s is the stray field and M_s is the saturation magnetization.

1.4.6 Zeeman energy

Zeeman energy is the energy associated with the interaction between the externally applied magnetic field and the saturation magnetization. When the system aligns parallel (anti-parallel) to the external magnetic field, the energy minimizes (maximizes). The Zeeman energy density can be written as

$$\phi_{Zeeman} = -\mu_0 H_{ext} \cdot M_s \tag{1.10}$$

where H_{ext} is the externally applied magnetic field.

1.5 Magnetization dynamics

Similar to a current carrying wire loop, an electron spinning about its axis has a magnetic moment. This magnetic moment, μ, is related to the angular momentum associated with electron spin, L, by the gyromagnetic ratio, γ [23].

$$\mu = \gamma L \tag{1.11}$$

The equation of motion for the magnetic moment of an electron is given by [24]

$$\frac{dM}{dt} = -\gamma\left(M \times H_{eff}\right) \tag{1.12}$$

where $M = \sum \mu$, H_{eff} is the magnetic field. In this equation, there is no dissipation term; therefore the magnetization will continue to precess forever as shown in the schematics in Fig. 1-4.

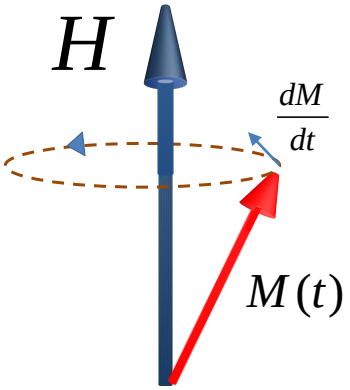

Figure 1-4: Magnetization precession.

1.5.1 Damping

In real systems, energy is dissipated through various sources, and the magnetization motion is *damped* until an equilibrium position is reached. The energy could be dissipated through the excitation of spin waves, by formation of eddy currents, or by direct coupling to other fields such as stray fields. All the energy is finally converted into phonons (microscopic thermal motion in the lattice system), magnon (magnetic system), or thermal excitation of conduction electrons. With the addition of the damping term in the equation, the magnetization precession vector shown in Fig. 1-4 will gradually lose its

energy and spiral down to the direction of the applied field to reach its equilibrium under certain conditions. Landau-Lifshitz (LL) equation is given by

$$\frac{dM}{dt} = -\gamma[M \times H_{eff}] + \frac{\alpha\gamma}{M_s}[M \times (M \times H_{eff})] \tag{1.13}$$

Gilbert improved the equation and the modified equation is known as Landau-Lifshitz-Gilbert (LLG) equation and is given by

$$(1+\alpha^2)\frac{dM}{dt} = -\gamma[M \times H_{eff}] + \frac{\alpha\gamma}{M_s}[M \times (M \times H_{eff})] \tag{1.14}$$

LLG equation contains additional term $(1+\alpha^2)$ which becomes negligible when α becomes very small. The LLG equation is typically written in the shorten form as below.

$$\frac{dM}{dt} = -\gamma[M \times H_{eff}] + \frac{\alpha}{M_s}\left[M \times \frac{dM}{dt}\right] \tag{1.15}$$

1.6 1D domain wall model

A Bloch profile obtained in the one-dimensional (1D) limit, namely the Bloch-wall profile is investigated for DWs in thin films by Nakatani *et al.* [25].

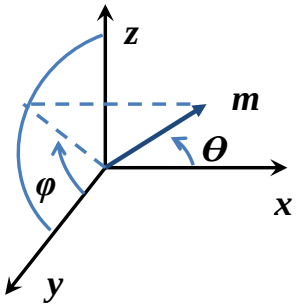

Figure 1-5: The definition of co-ordinate system used to describe in the 1D model of DW profile.

A typical DW is described by the following schematics as shown Fig. 1-6. The coordinate system used to describe the 1D model is shown in Fig. 1-5. The two outer regions, I and III, are homogeneous. Only in the middle region (II) the magnetization profile changes from -1 to +1. This is the region where the DW exists.

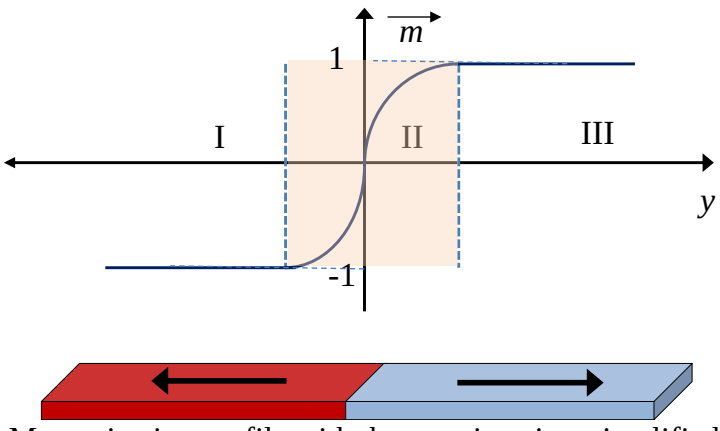

Figure 1-6: Magnetization profile with three regions in a simplified model.

The traditional tail to tail 1D Bloch wall is given by [25]

$$\begin{aligned} m_x &= \tanh(x/\Delta) \\ m_y &= 1/\cosh(x/\Delta) \end{aligned} \tag{1.16}$$

where m_x and m_y are the components of the unit magnetization vector in the longitudinal and transverse direction. Δ is defined as the DW width parameter.

The 1D model of a nanowire incorporates two effective anisotropy terms originating from magnetocrystalline and magnetostatic energy. The other term exchange energy arises from the non-uniformity of the magnetization in the cross section.

The general anisotropy energy density is given by

$$E_{an,eff} = K_0 sin^2\theta + \sum_{n=1}^{\infty} K_n sin^{2n}\theta K_0 sin^2(2\,\mathrm{n}\,\varphi + \varphi_n) \tag{1.17}$$

where the sum is limited to n = 1 with $\varphi_1 = 0$ and the exchange energy for magnetization along the *x* only is given by

$$E_{ex} = A\left(\frac{dm}{dx}\right)^2 = A\left[\left(\frac{d\theta}{dx}\right)^2 + \sin^2\theta\left(\frac{d\varphi}{dx}\right)^2\right] \tag{1.18}$$

There is no driving force for a variation of φ with *x*. Therefore, the anisotropy term is limited to one in the summation of E_{an}. φ is constant and $\varphi(x) = \phi$. For the DW profile, $m_x = \cos\theta, m_y = \sin\theta$, the optimal DW-width parameter depends on ϕ and it can be written as

$$\Delta = \sqrt{\frac{A}{K_0 + K\sin^2\phi}} \tag{1.19}$$

From the Bloch wall type solution, The total exchange energy is $2A/\Delta$, the total anisotropy energy is $2\Delta(K_0 + K\sin^2\phi)$, and the total energy is given by $4\sqrt{\mathrm{A}(K_0 + K\sin^2\phi)}$, where the integral of $m_y = \pi\Delta$ [25].

1.6.1 Wall types in nano-strips

In the above discussion, the nanowire width is in the order of exchange length. However, in a typical nanowire, the width is much larger than the exchange length (Λ).

1.6.1.1 Transverse wall

The wall magnetization in a transverse wall is oriented along the y-axis due to the magnetostatic interactions. The strip geometry allows wall distortion along the *y*-axis. The reduction of the magnetostatic integration in this case is mainly due to the small strip thickness. The fit with the 1D model

and the micromagnetic simulations for a transverse wall is shown in Fig. 1-7(b).

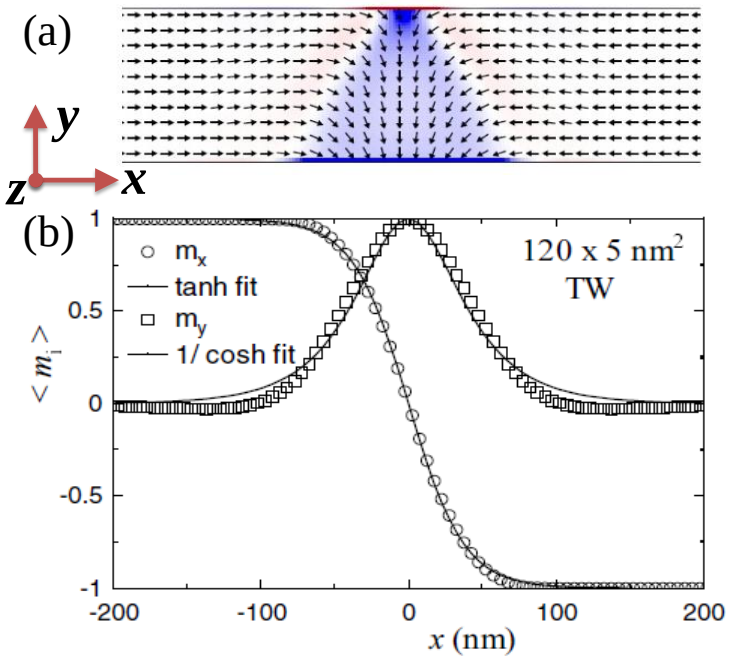

Figure 1-7: Transverse wall in a nanostrip (width – 120 nm; thickness – 5 nm; cubic mesh 5 × 5 × 5 nm^3). (a) Arrows show the magnetization direction. (b) Comparison of the micromagnetic simulation with the 1D model [25, 26].

1.6.1.2 Vortex wall

In the nanowire case, increased strip cross section allows for a flux closure structure to develop and form a vortex wall. The moments at the vortex core point upwards or downwards. The fit with the 1D model and the micromagnetic simulations for a vortex wall is shown in Fig. 1-8(b). The larger differences in the fitting shows that the transverse wall fits better for the case of 1D DW model.

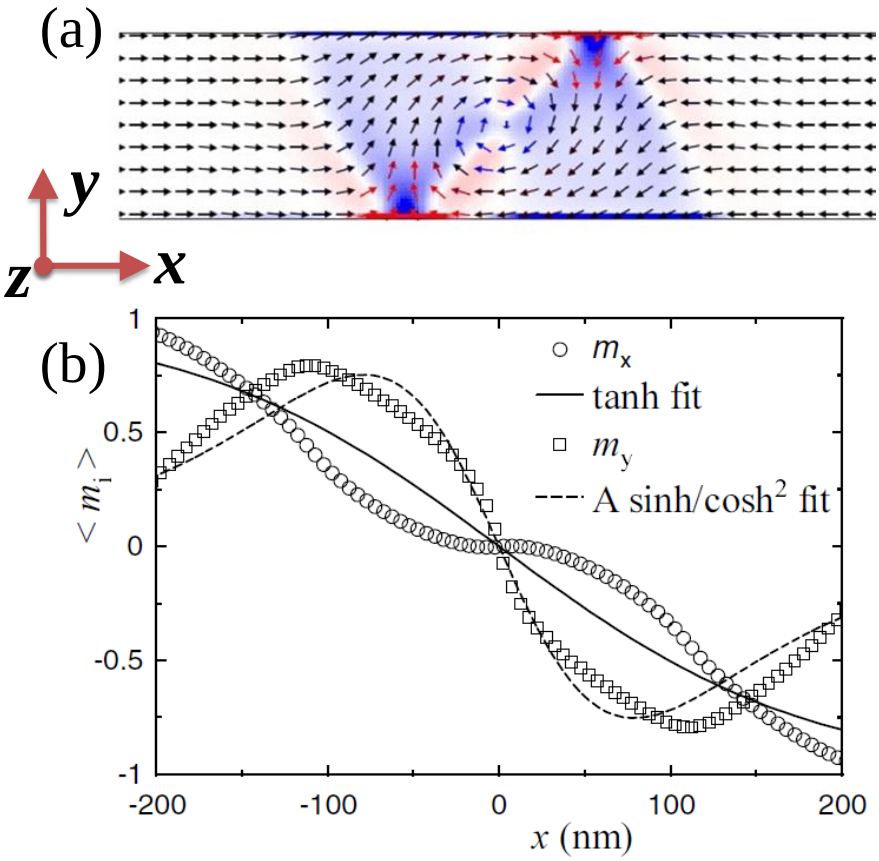

Figure 1-8: Vortex wall in a nanostrip (width – 240 nm; thickness – 10 nm; cubic mesh 5 × 5 × 5 nm^3). (a) Arrows show the averaged magnetization in axial m_x and transverse m_y direction. (b) Comparison of the micromagnetic simulation with the 1D based model [25, 26].

1.6.1.3 Phase diagram

The phase diagram of a DW structure in a nanostrip is investigated by McMichael and Donahue [27] with transverse walls and vortex walls as shown in Fig. 1-9(a)-(b). The DW width increases with strip width, however it is only weakly dependent on the strip thickness for transverse and vortex walls. The DW widths for transverse and vortex walls are $\Delta = w/\pi$ and $\Delta = 3w/4$, respectively. In the asymmetric transverse wall case as shown in Fig. 1-9(c), Δ increases with increasing the strip width and thickness.

Four types of distinguishable DWs are experimentally found to exist in permalloy nanowires. Depending on the chirality of the spin orientation, the DWs can be classified into clockwise and anti-clockwise. The four states of DWs are shown in Fig. 1-11 from the same nanowire from different measurements [28].

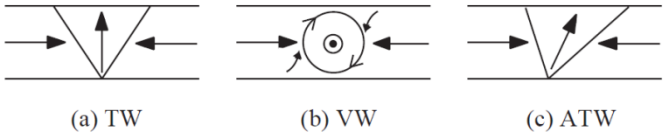

Figure 1-9: Domain wall structures in nano-strips with magnetization along the longitudinal direction. (a) Symmetric transverse wall. (b) Vortex wall. (c) Asymmetric transverse wall [25].

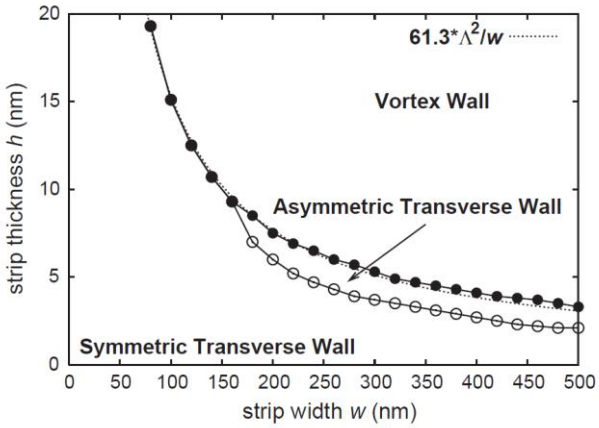

Figure 1-10: Phase diagram of the domain wall structure in permalloy nano-strips [27].

Figure 1-11(a) and (b) shows the clockwise configuration of the transverse and vortex wall, respectively, while Fig. 1-11(c) and (d) show the anti-clockwise configuration of the transverse and vortex wall, respectively. The corresponding simulated MFM divergence and the magnetization direction are also shown below the MFM images. More complex DW structures can also be formed. One such example is cross-tie domain wall (XDW). A XDW consists of a main DW, separating two antiparallel magnetic domains. The structure of the main wall varies continuously along its length, comprising alternating Néel and Bloch sections. XDWs are found in films with low anisotropy in an intermediate thickness range. Below the lower bound, Néel walls exist and above the upper bound, the asymmetric Bloch wall is found [29].

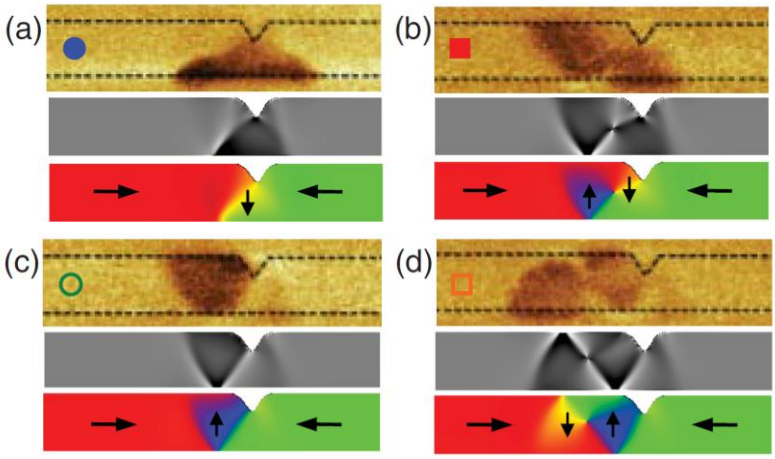

Figure 1-11: Four different types of DWs in permalloy nanowire. (a) and (b) show clockwise transverse and vortex walls while (c) and (d) show anti-clockwise transverse and vortex walls, respectively. The corresponding simulated divergence and the magnetization profile are also shown [28].

1.7 Recent development in domain wall based devices

Domain walls in in-plane magnetic anisotropy materials have been extensively studied experimentally and theoretically in the recent decade. Theoretical models have been developed to elaborate the current induced spin transfer torque mechanism in such systems [30, 31]. However, the choices of in-plane magnetic anisotropy materials are limited for DW applications. Permalloy (NiFe with different combinations) has been a favorite choice in-plane magnetic anisotropy system due to reasons such as ease of detection using AMR, and very low magnetostriction. The other systems include CoFe [32] and multilayer structures forming spin valves with Co and NiFe [33-35].

Even though the permalloy has been well studied as the candidate of DW based racetrack devices, it poses a few challenges. For permalloy, current driven DW motion is predominantly observed, when the DW takes up a vortex structure [16]. Vortex structures are energetically stable. However, vortex structures are formed when the nanowire is ~ 100 nm wide thus requiring bigger structures. The dimensions of the vortex walls are quite large extending to few hundred nanometers [36]. The close packing of DWs needed for a high density racetrack memory gives rise to strong dipolar interactions between the DWs. The spin torque effect in permalloy cannot overcome small parasitic magnetic fields or pinning from tiny defects [7]. This strong pinning of DWs

requires much higher current densities to move the DWs. However, the maximum current density is limited by Joule heating and the consequent rise in temperature in nanowires. For nanowires thinner than 40 nm, the reported critical current densities are between 5×10^7 and 30×10^7 A/cm^2 [37]. Klaui *et al.* have reported 5×10^7 A/cm^2 for a 5 nm thick nanowire and 1.3×10^8 A/cm^2 for a 35 nm thick permalloy nanowire [38]. The summary of the critical current density reported by different experiments in permalloy is shown in Fig. 1-12.

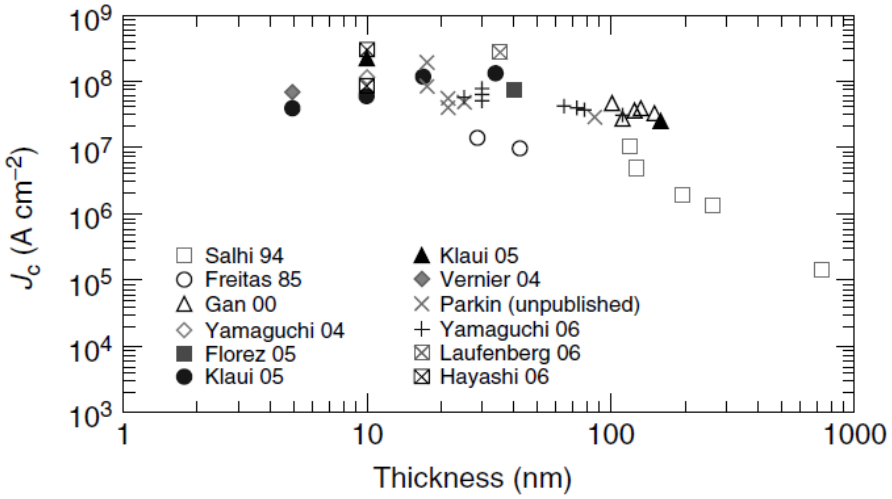

Figure 1-12: Critical current density for DW motion in permalloy nanowires. For nanowires thinner than 40 nm, the reported critical current densities are 5 - 30×10^7 A/cm^2 [37].

These limitations can be overcome by using magnetic materials with large perpendicular anisotropy. DWs in PMA systems can be very narrow (as little as ~ 1-5 nm) and their width is independent of the nanowire width. In contrast to permalloy, current-driven motion in PMA materials is much less sensitive to both pinning from defects and any local magnetic fields [39]. The DWs are more strongly pinned in PMA materials than in permalloy because of their smaller width. Koyama *et al.* have reported motion of DWs in PMA Co/Ni multilayered race tracks for current densities ~ 2.0×10^7 A/cm^2 which is 5 times smaller than that in permalloy, even though it has a strong pinning fields of ~ 200 Oe [11]. Moreover, PMA system provides easier ways to detect the local magnetization. The Hall resistance provides a local probe of the magnetization direction, similar to the response of a MTJ sensor. Also, the

separation between two DWs can be controlled below ~ 750 nm compared to the permalloy system which requires 6 times larger separation [16].

Apart from the magnetic field, the magnetization can also be controlled by electric field which opens avenues for real applications [40]. Electrical modulation of the energy barrier for the magnetic domain wall motion is recently demonstrated by various groups. Schellekens *et al.* demonstrated electric field controlled domain wall motion in Pt/Co/AlOx systems in microwires. This low power consuming methodology to control the magnetization can be readily integrated in existing technology [41]. Chiba *et al.* have demonstrated the control of DW velocity by the electric field in Co/Pt micro wires with HfO_2 as the insulating layer. The creep regime velocity of the DW is modulated from 10^{-6} – 10^{-3} m/s with the application of electric fields in the range of ±2–3 MV/cm [42]. Bauer *et al.* demonstrated electric field modulation in Co/GdO_x [43], in which strong voltage-controlled domain wall traps function as non-volatile, electrically programmable, and switchable pinning sites. Pinning strengths of at least 650 Oe can be readily achieved, enough to bring to a standstill domain walls travelling at speeds of at least ~ 20 m/s [44]. Furthermore, the electric field control of magnetization has been proposed for efficient DW based logic devices.

The recent developments on current induced torques, such as the Rashba and spin Hall effect, have provided further means to manipulate the domain wall dynamics [45-47]. Miron *et al*. demonstrated current induced DW motion in $Pt/Co/AlO_X$ ultra-thin nanowires at the velocity as high as 400 m/s compared to the maximum of 100 m/s reported in permalloy nanowires [12].

Current induced DWs are reported to move in opposite directions in Pt/CoFe/MgO and Ta/CoFe/MgO nanowires. Liu *et al.* have demonstrated that the combination of the spin Hall effect in the normal metal and the spin transfer into the ferromagnet can switch the magnetization direction [48]. Further development in this area has elucidated the chiral dependency of DWs in ultra-thin perpendicular thin films. Néel and Bloch walls exist in ultra-thin films. The magnetization is always perpendicular to the current direction in Bloch walls. On the other hand, the relative orientation of the magnetization and current gradually varies in Néel walls. The magnetostatic interaction

favors the formation of Bloch walls. In case of Néel walls, there is no preference of chirality due to the spatial inversion symmetry. However, Luc *et al*. [49] and Beach *et al.* [50] proposed that there exists a mechanism called Dzyaloshinskii–Moriya interaction (DMI) that breaks the spatial inversion symmetry introducing chirality in the systems they studied. DMI favors the formation of Néel walls over Bloch walls. Together with the spin Hall effect and Slonczewski spin torque, the DMI pushes all of the chiral walls rapidly in the same direction [51]. This provides a revolutionary approach to control domain walls in perpendicular systems.

1.8 Micromagnetic simulations

Micromagnetics plays an important role in nano-magnetism, an emerging area in spintronics. Micromagnetics acts as a translator between the proposed theories and equations into quantitative predictions. In this thesis, the micromagnetic simulations are performed by object oriented micromagnetic framework (OOMMF) developed by National Institute of Standards and Technology (NIST) and distributed freely on internet [52].

The two different methods used in micromagnetic modeling are finite difference method (FD) and finite element method (FEM). OOMMF solver is developed based on FD which is suited for definite geometrical shapes. The defined object is meshed on fixed rectangular cubic elements (e.g. 15×10×5 nm^3). It is solved for fully 3D objects.

1.8.1 Cell size and exchange length

To improve the accuracy of the simulations, small cell sizes are chosen. However, the dimensions are sufficient to provide accurate results, when the cell size is in the comparable length of the exchange length. The exchange length is given by the following equation

$$\Lambda_{ex} = \sqrt{\frac{2A}{\mu_0 M_s^2}} \tag{1.20}$$

where A is the ferromagnetic material's exchange stiffness and M_S is the saturation magnetization. For permalloy, with Λ_{ex} is ~ 5 nm.

In perpendicular anisotropy systems, the domain wall width is quite small [53]. In that scenario, the cell size should be similar to the domain wall width, δ_w [54]

$$\delta_w = \sqrt{\frac{A}{K}} \tag{1.21}$$

With parameters corresponding to CoPtCr (A = 10^{-11} J/m, M_S = 3×10^5 A/m, K = 2×10^5 J/m^3), δ_w yields 7 nm and Λ_{ex} is ~ 13 nm [55].

1.8.2 Simulation geometry

For our studies in this thesis, magnetic DWs are studied in magnetic nanostrips. When the nanowires are long, it is impossible to mesh the whole magnetic system entirely for solving. However, the magnetization is invariant along the length of the nanowires far away from the DW and at the wired ends. Therefore, it is possible to use a restricted region for calculations as follows: An infinitely long nanowire is mimicked by cancelling the magneto-static charges at the ends as shown in Fig. 1-13. The left and the right portions are set with a fixed magnetization. The domain wall motion studies take place inside the middle region.

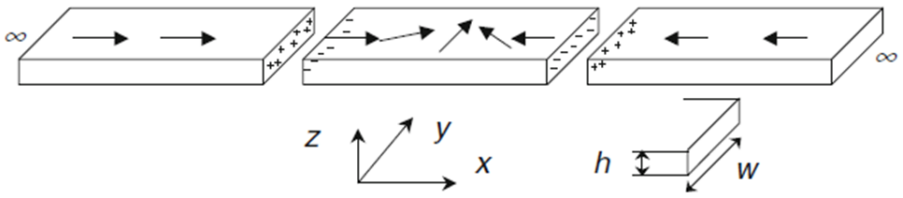

Figure 1-13: A long nanowire is divided into three parts. The left and the right parts have fixed magnetization values. The middle portion has the domain wall [25].

1.9 Objectives

There are several aspects that need to be addressed to make nanowire based magnetic devices technologically feasible. Few such aspects are domain wall generation, propagation, and detection. A few domain wall generation methods are employed in magnetic trilayer systems. However, the popular methods require either additional lithography steps or rely on random pinning sites to generate domain walls in perpendicular systems. Domain wall control sensitively depends on the potential landscape generated by the pinning sites. The conventional notches formed by lateral constriction make DW pinning a complicated phenomenon. Electrical detection techniques are quite simple and fast methods for domain wall detection in nanowires. However, the detection techniques such as anisotropic magnetoresistance or anomalous Hall effect are quite dependent on the material. Addressing these above questions are the main objectives of this work.

1.10 Organization of the thesis

Chapter 1 presents an introduction to storage and logic devices with the emphasis on nanowire based devices. This chapter introduces the background for domain walls in magnetic nanowires. The recent developments in magnetic domain walls are also reviewed. The experimental methods used for this work is elaborated in Chapter 2. The device making procedures as well as structural and magnetization characterization schemes are briefly discussed. Magnetic domain wall characterization in nanowires is presented in chapter 3. Magnetic force microscopy and electrical measurements are employed for domain wall detection in both NiFe and Co/Pd multilayers. Chapter 4 presents domain wall pinning studies at vertically etched nanotrench pinning sites. The experimental results are supported by micromagnetic simulations and compared with the conventional V-notches. Thermally assisted domain wall generation in perpendicular trilayer nanowires is described in Chapter 5. The current pulse amplitude required for domain wall generation is studied with respect to assist field and pulse width for three different trilayer stacks. Chapter 6 describes magnetocapacitance measurements in magnetic nanowires. It is established

that the magnetocapacitance measurements can be implemented as a DW detection technique in both NiFe and Co/Pd multilayers. A brief summary of this work concludes the thesis in Chapter 7.

Chapter 2 : Experimental techniques

This chapter presents an overview of the experimental techniques utilized in this research work. In the first section, thin film growth techniques are discussed. The requirements for growing magnetic thin films are briefly presented. In the following section, device fabrication methodologies are presented in details. The lift-off method and subtractive method are utilized to make nanoscale devices. Finally, the structural and magnetic characterization techniques are presented in brief.

2.1 Thin film deposition processes

2.1.1 Magnetron sputtering

For the work presented in this thesis, magnetron sputtering is utilized for both thin film growth and electrode depositions [56]. Sputtering is the one of the preferred vacuum deposition techniques utilized in research as well as in industry. Sputtered films exhibit excellent uniformity, density, purity, and adhesion especially in magnetic films.

Inert gas such as Ar or He are used in vacuum conditions for the sputtering process. A typical working principle of dc-magnetron technique is presented in the schematics in Fig. 2-1. Permanent magnets are placed under the sputtering material (target), which produce a strong magnetic field. When a strong voltage is applied, the inert gas gets ionized (e.g. $Ar \rightarrow Ar^{+} + e^{-}$) and generates plasma. These ions are continuously accelerated towards the negatively charged target surface. Argon ions bombard on the target surface and the target material is ejected from the surface. These particles traverse the chamber and are deposited as a thin film onto the surface of the substrate. This process is known as sputter deposition. Also, these impacting ions generate secondary electrons which feed the formation of further ions and sustain the

plasma in the chamber. Initially excess amount of Ar is injected into the chamber to generate plasma. However, when the required deposition takes place, the Ar flow is adjusted in order to control the properties of film growth.

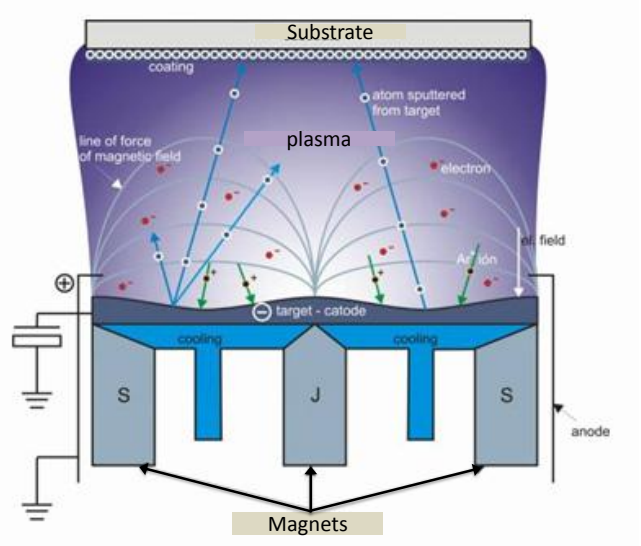

Figure 2-1: Dc-magnetron deposition process. The sputter target is placed on top of permanent magnets and the substrate is directly on top of the target. Line of force of magnetic field is also shown in the diagram [57].

The sputtering technique can also be used to deposit alloys of oxides and nitrides either with reactive sputtering methods or with RF guns. The charge accumulation of the ions on the oxide targets causes the plasma to die off. To avoid this issue, a radio frequency (RF) ac-voltage is applied at the target to prevent the buildup of charges at the top surface. However, the RF-power based deposition method provides a very slow deposition rate compared to that of dc-deposition [58].

Figure 2-2: A sputter deposition system used for magnetron sputtering. The power supplies and the deposition chamber are visible in the image [59].

Thin films are grown in a sputtering chamber with multi targets as shown in Fig. 2-2. The base pressure of the chamber is maintained at ~ 1×10^{-9} Torr. The plasma is controlled at very low pressures during the deposition by controlling the Ar flow, which allows depositing high quality thin films. Moreover, an in-situ magnetic field is applied for samples to induce an anisotropy for some DW based device experiments. The heating facility in the chamber is also utilized to deposit films at higher temperatures, or the films are post-annealed at vacuum conditions after the deposition.

2.2 Device fabrication

2.2.1 Sample preparation

For the research works discussed in this thesis, samples are prepared mainly in two types of substrates which are Si substrates with naturally grown oxide of a thickness of 200 – 300 nm and glass substrates. First, the substrates are diced into 1×1 cm^2 or 0.5×0.5 cm^2 pieces to be used for device fabrication purposes. These diced substrates undergo a substrate cleaning procedure discussed below before the device fabrication process.

At first, these substrates are heated in the Ozone stripper at 150° C for 20 minutes. This process ensures that the organic contaminants are removed from the substrates. Secondly, the substrates are ultrasonicated in acetone for 10 minutes. This step removes the inorganic contaminants. Subsequently, the substrates are ultrasonicated in isopropanol (IPA) for 10 minutes. This step ensures the complete removal of acetone from the sample surface. De-ionized water is used to wash away the IPA contaminants. Finally, dry Nitrogen is used to blow the sample surface.

2.2.2 Photolithography

Photolithography is a widely used for micro-fabrication of thin film devices. The patterns on the hard mask (known as photomask) are transferred onto the substrate covered with a resist (photoresist) with ultra-violet (UV) light. Typically, the photomasks are prepared on quartz substrates. The required patterns are made on the chromium layer on the substrate. UV light

passes through the quartz regions and blocked by the chromium regions. The photoresist is selectively sensitive to the frequency of the light. An illustrative diagram depicting the exposure procedure is shown in Fig. 2-3. The patterns are obtained by developing the exposed substrates. The exposed area gets washed away by the developer for positive tone photoresist. In case of the negative tone photoresist, the exposed area remains after development process. For the work presented in this thesis, a Karl Suss mask aligner (MA6) is utilized for device fabrication especially for electrode depositions as shown in Fig. 2-4.

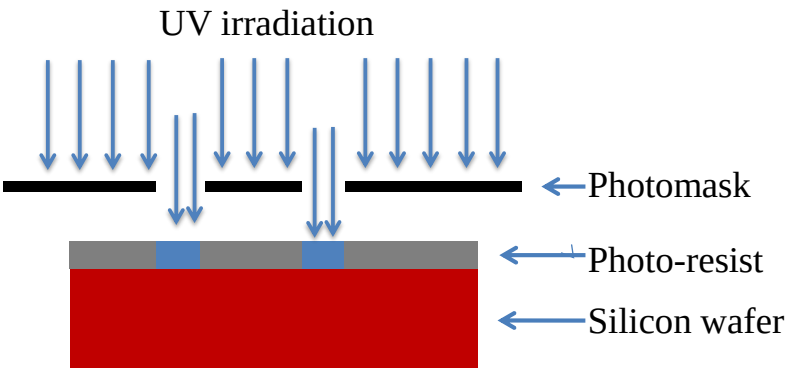

Figure 2-3: Photomask is used to selectively block the UV-irradiation. The resist gets exposed through the quartz region of the mask.

Figure 2-4: A MA6 Karl Suss mask aligner used for photolithography [60].

For electrode depositions, positive photoresists such as AZ 7200 (from Clariant GmbH) and PFI (from Sumitomo) were utilized. The positive exposed regions are developed using AZ-300 MIF developers which is a Tetramethylammonium hydroxide (TMAH) based aqueous solution [61].

2.2.3 Electron beam lithography

Electron beam lithography (EBL) is one of the key fabrication techniques used for creating patterns at the nanoscale. The working principle of EBL is quite similar to the photolithography [62]. A focused beam of electrons is used to scan over a substrate which is covered with EBL resist (electron sensitive resist). According to the exposed energy (dose) of the electron beam, the solubility of the resist can be controlled. When the electron energy is exposed on the positive tone EBL resist, the polymer in that exposed region begins to separate (through molecular scission) and is washed away by the developer. On the other hand, the exposed negative tone EBL resist gets hardened (molecules get cross-linked) and that area remains after the development process.

Figure 2-5: Raith e-line lithography system is used for lithography [63].

Both the positive and negative tone resists were used for device making as discussed in detail in section 2.2.5. The system used for the EBL is shown in Fig. 2-5. A magnetic shielding is employed to prevent the magnetic

field noise from the surrounding area. This careful step improves the beam control and ultimately the lithography precision.

2.2.4 Dry etching

Etching is a common technique used to create the desired pattern by removing the unprotected parts of a material. One of the methods of etching is by employing a wet/chemical process in which a substrate is submerged in an etching solution. This is an isotropic process. Another approach is dry ion etching such as ion beam milling process. Submicron ion particles are accelerated and bombarded onto the surface of the substrate with a resist/hard material to protect the desired pattern. The etching rate of the resist/hard material is typically lower than that of the etching material to be removed. In the case of Ar ion milling, the Ar ions (in the plasma) are formed by electrical discharge and it is accelerated by an optically aligned grid to form highly collimated beam. The sample is mounted on a rotating platform, the angle of which platform can also be controlled. This not only makes the etching process uniform throughout substrate surface, but also removes the waste material resulting in straight side walls. In addition to that, it also avoids the undercutting. Ion milling offers a higher precision and repeatability compared to other forms of etching [64].

We have used Ar based ion miller for our research purposes. This system is also equipped with secondary ion mass spectroscopy (SIMS) which is used to detect the elemental, isotopic or molecular composition of the sample surface. In addition to that, this system also incorporates in-situ magnetron sputtering capability. This option is utilized whenever the device fabrication process requires deposition right after the ion milling process, without breaking the vacuum. Ion milling is mainly used for transferring the desired patterns onto the thin film. This process is discussed later as subtractive method in section 2.2.5.2. Etching is also done before depositing the contact pads to clean the interface to improve the ohmic contact.

Figure 2-6: An ion milling system used for etching. Ar plasma is utilized for milling [63].

During the ion milling process, one of the challenges is the resist burning due to excess heat generated during the process. Therefore, the intensity and duration of the Ar ions bombarding onto the sample is controlled by the following steps.

1. The power of the ion beam is controlled, and lower current values for the beam current are used (45 mA beam current).
2. The substrate is mounted on a sample holder. To improve the thermal conductivity between the sample and the holder (which is water-cooled), we have utilized a vacuum grade thermal paste.
3. The duration of continuous ion milling is restricted to 15 seconds. The ion beam is shielded continuously for another 3 minutes for the sample surface to cool down before further milling process.

2.2.5 Pattering techniques

We have utilized lift-off and subtractive methods for pattern transfers which are discussed below.

2.2.5.1 Lift-off method

A bilayer resist technique is utilized for the lift-off method. Bilayer creates the undercut which makes the lift-off process easy. Two combinations of bilayer resists are used for our device fabrication and the details are discussed below.

In the first case, wafers are covered with a positive e-beam resist, Poly methyl methacrylate (PMMA) of different molecular weights – PMMA 495 and PMMA 950. A spin coater is operated at 6000 rpm which results to the resist thickness of ~ 120 nm and ~ 80 nm, respectively for the case of PMMA 495 and PMMA 950. Each layer of PMMA is baked at 180° C for 120 seconds to avoid inter-layer mixing.

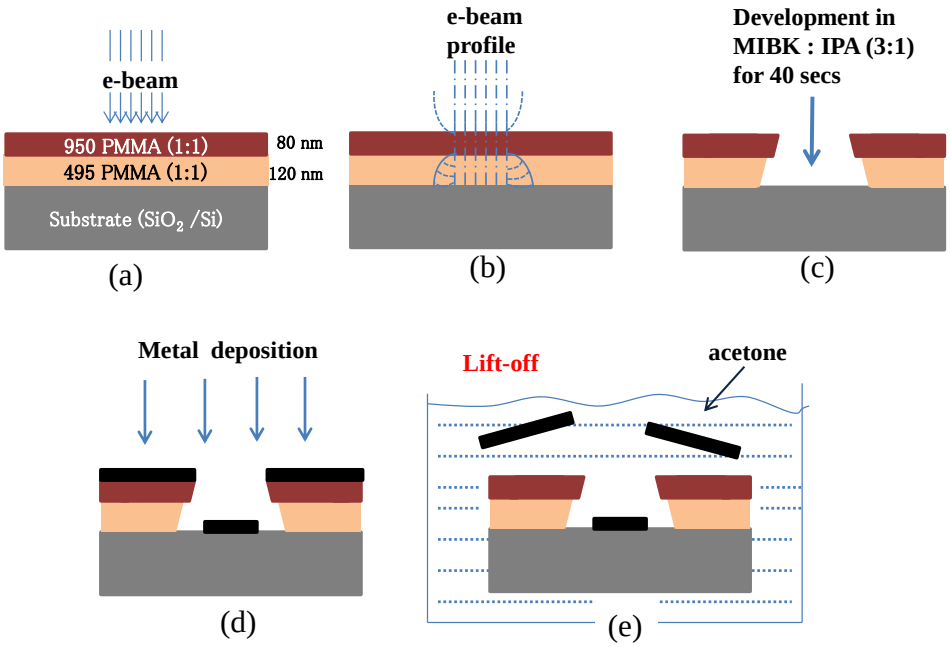

Figure 2-7: Lift – off process in details. (a) Exposure of e-beam for patterning. (b) E-beam profile – interaction of the resist with secondary and backscattered electrons. (c) The development process. (d) Metal deposition process. (e) Lift-off process. The unexposed resist with the metal on top is removed inside acetone.

The intended nanowire patterns are exposed on resist by EBL. The difference in molecular weight, together with the backscattered and secondary electrons creates a profile in PMMA as shown in Fig. 2-7. Developing, which is the process of removing the exposed resist, is done by immersing the wafer in a solution made from methyl isobutyl ketone (MBIK) and isopropyl alcohol with a ratio of 1:3 by volume. The process is optimized for 25 seconds. Subsequently, the wafer is immersed in IPA to stop further development process and blow dried by N_2. This creates the mask for the pattern transfer onto the wafer by the sputtering process.

The wafer is transferred into the sputtering load lock chamber as soon as possible to avoid contamination from the surrounding, and films are grown on the wafers using magnetron sputtering. Thereafter, the wafer is immersed into acetone for the lift-off process. Typically, an ultrasonic water bath operating at a low power is used to assist removal of EBL resist. The steps are shown in detailed schematics in Fig. 2-7.

The second combination of resists utilized for lift – off is MMA/PMMA (PMMA 950 on top) where the under layer (MMA) is not sensitive to the electron energy. The whole process is similar to the case discussed for the PMMA/PMMA case.

2.2.5.2 Subtractive method

For the subtractive method, MaN 2401 or MaN 2405 is spin coated on top of the deposited thin film. MaN 2401 yields a thickness of 100 nm at 6000 rpm. The resist is post baked at 90° C for 90 seconds. EBL is used to expose the desired patterns. Wafer is immersed in MaD developer for 40 seconds to develop the exposed pattern and rinsed with DI water followed by blow drying with research grade N_2. The exposed patterns remain, while the resist covering all the other unexposed area is removed by the developing process.

The pattern transferred wafer is loaded into the high vacuum ion milling chamber. Ar ion milling with a 45 mA beam current is typically used for pattering purposes for our sample conditions. The milling materials are detected by secondary ion mass spectroscopy (SIMS), and the milling process

is terminated at the desired depth of the material. For most of our samples, we had to etch through the multi-layers till the silicon substrate.

After the ion milling etching process is over, the resist is removed from the patterned structures by immersing the wafer into a negative resist remover. It should be noted that the negative resist removing process might be tedious. Most of the time, the removing process is performed in an ultrasonic bath with repeated visual inspection through the microscope available in the clean room. Temperature of the water bath is increased to assist the resist removal process. The steps involved in these processes are illustrated in Fig. 2-8. The wafer would undergo similar processes to make multi-layer lithography samples.

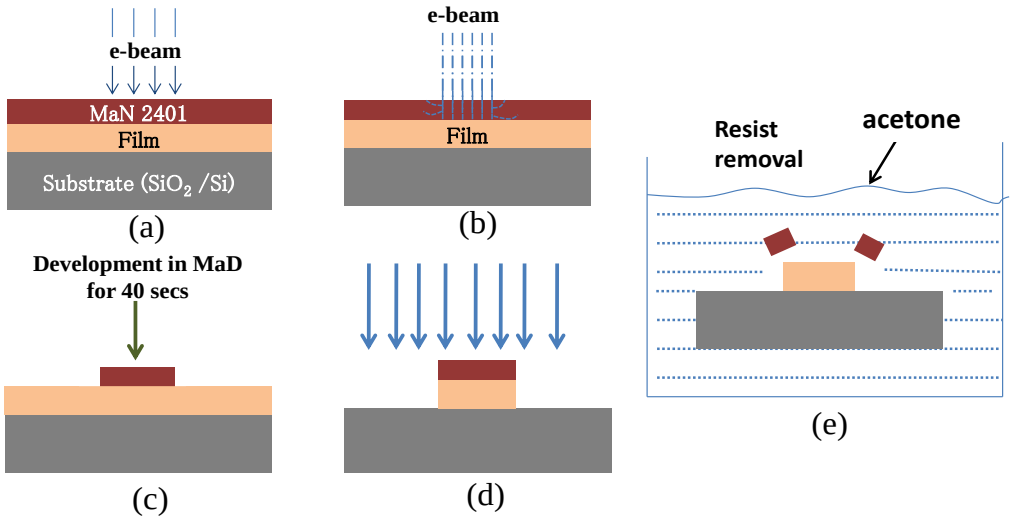

Figure 2-8: Lithography steps with negative resist. (a) The film coated with negative resist is exposed with the desired patterns by EBL. (b) Electron beam profile inside the resist with the backscattered and secondary electrons. (c) Developing the exposed patterns. (d) Ion milling process to remove the metal area not covered by EBL resist. (e) Removal of EBL resist in acetone or negative resist remover.

2.3 Structural and magnetic characterization techniques

2.3.1 Magnetic force microscopy (MFM)

Magnetic force microscopy (MFM) is widely used for imaging the domain structure in magnetic materials. Even though the types of domain wall can be distinguished by AMR measurements, it cannot be correlated without imaging the domain structure. Thus, MFM becomes a critical tool in domain wall research. The key to a successful MFM imaging lies in separating the magnetic signal from the other signals. To achieve this, MFM is commonly used in 'lift mode' of the atomic force microscopy system. The working principle of MFM is shown in Fig. 2-9. At first, the topography information of the surface is recorded and then the tip is lifted by a predefined distance of 10 nm – 200 nm and the magnetic information is recorded. The magnetic forces cause a phase shift over different domains during the lift-mode scan. Most of the forces decay more rapidly with distance than the magnetic interaction. However, the electrostatic forces are an exception which is usually distinguishable from the magnetic contrast. Only the long range magnetic force will be the dominating factor in the lift mode.

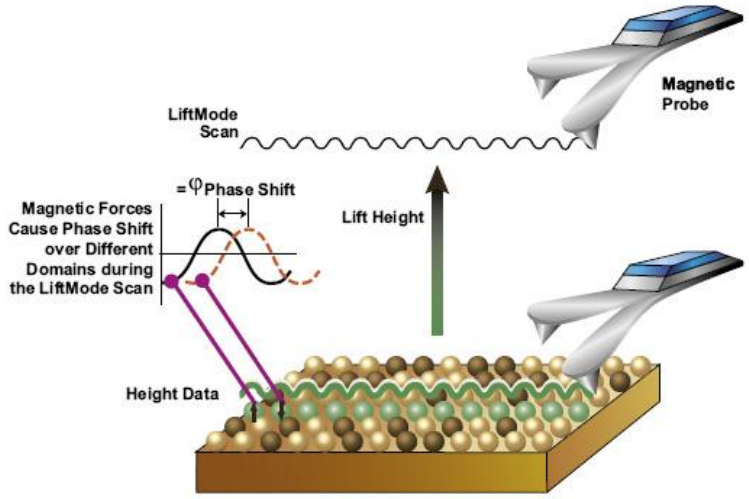

Figure 2-9: Working principle of an MFM system. First the topographic information is recorded, and then the lift-mode scan is performed [65].

Even though MFM technique can go down to the resolution of 25 nm, it has its own drawbacks. Firstly, MFM does not probe the magnetization but rather the dipole fields generated by inhomogeneities in the magnetization. For

samples magnetized in-plane, these fields are approximately proportional to the divergence of the magnetization. This means that it can be difficult to resolve the structure of complex DWs from an MFM image without the help of micromagnetic simulations. Secondly, the interaction between the magnetized MFM tip and the sample is often large enough to perturb the magnetic structure of the sample. The field from the tip can both distort and cause transformations in the structure of DWs [66]. Furthermore, it can drag DWs along a nanowire, even if the DWs are trapped at pinning sites [67]. Therefore, tips should be carefully chosen for experiments.

For our studies, low moment tips are utilized for imaging soft magnetic materials such as permalloy, and high moment tips are utilized for Co/Pd multilayers. We have used a Veeco® scanning probe microscopy system for our experiments as shown in Fig. 2-10.

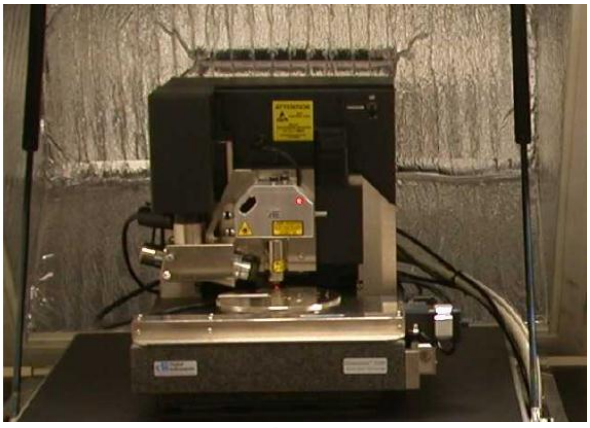

Figure 2-10: Veeco® scanning probe microscopy system. The system is shielded during measurements isolate the measurement system from the outside magnetic noise.

2.3.2 Superconducting quantum interference device (SQUID)

A superconducting quantum interference device (SQUID) is a highly sensitive magnetometer used to measure extremely subtle magnetic flux. This technique consists of two superconductors separated by thin insulating layers to form two parallel Josephson junctions as shown in Fig. 2-11.

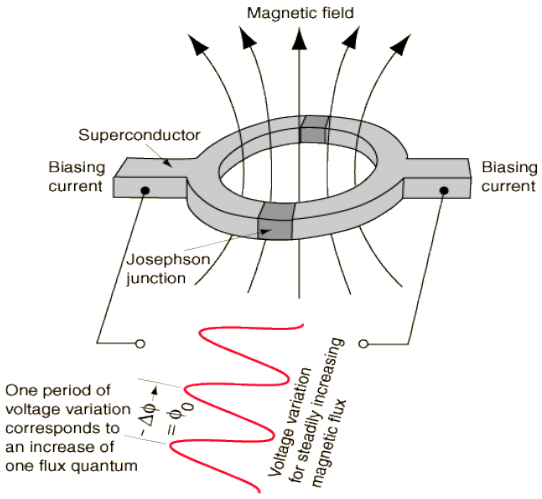

Figure 2-11: Working principle of a SQUID [68].

When a constant biasing current is maintained in the SQUID device, depending on the change in magnetic flux, the measured voltage oscillates with the changes in phase at the two junctions. The flux change can be calculated by counting the number of oscillations. In an ideal scenario SQUID can detect magnetic fields as small as 1×10^{-15} T. Commercial SQUID systems could reach a sensitivity of 1×10^{-12} T [68].

Figure 2-12: SQUID – MPMS system used for measurements [69].

A commercially available SQUID – MPMS system from Quantum Design was used for the studies in this thesis as shown in Fig. 2-12. It can be

operated in the temperature range of 2 to 400 K and a field range of +/- 9 T with a field resolution of 0.05 Oe.

2.4 Electrical characterization

Most of the presented work primarily involves transport measurements. Probe based systems provide easier means of electrical characterization. A probe-station was used for four probe based measurements which can house 4-separate probes with an in-plane magnetic field as shown in Fig. 2-13. The maximum field limit is +/- 800 Oe. A microscope connected the screen helps to place the probes on the micron-sized contact pads.

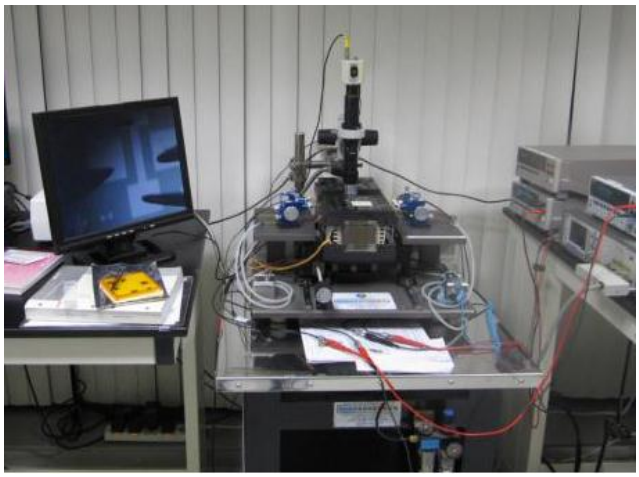

Figure 2-13: Four probe station utilized for dc- and ac-measurements.

When the measurement requires more than 4 connections, we have utilized a He4 cryostat system as shown in Fig. 2-14(a), in which ac and dc measurement systems are visible on the rack. A wire bonded sample to the sample holder is shown in Fig. 2-14(b). The He4 cryostat chamber provides better shielding from the outside noise sources and can be operated at a high vacuum of 10^{-6} Torr. The measurement chamber of the cryostat is placed between two electromagnet poles, which provide a maximum magnetic field of ~ 8 kOe. The electromagnets are placed on a rotating platform which gives the freedom to apply magnetic field in any desired angle.

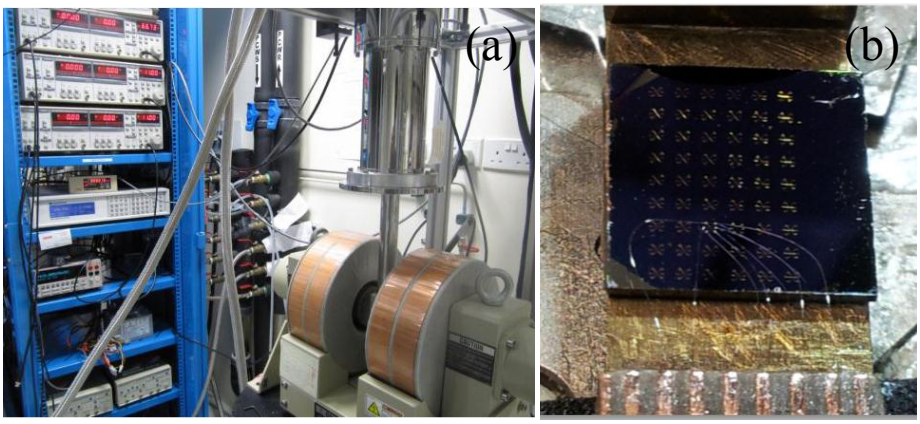

Figure 2-14: (a) He4 cryostat system with magnetic poles. Ac and dc measurement and control equipment are visible on the rack. (b) Electrodes on the substrate are wire bonded to the terminals in the sample holder. 8-terminals can be used for measurements.

Chapter 3 : Domain wall characterization

3.1 Introduction

Domain wall generation and domain wall control through pinning are important aspects in domain wall based device applications. We characterize various DW generation methods and field induced DW motion in in-plane and out-of-plane nanowires using different detection mechanisms, such as magnetic force microscopy and electrical measurements. Permalloy and Co/Pd multilayer nanowires are used for in-plane and out-plane experiments, respectively.

3.2 Field driven domain wall motion in permalloy nanowires

Permalloy nanowires were fabricated from the sputter grown samples with the structure of substrate/Al_2O_3 (5 nm)/NiFe (30 nm)/Al_2O_3 (5 nm). Semi-circular nanowires were fabricated using the subtractive method discussed in section 2.2.5 with nanowire widths ranging from 300 to 800 nm and a diameter of 50 μm.

In the following section, two types of vortex DW configurations – head to head (HH) and tail to tail (TT) DWs are generated utilizing the shape anisotropy, and the depinning field strength is determined by MFM.

3.2.1 Domain wall generation by shape anisotropy

A HH – DW is generated by applying a saturation magnetic field H_{SAT} along the *x*-direction as shown in Fig. 3-1. At high magnetic fields, the magnetic moments align along the direction of the external magnetic field. When the magnetic field is gradually reduced, the magnetic moments would relax to its original state. However, due to the shape anisotropy, magnetic moments tend to align along the nanowire. Therefore, the spin configurations

lead to an opposite alignment of magnetic moments as shown in Fig. 3-1(b). If the magnetic moments face each other, the configuration is defined as a head to head (HH) DW as shown in Fig. 3-1(c). By applying the same sequence in the opposite direction (apply saturation magnetic field in –*x*-direction and gradually reduce to zero), a tail to tail (TT) DW can be generated as shown in Fig. 3-1(d), in which the magnetic moments face the opposite direction [10].

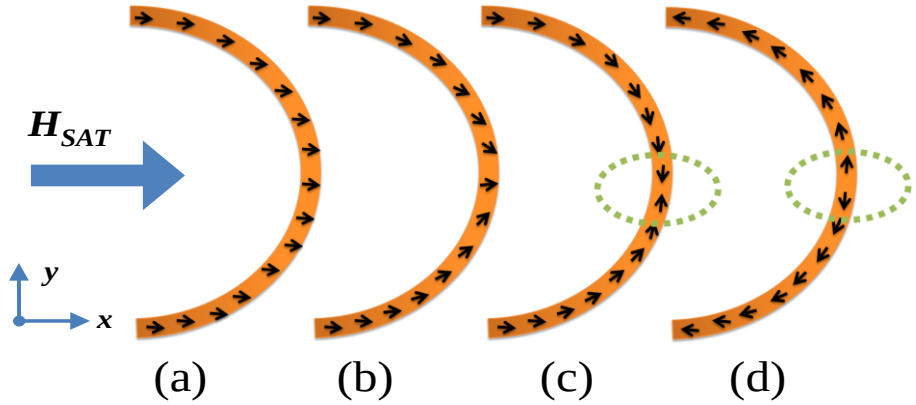

Figure 3-1: Generation of a DW by magnetic field utilizing the shape anisotropy. (a) Saturation magnetic field is (H_{SAT}) applied along *x*-direction. (b) Alignment of magnetic moments when the applied field is gradually reduced. The magnetic moments stay parallel to the nanowire edges due to shape anisotropy. (c) The dotted area shows a generated HH-DW after the field is removed. (d) A TT-DW is formed with saturation magnetic field in –*x*-direction.

3.2.1.1 Experimental setup

An electromagnet is used for applying the external magnetic field. MFM is performed in ambient conditions in a Veeco® scanning probe microscopy system. Commercially available low moment magnetic tips coated with CoCr alloy are used for imaging, in order to minimize the influence of the tip on soft-magnetic material, NiFe as discussed in section 2.3.1.

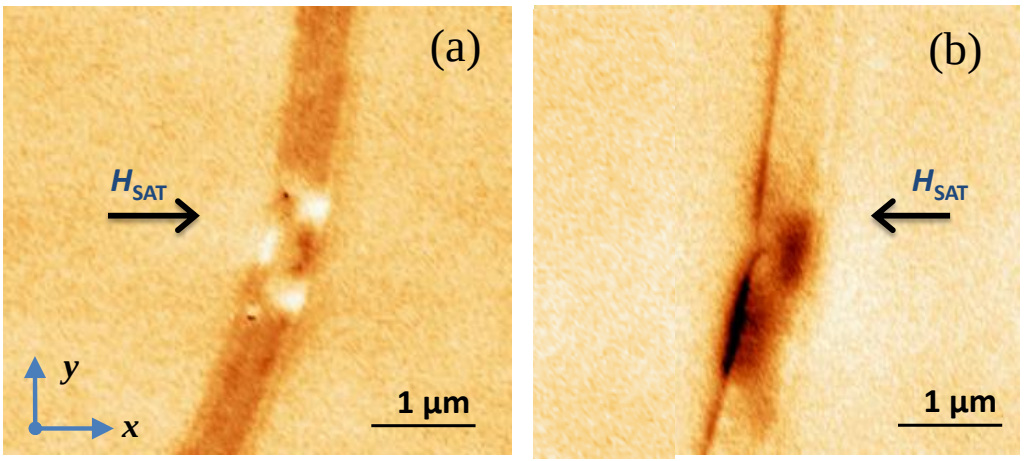

Figure 3-2: MFM images show a HH and TT – DW configuration formed after saturating the nanowire (width: 700 nm) in the +*x*- and –*x*-direction, respectively.

A saturation magnetic field of H_{SAT} = 4 kOe is applied along the +*x* and –*x*-direction as shown in the Fig. 3-2 and the field is reduced to zero before removing the sample from the probe station. Extra care was taken to minimize the stray or residue magnetic field. Figure 3-2(a) and (b) show a HH and a TT configuration of a vortex DW, respectively. We can clearly observe the magnetic contrast between the two images in (a) and (b). The MFM tips are magnetized in the same direction by using a specially designed permanent magnet for two minutes for both the experiments prior to the measurement. Therefore, the opposite magnetic contrast, bright and dark, represents the opposite alignment of magnetic moments. The stray field emanating from the DW structure points up (bright) and down (dark) for the HH and TT – DW configurations, respectively.

3.2.2 Field driven motion of head to head DWs

The field driven motion of a HH-DW is studied by MFM. A HH-DW is generated using the sequence described in section 3.2.1. In order to move the DW, an external magnetic field (H_A) is applied at an angle 30° away from vertical axis as shown in Fig. 3-3. At each step, prior to performing MFM measurement, the sample is taken away from the AFM system, and a magnetic field H_A is applied and reduced to zero. H_A is increased in steps of 10 Oe, until

the DW is removed from the position. At 70 Oe, the DW has disappeared from its position.

It can be seen from the images that the DWs structure goes through a gradual change with the application of external magnetic field. Even though the applied field is not sufficient to depin the DW from the pinning center, it causes the DW to expand. When the external field is removed, the structure still remains expanded and distorted. The roughness at the edges of the nanowire could play a role for this behavior. The DW expansion with magnetic field is shown in micromagnetic simulations in 4.3.2.

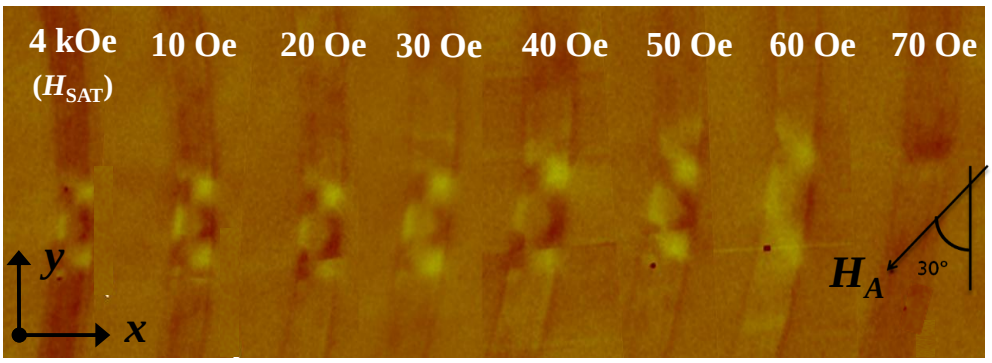

Figure 3-3: MFM images of depinning a HH-DW by external magnetic field, H_A applied in the depicted direction. At 70 Oe, the DW is depinned from the pinning site.

3.2.3 Field driven motion of tail to tail DWs

In this experiment, a TT – DW is generated as discussed in section 3.2.1 and its configuration is confirmed by the contrast of MFM images as shown in Fig. 3-3. The field strength required for depinning the TT – DW is lower than that of the HH – DW from the same pining site, which is similar to the reported values [28]. Depending on the configuration of the DW and the geometry of the pinning site, the depinning profile significantly changes. The pinning site influence on the depinning strength is studied in chapter 4.

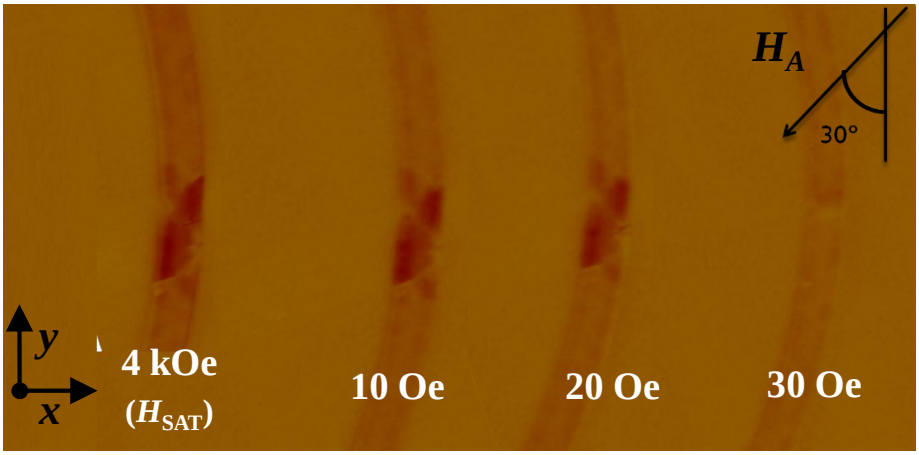

Figure 3-4: MFM images of depinning a TT-DW by external magnetic field, H_A applied in the depicted direction. At 30 Oe, the DW is depinned from the pinning site.

3.3 Electrical characterization of magnetic DWs

Various measurement schemes are employed to characterize DWs in nanowires. Optical measurements such as magneto optic Kerr effect (MOKE) [70] and electrical detection methods such as giant magnetoresistance (GMR) [35], anisotropic magnetoresistance (AMR), and Hall measurements are commonly used. The position of a DW in a nanowire can be detected by MOKE or GMR techniques. Electrical methods are fast and reliable, and it is also extensively used for studies on DW dynamics. In the following section, we utilize a quasi-static resistance measurement set-up using lock–in amplifiers and Keithley current source meters to detect DWs.

3.3.1 Measurement set up

Nanowires with the nucleation pads shown in Fig. 3-5 are fabricated from the film stack of substrate/Ta (5 nm)/NiFe (30 nm)/Ta (4 nm). Ta is used as an underlayer to improve the adhesion and to provide a smooth template for growth. Ta is also used as a capping layer to prevent oxidation. The design geometry shown in Fig. 3-5(a) is adopted from the work presented by Hayashi *et al.* [71]. The four pads (A_1, A_2, B_1, and B_2) are spaced in such a way, suitable for GSG high frequency probes. Two dc pads (C_1, C_2) are also added for *dc* measurements. The ground plane around the device acts as a common

ground for various GSG configurations. It also helps to reduce measurement noise.

Lock in technique provides the ability to detect a very small resistance drop which arises from the DW presence in the nanowire due to the change in AMR. The measurement schematics are shown in Fig. 3-5. A voltage source from the lock-in amplifier is connected in series with a resistor (R_{EX}), to convert the voltage source into an effective current source. The effective four probe configuration is shown in Fig. 3-5.

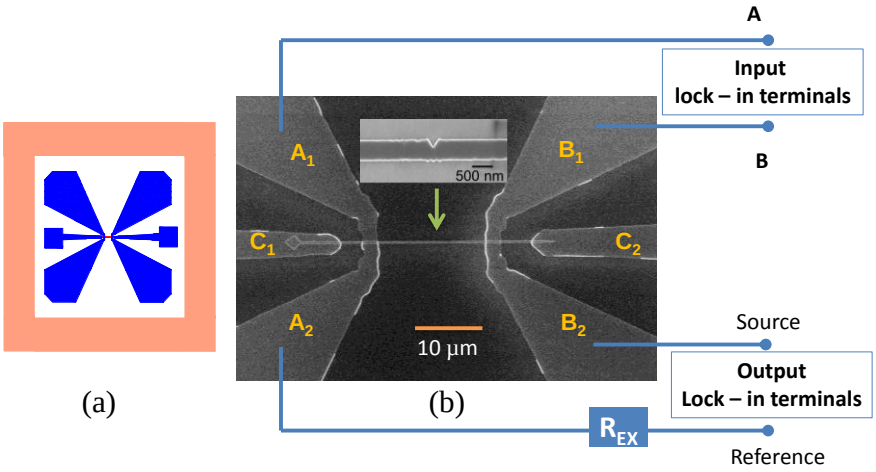

Figure 3-5: (a) The measurement pad design with nanowire at the center. The inset shows a representative notch. (b) SEM image of the device with four probe measurement scheme. A lock in amplifier with an external resistance (R_{EX}) is connected to the nanowire.

3.3.2 DW generation with nucleation pad geometry

A single DW is generated and pushed to the notch located in the middle of the nanowire by means of a nucleation pad. In the case of shape anisotropy based DW generation in semicircular or V shape nanowires, a vector magnetic field is required to study the field driven DW motion. On the other hand, for the nucleation pad method, magnetic field along one direction is enough to study DW generation, propagation, and detection without requiring complex magnetic field systems [72].

Figure 3-6 shows the sequence of generating a DW and subsequently pinning it at the notch. At first, the nanowire is saturated along H_{SAT} as shown in Fig. 3-6(a). When an increasing H_{NUC} is applied along the $-x$-direction, the magnetization on the pad region starts to reverse, thus forming a DW at the

mouth of the nanowire as in Fig. 3-6(b). This is due to the fact that larger area has a lower coercivity due to the lower shape anisotropy. When H_{NUC} further increases, the DW is released from the mouth of the nanowire. As the pinning potential of the notch is higher than the mouth of the nanowire, the DW is pinned at the notch as in Fig. 3-6(c). Further increase in H_{NUC} overcomes the energy barrier at the notch, and the DW is released from the notch and annihilated. The resultant magnetization configuration is shown in Fig. 3-6(d).

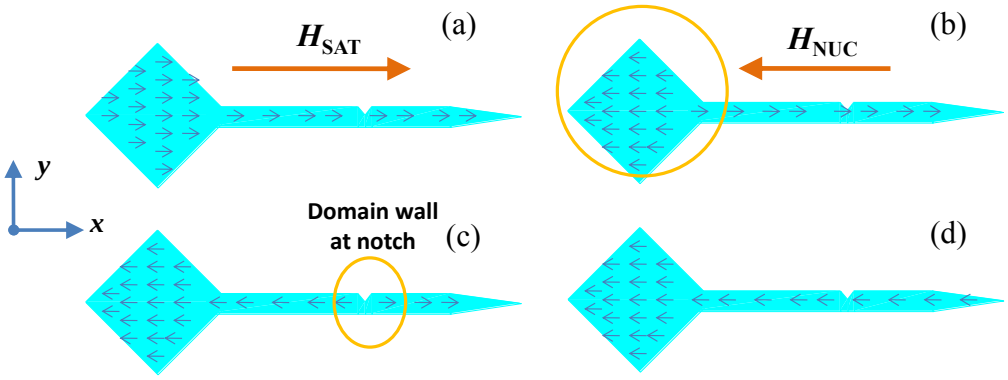

Figure 3-6: Generation of a DW utilizing the nucleation pad geometry. (a) The nanowire is saturated along +*x*-direction. (b) When H_{NUC} is applied, the pad reverses first and a DW is formed at the mouth of nanowire. (c) Further increase in H_{NUC} releases the DW and subsequently pushes the DW towards the notch. (d) The entire wire is saturated along the –*x*-direction.

AMR response of a permalloy nanowire (700 nm wide and 65 µm long) with an input sinusoidal current of 20 µA is shown in Fig. 3-7(b). The magnetic field is swept from H_{max} to H_{min} and back to H_{max} to form a loop. The magnetic reversal process of the nanowire is observed clearly.

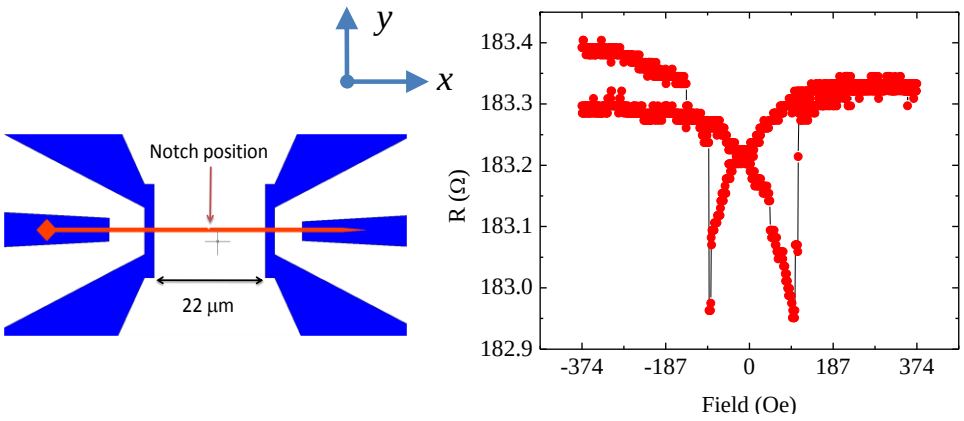

Figure 3-7: (a) Device structure with the notch position. (b) AMR response of a 700 nm wide nanowire with magnetic field.

3.3.3 Domain wall resistance

The presence and absence of DW can be detected by AMR. When a DW is present, the DW lowers the resistance of the nanowire. AMR change due to a DW is very small, thus it is easy to be ignored. The following sequence is employed to detect the DW resistance.

First, the nanowire is saturated by H_{SAT} (700 Oe) in the +*x*-direction and reduced to zero. R_{SAT} is recorded at zero fields. Then, a nucleation field, H_{NUC} is applied in the –*x*-direction and reduced to zero, and then the R_{NUC} is recorded [73]. The whole cycle is repeated as the nucleation field (H_{NUC}) increases from 100 to 200 Oe at 5 Oe steps. The field cycle is described in the Table 1. At every step, 30 points are taken at an interval of one second and averaged to improve the signal to noise ratio.

Cycle	Field	Resistance
1	H_{SAT}	
2	0	R_{SAT}
3	$-H_{NUC}$	
4	0	R_{NUC}

Table 3-1: The measurement sequence and field cycle employed to detect the DW at the notch.

DW resistance is given by the following relation, $R_{DW} = R_{SAT} - R_{NUC}$. Figure 3-8 shows repeated measurements at $H_{NUC} = -45$ Oe. 30 recordings of R_{SAT} and R_{NUC} are continuously plotted where *x*-axis is the arbitrary time. As can be seen from the plot, there is no drop in values between R_{SAT} and R_{NUC} since $H_{NUC} = -45$ Oe is well below the required nucleation field to generate a DW. However, at $H_{NUC} = -130$ Oe, a clear drop in resistance values is observed as in Fig. 3-8(b). It can be inferred that a DW is trapped at the notch, and the DW resistance, R_{DW} is ~ 0.2 Ω. The linear increase in ΔR can be attributed to thermal drift. This observation is further confirmed by MFM measurements. After a successful DW pinning at the pinning site, the sample is removed from the probe station and MFM is performed. A representative MFM image is shown in Fig. 3-9. A single DW is clearly visible at the pinning site.

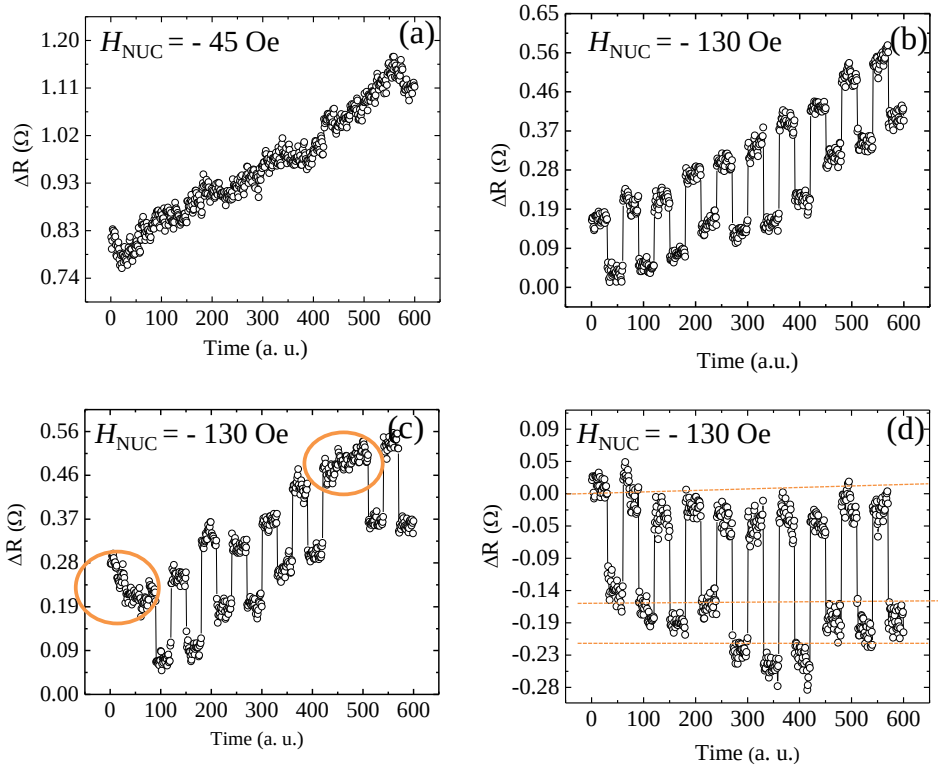

Figure 3-8: Repeated measurements following the scheme shown in Table 1 with H_{NUC} = -45 Oe (a) and H_{NUC} = -130 Oe (b-d). (b) DW generation failures are highlighted. (d) Different resistance levels observed for generated DWs.

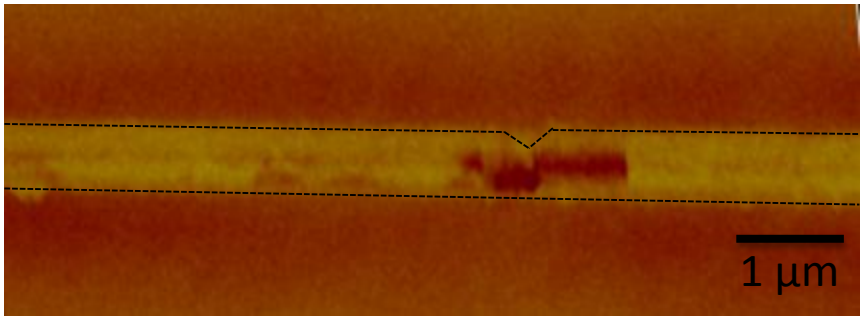

Figure 3-9: MFM image shows a DW trapped at the pinning site by the pad nucleation method. The notch position in the nanowire is also shown.

The DW generation is a stochastic process [74]. Figure 3-8(c) shows such a behavior with H_{NUC} = -130 Oe. The highlighted parts show that a DW is not generated in that field sequence. Two scenarios can explain this observation. One is that the DW is pinned at the mouth of the nucleation pad and it is not released. The other reason is that the DW is released from the pinning site without pinning [75]. It is expected that the nanowire geometry favors a vortex wall at the pinning site. However, due to the effect of notch geometry and edge roughness, four types of DW configurations including

chirality can be formed. This is evident from Fig. 3-8(d) where R_{DW} shows two clear distinct states. Those two distinct states could correspond to a transverse DW and a vortex DW as discussed section 1.6.1.3. Detailed studies of DW generation and DW pinning are presented in chapter 4.

3.3.4 DW generation by Oersted field generation method

In the following section, we discuss the DW generation procedure utilizing the Oersted field generation method. Oersted fields generated by a current carrying conductor can be used to switch the magnetization of a nanowire placed below the current carrying conductor. Two cases of Oersted field generated in a current carrying conductor are shown in Fig. 3-10(a) and (b). When the magnetization of the nanowire (M) and the generated Oersted field are in the anti-parallel alignment, the magnetization (M) of the magnetic nanowire portion as highlighted in Fig. 3-10(b) can be reversed, thus forming two domain walls. However, in the case of both magnetization and the Oersted field are parallel, no DW will be generated as shown in Fig. 3-10(a).

The magnetic field due to the current passing through the conductor has H_x and H_z components. The Karlqvist equations which are commonly used in the recording media can be modified to calculate the magnetic field components which results in [76, 77]

$$H_x(x,z) = H_0[\arctan(\frac{(\frac{W}{2}+x)}{z}) + \arctan(\frac{(\frac{W}{2}-x)}{z})]$$
$$H_z(x,z) = \frac{H_0}{2}[\frac{(\frac{W}{2}-x)^2+z^2}{(\frac{W}{2}+x)^2+z^2}] \quad (3.1)$$

A resultant Oersted field profile is shown in Fig. 3-10(c). The effective field in the *x*-direction plays a main role in reversing the magnetization.

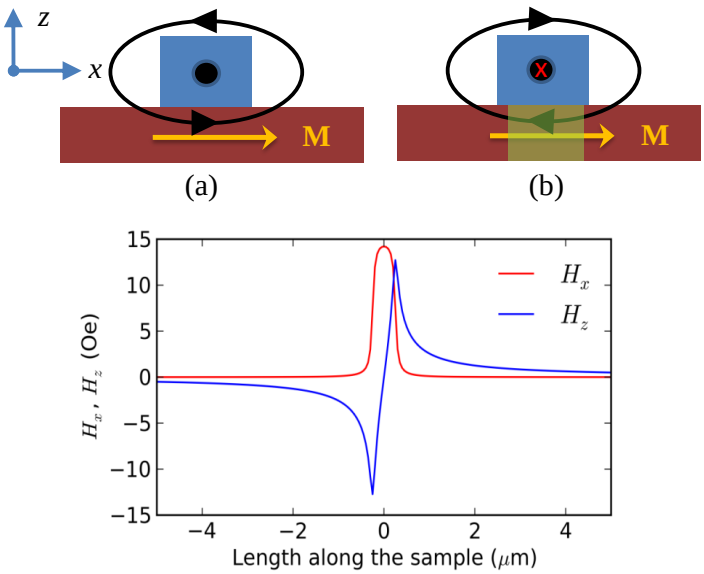

Figure 3-10: Schematics of Oersted field generated by a current carrying conductor. The generated Oersted field is in the (a) parallel and (b) anti-parallel with magnetization underneath the conductor. (c) The Oersted field profile of H_X and H_Z along the length of the sample.

Micromagnetic simulations are performed using OOMMF to study the Oersted field based DW generation process. A permalloy nanowire, with the dimensions of 10 µm × 500 nm × 30 nm, is placed 40 nm (center to center) beneath a current carrying conductor as shown in Fig. 3-11(a). The width and the thickness of the conductor are 500 and 50 nm respectively. A current pulse with a pulse width of 5 ns is applied through the current carrying conductor. The rise time and fall time are fixed at 40 ps. After the pulse, the system is set to relax. Subsequently, two vortex DWs are formed on both sides of the current carrying conductor as can be seen in Fig. 3-11(b).

The experimental schematics for the DW generation are shown in Fig. 3-12(a). A nanowire [Ta (5 nm)/NiFe (30 nm)/Ta (3 nm)] with a pinning site at the center is patterned with electrodes as discussed in section 2.2.5. A dc source meter (Keithley 2400 across CD contacts) and a nano-voltmeter (Keithley 2148A across CB contacts) are connected in parallel to measure the voltage drop.

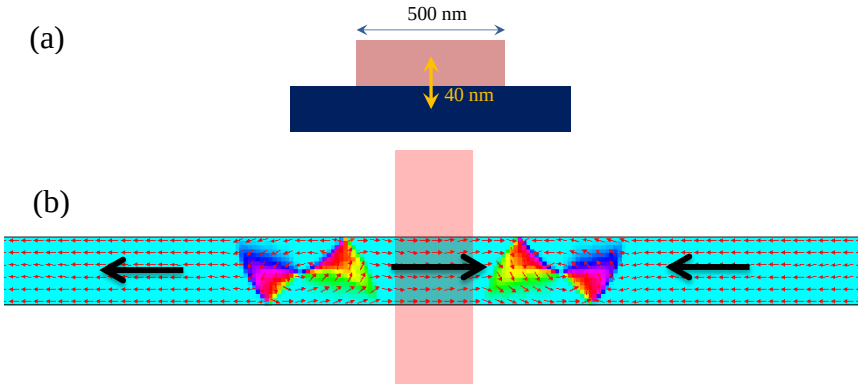

Figure 3-11: (a) Cross sectional view of simulation setup – a current carrying conductor is placed on top of the magnetic nanowire. (b) After the current pulse is applied, a portion of the magnetic nanowire is reversed, resulting in two vortex DWs. The arrows indicate the direction the magnetization.

The sequence described in Table 3-2 is used to generate a DW in the nanowire. First, the nanowire is saturated with H_{SAT} in the $-x$-direction and slowly reduced to zero. Then, the resistance across CB terminals is measured (R_{SAT}). After that, a short pulse is applied at electrode A to generate a DW while H_{INJ} ($+x$-direction) is ON. The magnetic field is brought back to zero and the resistance across CB is measured again (R_i). The DW resistance is given by $R_{DW} = R_{SAT} - R_i$.

Cycle	Field	Resistance
1	$-H_{SAT}$	
2	0	R_{SAT}
3	H_{INJ}+ DW gen pulse	
4	0	R_i
5	H_{SAT}	

Table 3-2: Field sequence applied for during measurements to generate and detect DWs. The resistance levels measured at the corresponding fields is shown on the right column.

The five possibilities of magnetic reversal in the nanowire are shown in Fig. 3-12(b). They are:

(i) Only the portion below the electrode is reversed, thereby forming two DWs.

(ii) Due to the injection field (H_{INJ}), the DW on the left can overcome the pinning strength and gets annihilated, resulting in a single DW.

(iii) The DW can move towards the pinning site and gets pinned due to the higher potential barrier.

(iv) The moving DW overcomes the pinning barrier and the whole nanowire is reversed.

(v) The generated field by the pulse is not sufficient to reverse the nanowire – no DW is generated.

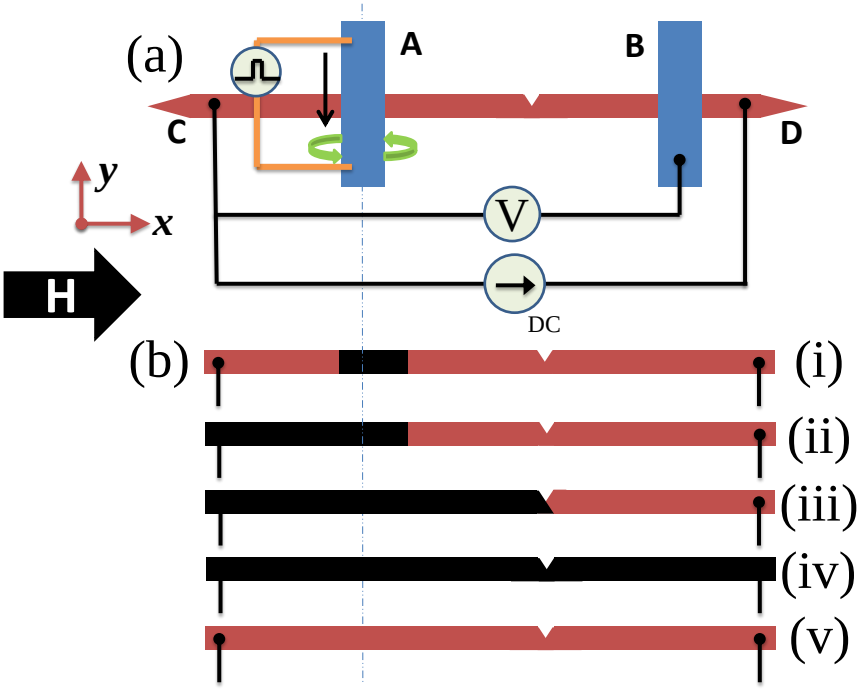

Figure 3-12: (a) Measurement schematics for DW generation and detection. (b) Five possible magnetization states after the DW generation pulse.

The above discussed states could be identified by monitoring the resistance values across CB contacts by the following procedure. After the DW generation sequence, an increasing magnetic field is applied in the +x-direction to drive the DW out of the nanowire. The possible magnetic state and its profiles are shown in Fig. 3-13.

(a) Two DWs are generated. With increasing the magnetic field, the DW on the left moves out of the nanowire and the nanowire reaches a state similar in Fig. 3-13(b). This is evident from the first

step (1→2) in the plot. When the magnetic field further increases, the DW on the right is driven out of the nanowire (2→3). It can be further noted that the total increase of the resistance (1→3) is twice as that of the first step (1→2) confirming the existence of 2 DWs.

(b) The profile when a single DW is generated. Irrespective of the position of the DW, the resistance values remains the same as shown in Fig. 1-13(b).

(c) When the whole nanowire is reversed, the increase in the magnetic field does not show any changes as shown in Fig. 1-13(c).

(d) A failure in DW generation. The nanowire goes through a normal reversal process as shown in Fig. 1-13(d).

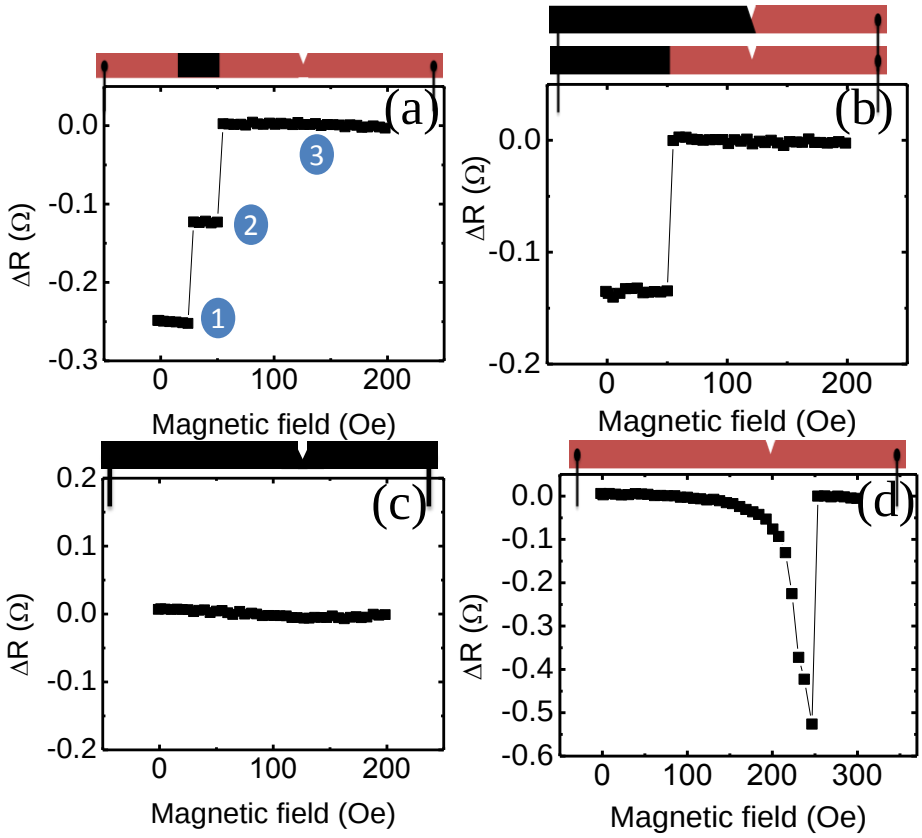

Figure 3-13: Resistance values across CB. (a) Two DWs are generated. (b) A single DW generated. (c) Whole nanowire is reversed. (d) No DW was generated.

A detailed study in pinning site and its stochastic behavior is presented using the above techniques in Chapter 4.

3.4 Field driven domain studies in perpendicular magnetic anisotropy (PMA) systems

DWs in PMA systems offer superior qualities for device applications as discussed in chapter 1. In the following section, perpendicular magnetic anisotropy systems are investigated for DW applications. Attempts are made to generate a single DW which is detected with MFM and electrical measurements.

3.4.1 Experimental setup

A pinning site for DW in a PMA nanowire can be achieved by introducing thickness variation, especially, in a multilayer system. In a Co/Pd multilayer system, the interface anisotropy is strong enough to overcome the macroscopic shape anisotropy and induces a perpendicular easy axis of magnetization. Therefore, in order to control the magnitude of anisotropy, one has to tailor the properties at the interfaces. In our study, anisotropy is controlled by manipulating the number of multilayers. A thickness variation is introduced by creating a vertical step-like structure in the nanowire [78]. This step is created by etching out a portion of the nanowire by ion milling while masking the other part of the nanowire.

3.4.2 Sample preparation

Nanowires are fabricated from films grown by magnetron sputtering with a structure of substrate/Ta (4 nm)/Ru (20 nm)/[Pd (0.7 nm)/Co (0.2 nm)]$_{22}$/Ta(4 nm). The subtractive method is used (as discussed in section 2.2.5) for the nanowire fabrication. In the second step, partial etching is done to form the step like topography. The partial etching mask is shown in Fig. 3-14(a). The estimated etched thickness by AFM is 10 nm. Finally, electrical pads are patterned on top of the nanowire. The resultant device structure is shown in Fig. 3-14(b).

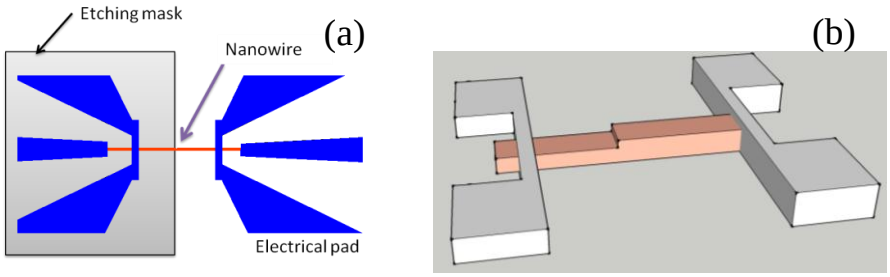

Figure 3-14: (a) Mask patterns for etching. (b) Device schematics with a step in the middle of the nanowire.

After the samples were prepared as described above, MFM images were taken to ascertain the status of the magnetic domain structures in the nanowire. Multiple domain structures were observed as in Fig. 3-15(b) confirming the magnetic properties of the nanowire with a clear contrast compared to the topography image in Fig. 3-15(a).

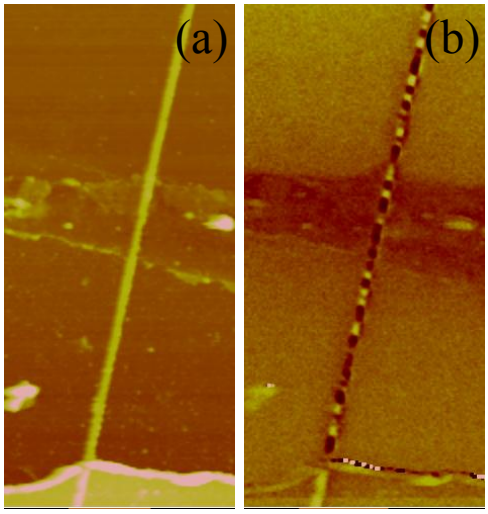

Figure 3-15: (a) Topography and (b) Phase diagram of a freshly prepared Co/Pd multilayer nanowire with the step like structure. Multi-domain structure is clearly visible.

Measurements in AMR configurations were carried out using the schematics shown in Fig. 3-16(a). The nanowire reversal process is observed, when magnetic field is swept in the out-of-plane direction. The points indicated by a red arrow in Fig. 3-16(b), in the middle of the reversal curve could reflect DW pinning in the middle the nanowire. This helps to identify the required magnetic field to apply to create a single DW at the step-feature.

To verify the DW at the step, MFM images were taken at different points around the abrupt switching area as highlighted by the arrow in Fig. 3-16(b).

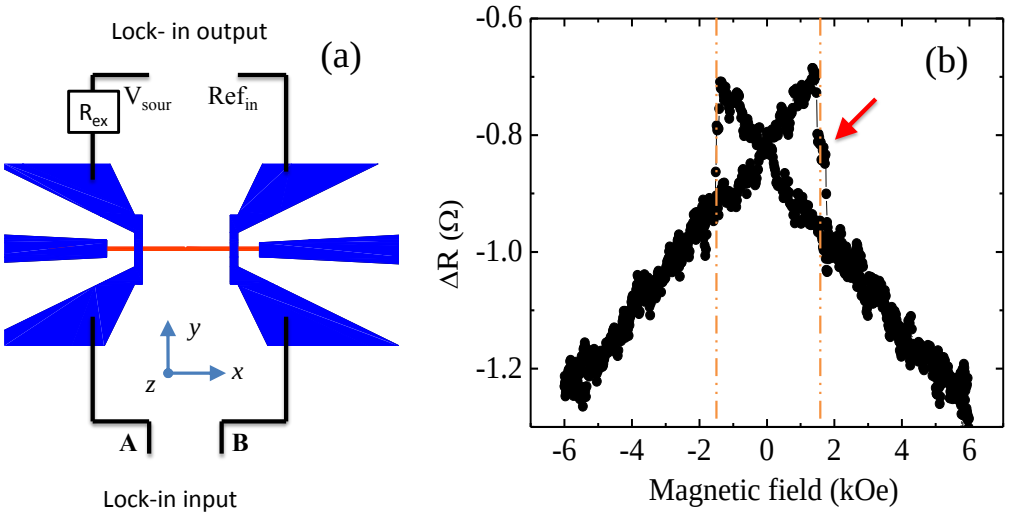

Figure 3-16: (a) AMR measurement schematics. (b) AMR measurement with magnetic field applied in the out-of-plane direction.

MFM images shown in Fig. 3-17(a) were taken right after stopping at a nucleation field, H_{NUC} = 1.55 kOe (after the nanowire was saturated with H_{SAT} = - 6 kOe). A DW is clearly visible at the step (circled) with the contrast difference of a bright (magnetization pointing upwards) and dark (magnetization pointing downwards) region. When the H_{NUC} is further increased to +6 kOe, the DW has depinned from the step-pinning site as seen in Fig. 3-17(b) and the whole nanowire is saturated in the out-of-plane direction.

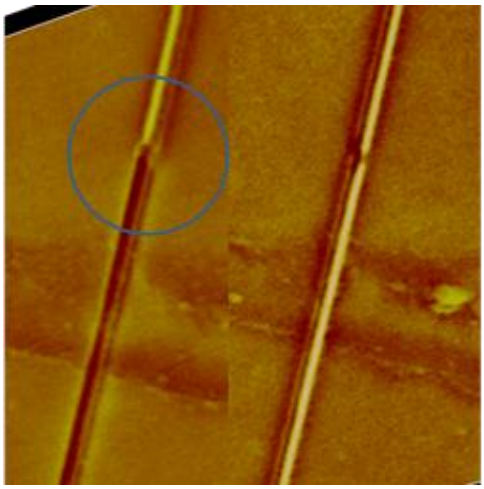

Figure 3-16: (a) Phase diagram of a single DW pinned at the edge of the step (circled). (b) Phase diagram after saturation.

This DW generation method, however, is more suitable for thick multilayer structures. Moreover, the etching process introduces a significant amount of unwanted roughness along the surface which may hinder the performance of the device. For the ultra-thin tri layer structures, this method would not be feasible. We have studied an alternative method to generate DWs in chapter 5 utilizing the Joule heating.

3.5 Summary

DW generation and detection in in-plane (NiFe) and out-of-plane (Co/Pd multilayers) were explored in this chapter. MFM studies provide DW structures in permalloy nanowires. The electrical measurement schemes are established for DW generation and detection which will be further utilized in chapter 4, 5, and 6.

Chapter 4 : Domain wall pinning at nanotrench pinning sites

4.1 Motivation

The design of pinning sites is crucial for the control of domain walls in nanowires. The most common approach to pin a domain wall is by introducing a constriction along the width of the nanowire. The parameters such as pinning fields and pinning potentials highly depend on the notch dimensions. However, the reproducibility and control of lateral dimensions are quite challenging lithographically.

In this chapter, we investigate an alternative approach to pin a domain wall with lower lithography requirements. The pinning sites are created by etching out a selected portion of the magnetic nanowire, thus forming a vertical nanotrench across the whole width of the nanowire in contrast to the conventional approaches with a lateral trench across the small portion of the nanowire.

4.2 Introduction

Domain wall (DW) based devices have been proposed as a promising solution for future high density storage and logic devices [8, 9, 35, 79-81]. Implementing these devices requires precise and reliable control of DWs which can be achieved through pinning centers. Automotion happens in ideal nanowires [36], however, in reality, lithographic imperfections in nanowires results in natural pinning sites which are inherently hard to control. Controllable pinning sites can be introduced by engineering artificially structured variations into the geometry along the nanowires, which are known as “notches”. Complex DWs are formed at these notches and its depinning behavior is very sensitive to the initial state of the DW, its structure, and

chirality as well as the excitation method [28, 36, 82, 83]. Even the stochastic behavior of the pinning and depinning process can be controlled by varying the notch dimensions [84]. Static and dynamic pinning strengths for a DW at the pinning sites have also shown deviations [85]. All these results show that the control of DWs depends predominantly on the notch profile.

A few mechanisms are typically used to pin and control a DW in ferromagnetic nanowires of in-plane anisotropy systems. Ion irradiation is an approach in which a portion of the nanowire is implanted with ions to soften the magnetic properties, thereby creating a pinning site [86, 87]. The common approach is to introduce lateral constrictions along the nanowire, as a result, giving rise to a notch [88] or alternatively a lateral protrusion known as anti-notch [85]. However, in nanowires, it is lithographically challenging to precisely control the lateral dimensions at the nanoscale. Examples of notch and anti-notch are shown in Fig. 4-1.

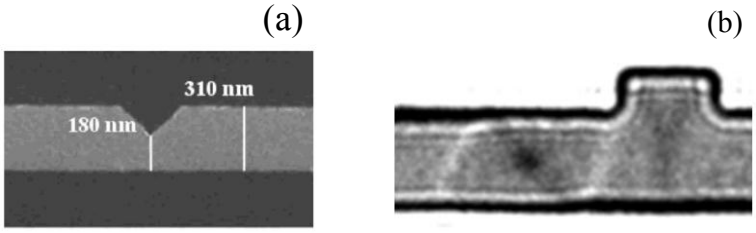

Figure 4-1: (a) A lateral notch with constriction [82]. (b) A lateral notch with protrusion [85].

In this chapter, we have studied an alternative approach to control the notch profile vertically by removing a rectangular shaped portion of the magnetic material along the nanowire (hereafter referred to as nanotrench) as shown in Fig. 4-2. It enables us to utilize the advantage of controlling the vertical etching depth accurately down to a few monolayers with ion milling. We study the field-induced pinning and depinning of DWs, from the nano-trench pinning site, in the permalloy nanowires. Furthermore, we also compare the pinning strength of conventional V-notches.

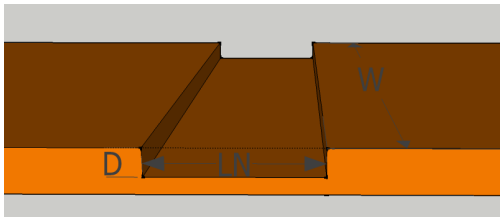

Figure 4-2: Proposed vertical notch, ‘nanotrench’.

4.3 Simulation studies on pinning sites

4.3.1 Nanotrench pinning site

Micromagnetic simulations of the depinning studies are performed using the object oriented micromagnetic framework (OOMMF). Two different dimensions of nanowires are utilized for studying transverse (a width of 100 nm and thickness of 10 nm) and vortex (a width of 200 nm and thickness of 40 nm) DWs for nanotrench. Cell dimensions of 4×4×2 nm^3 and 4×4×5 nm^3 have been used, for the transverse and vortex case, respectively. A saturation magnetization of M_S = 8.6×10^5 A/m, exchange constant of A = 13×10^{-12} J/m, and an anisotropy constant of K = 0 are assumed. The simulations were performed at the quasi-static regime and the Gilbert damping parameter (α) is set to 0.5 to improve the speed of the simulations.

A nanotrench is placed at the center along the nanowire as shown in Fig. 4-3(a). The center of the DWs is located at the right edge of the nanotrench and released to relax for several nanoseconds to form an energetically favorable, stable structure in each simulation to maintain consistency throughout. Examples of a similarly initialized transverse and a vortex DW at the nanotrench are shown in Fig. 4-3(b) and (c), respectively. During the relaxation process, the vortex DW moves outwards of the nanotrench and is stabilized, while the transverse DW moves towards the center of the nanotrench. The position of the nanotrench is highlighted using a dark shade. In both cases, the length of the nanotrench (LN) is 240 nm, while the depth (DN) is 6 and 20 nm, respectively, for transverse and vortex cases.

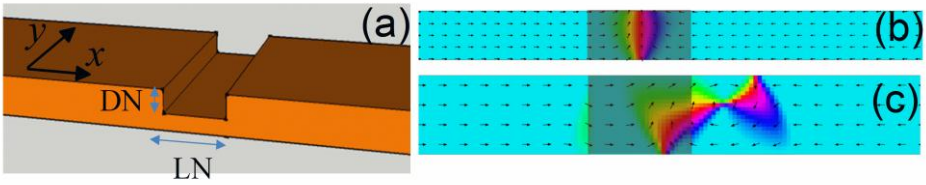

Figure 4-3: (a) Schematics of a nanotrench. Initialized (b) transverse and (c) vortex domain wall at the nanotrenches. The dark shade highlights the area of nanotrench.

For the case of V-notch, the length of the notch (LN) and depth of the notch (DN) are defined as in Fig. 4-4. Two different dimensions of nanowires are used for transverse (a width of 100 nm and thickness of 10 nm) and vortex (a width of 200 nm and thickness of 30 nm) DW configurations. Initialized DW configurations for transverse and vortex cases are shown in Fig. 4-4(b) and (c), respectively.

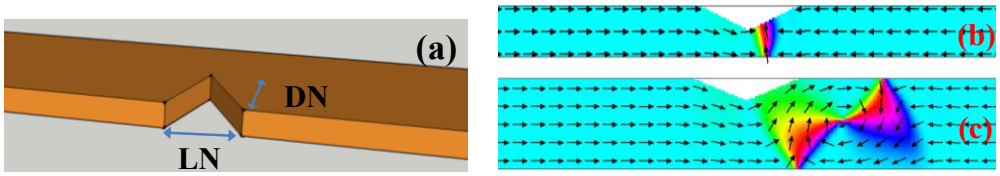

Figure 4-4: (a) Schematics of V-notch. Initialized (b) transverse and (c) vortex domain wall at the V-notches.

4.3.2 Depinning field studies on nanotrench and V-notch

4.3.2.1 Transverse domain walls

The effect of varying the notch dimensions on the pinning and depinning of both types of DWs have been studied. The length (LN) and the depth (DN) of the notches are gradually varied. Magnetic field is applied in the +*x*-direction. The evolution of the DW structure during the depinning process from the right – side of the notch for nanotrench and V-notch is shown in Fig. 4-5(a) and (b), respectively. The DWs expands in the direction of field due to the Zeeman energy before being depinned from the pinning site.

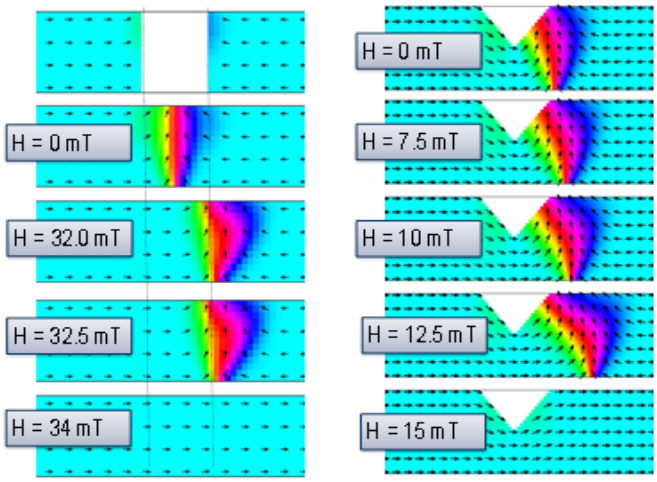

Figure 4-5: Evolution of transverse DWs during the depinning process at a nanotrench (a) and a V-notch (b).

For the case of a transverse wall in a nanotrench, when the DN is increased from 2 to 6 nm, the depinning field strength increases almost linearly as shown in Fig. 4-6(a). This trend remains the same for all the trench lengths (LN) investigated. However, when the length of the notch (LN) is increased from 20 to 240 nm, it is observed that the pinning field increases linearly and subsequently saturates as shown in Fig. 4-6(c). For the case of a 6 nm deep nanotrench, the depinning field saturates at a nanotrench length of 100 nm.

For the case of a transverse wall in V-notch, when the DN is increased from 10 to 50 nm, the depinning field also increases similar to the case of nanotrench as in Fig.4-6(b). However, when LN is increased from 20 to 240 nm for the V-notch as in Fig 4-6(d), the depinning field gradually decreases in contrast to that of nanotrench.

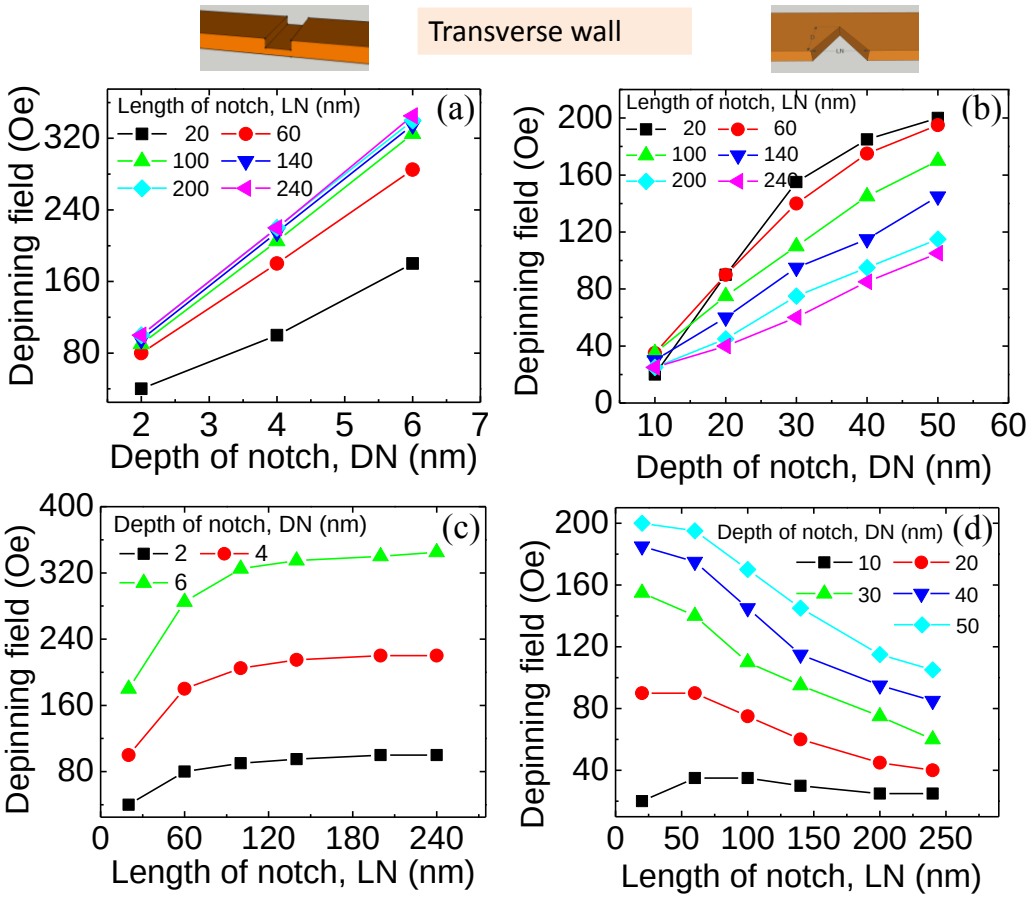

Figure 4-6: Depinning strength of transverse DWs. (a) and (b) show the depinning strength with respect to depth of notches (DN) for nanotrench and V-notch respectively. (c) and (d) show the depinning field dependence for length of notch (LN) for both cases.

4.3.2.2 Vortex domain walls

The evolution of the vortex walls at the pinning site in response to an increase in magnetic field is shown for a nanotrench and V-notch in Fig. 4-7(a) and (b), respectively. In both the cases, similar to the transverse DW case, the DWs expand before being depinned.

The depinning fields, for the case of vortex DWs, in nanotrenches show similar trends to that of the transverse DWs. The depinning field increases with the depth and length of the nanotrench as in Fig. 4-8(a) and (c).

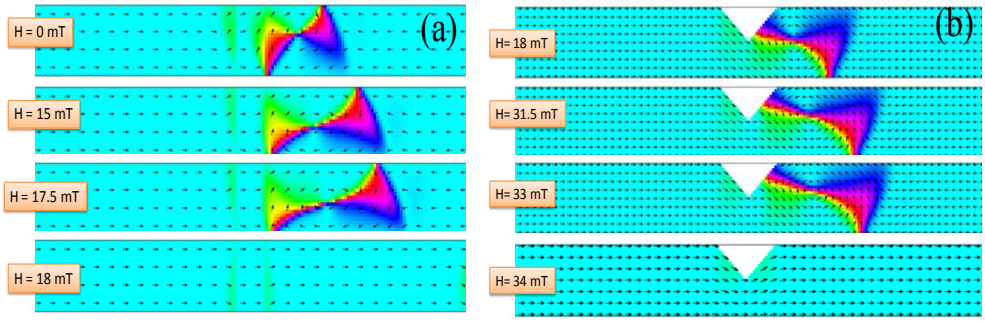

Figure 4-7: Vortex DW evolution during the depinning process at nanotrench (a) and V-notch (b). The DW significantly expands due to the Zeeman energy in the direction of the magnetic field.

However, it is evident that irrespective of the depth of the nanotrenches, the depinning strength profile reaches saturation around a length (LN) of ~ 100 nm for both cases of transverse and vortex DWs. This saturation behavior can be understood by the energy landscape of the pinning sites as discussed in section 4.4.

The depinning behavior of a vortex wall in a V-notch also follows a similar trend described for the transverse case in a V-notch. However, we can see that the depinning strength does not scale linearly as compared to the nanotrench case. Rather, it shows a complex trend.

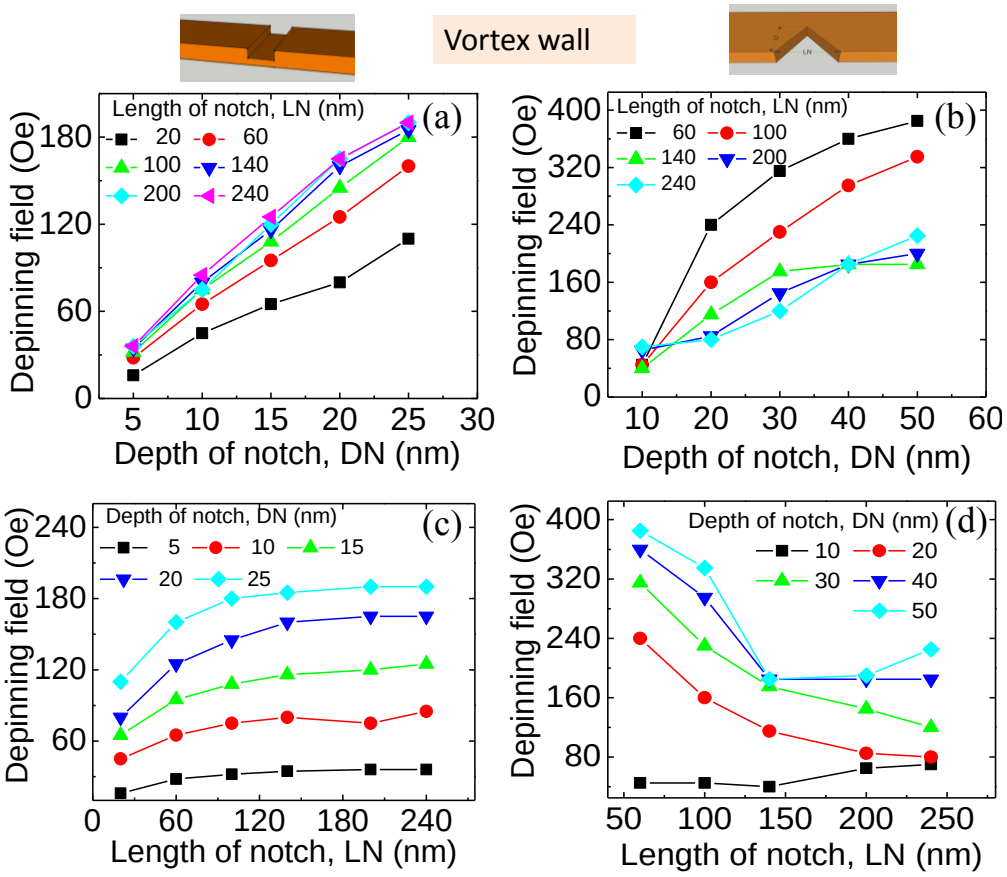

Figure 4-8: Depinning strength of vortex DWs. (a) and (b) show the depinning strength with respect to depth of notches (DN) for nanotrench and V-notch, respectively. (c) and (d) show the depinning field dependence for length of notch (LN) for both cases.

4.4 Energy profile of pinning sites

In order to provide a more quantitative understanding of the depinning behavior, the potential landscape for the DW states are calculated by micromagnetic simulations. The geometrical variations along the nanowire generate an energy landscape that a DW experiences while traversing through the wire. The change in the potential profile reflects the interaction between the spin structure of DW and the pinning site. In order to understand the energy landscape of the notch profiles, energy terms like demagnetization and exchange energy are taken into consideration. A DW is initially placed on the left side, at a distance of 1.5 µm away from the center of the notch. A constant magnetic field is applied along the +*x*-direction to drive the DW towards the right end of the nanowire, thereby, passing through the notches at the center of the nanowire. The absence of the anisotropy energy term makes the energy equation converge to

$$E_{Tot}=E_{Dem}+E_{Ex} \tag{4.1}$$

where E_{Dem} is the demagnetization energy and E_{Ex} is the exchange energy.

A representative simulation setup with a DW initialized at -1.5 µm away from the center of the nanotrench is shown in Fig. 4-9(a). The moving DW in different locations along the nanowire (DW position = -0.35, 0.6 µm) is shown in Fig. 4-9(b) and (c).

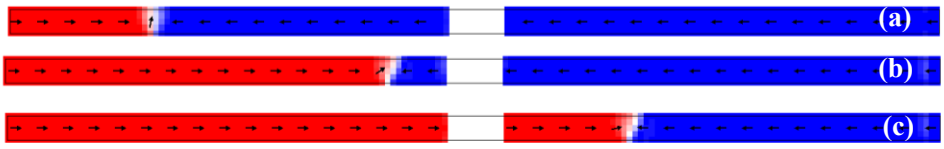

Figure 4-9: (a) A transverse DW is initialized at -1.5 µm away from the center of the nanotrench. (b) and (c) shows the field induced DW motion in different locations along the nanowire (DW position = -0.35, 0.6 µm).

4.4.1 Nanotrench pinning site

4.4.1.1 Transverse DW

The contributions of each energy terms in the system for a transverse DW (LN = 240 nm; DN = 6 nm) in nanotrench is plotted in Fig. 4-10(a) with respect to the DW position. The energy is normalized with respect to the total energy (E_{Tot}). The center of the nanotrench is set to zero on the *x*-axis. The total energy of the system is locally reduced forming a potential well around the center of the nanotrench in case of the transverse DW as shown in Fig. 4-10(a). The demagnetization energy contributes 90%, while the exchange energy is ~ 10% of the of the total energy contribution outside the potential well. The exchange energy increases while entering into the nanotrench area, as a result, providing a resistance to the moving DW, indicated by a small peak at -0.19 µm.

The total energy is plotted in Fig. 4-10(b) for transverse (DN = 6 nm) walls with various lengths (LN = 40 to 240 nm) of nanotrenches in order to achieve a better understanding of the energy landscape at the pinning site. It can be inferred that the shape of the energy profile is almost conserved. Furthermore, the depth of the dip in the energy profile increases with increasing the length of the nanotrench. The curvature as well as the depth of the energy landscape determines the pinning strength. The insets of Fig. 4-10(b) show the drop in the energy profile, ΔE_{Tot} with respect to the energy at 500 nm which follows the same trend as that of the depinning strength discussed in section 4.3.2.1 for the transverse DWs.

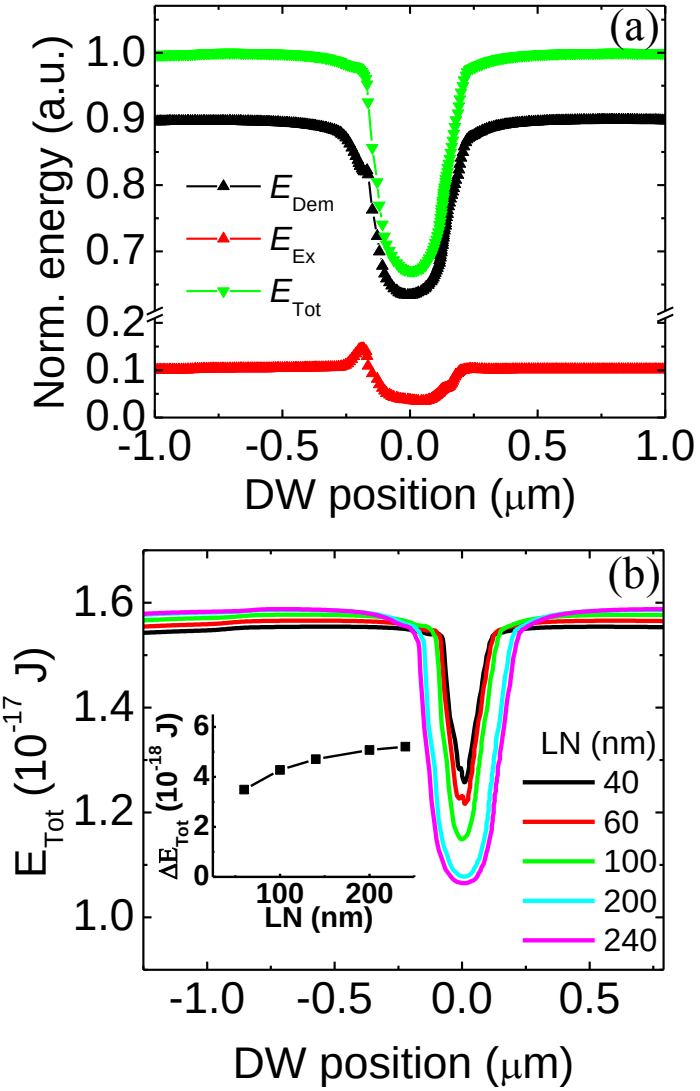

Figure 4-10: (a) Normalized energy profile for separate energy terms with respect to DW position for transverse DW for a nanotrench. (b) Total energy for various lengths of notches with respect to DW position for transverse DW. The inset shows the drop in energy in the potential well with respect to the energy at the position of 500 nm.

4.4.1.2 Vortex DW

The contributions of each energy terms in the system for a vortex DW (LN = 240 nm; DN = 15 nm) in a nanotrench is plotted in Fig. 4-11(a) with respect to the DW position. It should be noted that the interactions generated at the nanotrench edge by a larger vortex DW structure make the energy landscape different from the transverse DW case. The transverse DW pins at the center of the pinning site, whereas the vortex DW is repelled away from

the center of the nanotrench, but pins at either edges of the nanotrench due to a dual-dip energy profile. This phenomenon is also observed in the conventional constriction type notches, where the vortex DW has to realign its spin structure at the expense of increasing energy terms while passing through the notch [82, 89]. However, the contributions from the demagnetization energy and exchange energy remain around 90% and 10%, respectively, which is similar to the transverse DW case as discussed earlier. Similar energy contributions have been reported for pinning sites defined by ion implantation [86].

The total energy is plotted in Fig. 4-11(b) for vortex (DN = 15 nm) walls with various lengths (LN = 40 to 240 nm) of nanotrenches for a better understanding of the energy landscapes. The shape of the energy profile is almost conserved. Furthermore, the depth of the dip in the energy profile increases with increasing the length of the nanotrench similar to the case of the transverse DWs. The insets of Fig. 4-11(b) show the change in the energy profile, ΔE_{Tot} with respect to the energy at 500 nm which follows the same trend as that of the depinning strength discussed in section 4.3.2.2. It can be noted that the drop in energy on both sides of the dip (labeled left and right) shows a very similar behavior for the vortex DW case shown in the inset of Fig. 4-11(b).

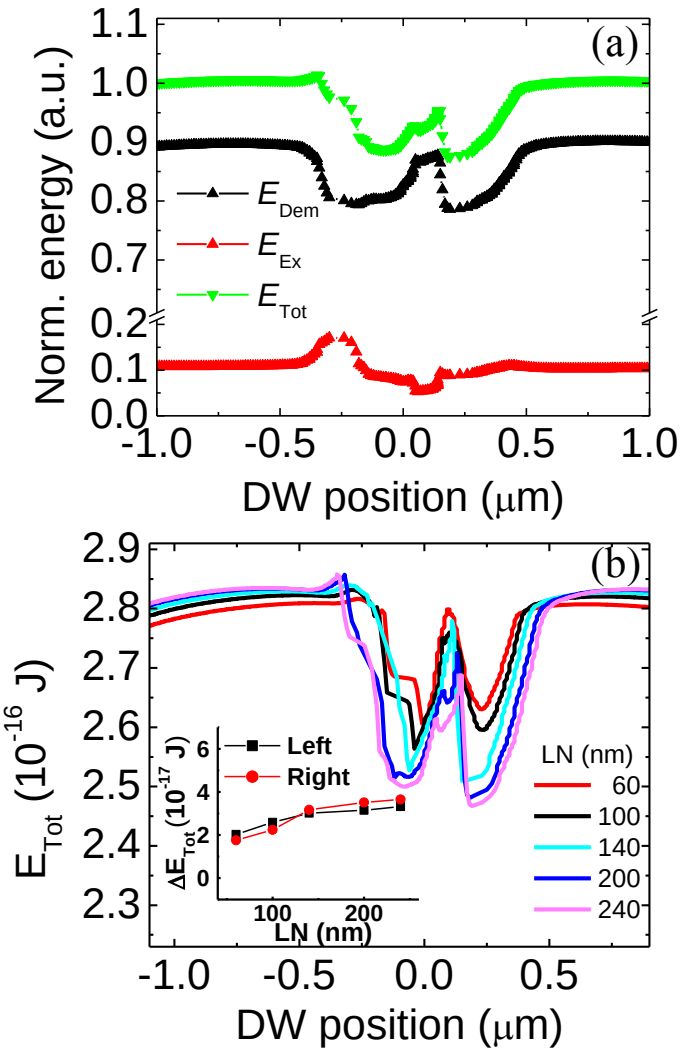

Figure 4-11: (a) Normalized energy profile for separate energy terms with respect to DW position for vortex DW for nanotrench. (b) Total energy for various lengths of notches with respect to DW position for vortex DW. The inset shows the drop in energy in the potential well with respect to position 500 nm.

4.4.2 V-notch pinning site

4.4.2.1 Vortex DW

The contributions of each energy terms in the system for a vortex DW (LN = 240 nm; DN = 50 nm) in a V-notch is plotted in Fig. 4-11(a) with respect to the DW position. A dual dip phenomenon is observed similar to the nanotrench (vortex). However, the energy barrier while the DW moves through the V-notch is higher compared to the nanotrench case. The total energy is plotted with respect to the DW position in Fig. 4-12(b). The dip in

the total energy does not scale with the depinning field, suggesting that, the curvature of the potential profile of the pinning site plays a dominant role in V-notches.

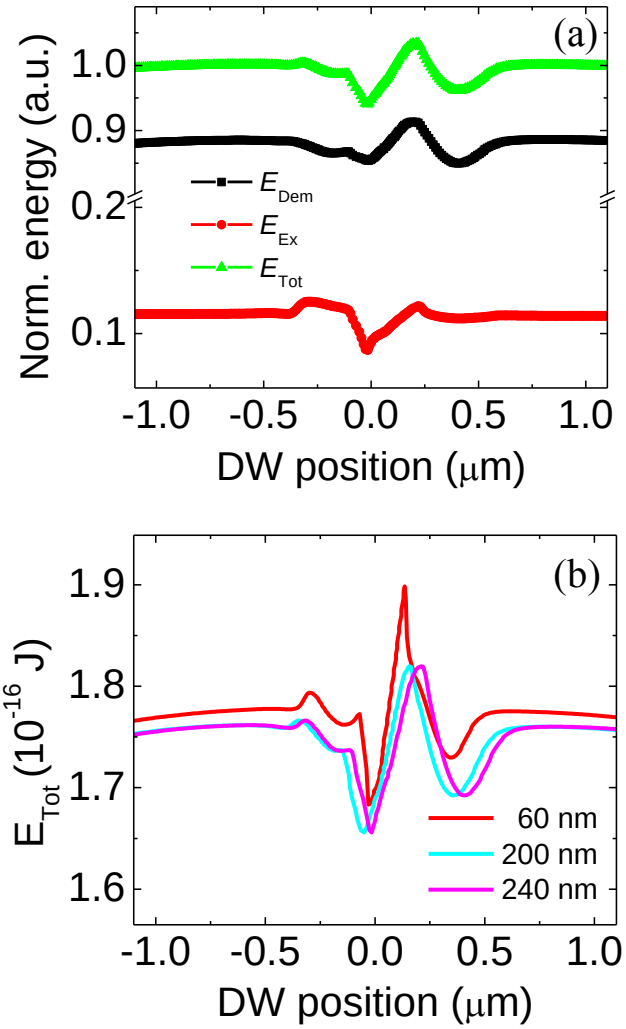

Figure 4-12: (a) Normalized energy profile for separate energy terms with respect to DW position for vortex DW for V-notch. (b) Total energy for various lengths of notches with respect to DW position for vortex DW.

We further analyze the spatial energy landscape along the nanowire without a DW. The magnetization of the nanowire around the V-notch is shown in Fig. 4-13(a) after relaxing the system for several nanoseconds. The magnetization stays parallel along the V-notch due to the demagnetization energy. The total energy of the nanowire along the nanowire position is plotted in Fig. 4-13(b). The curvature of the potential profile is clearly decreases with increasing notch length.

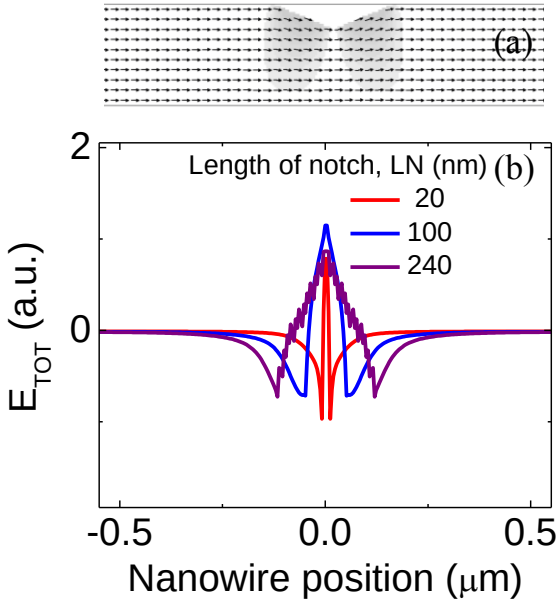

Figure 4-13: (a) Nanowire with a notch after the magnetization relaxing process. (b) Total energy along the nanowire position.

We extend the studies with a vortex wall at the V-notch. Vortex walls are initialized at the right edge of the V-notch for various lengths of notches (LN) as in Fig. 4-14(a). When a vortex DW is present around the notch position, the energy landscape in Fig. 4-14(b) significantly changes as compared to Fig. 4-13(b). The curvature of the potential profile varies with the length of the notch.

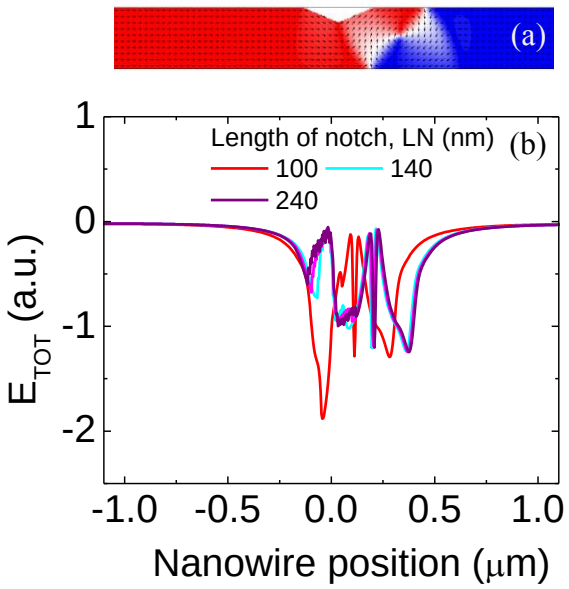

Figure 4-14: (a) A simulated DW at the V-notch (b) Total energy for various lengths of notches with respect to the DW position.

4.5 Experimental studies with nanotrench pinning site

The proposed nanotrench pinning sites are experimentally verified in permalloy nanowires. The following section presents the experimental details and the results obtained.

4.5.1 Device preparation

Thin films with the stack structure of substrate/Ta(3 nm)/NiFe(30 nm)/Ta(3 nm)/Ru(2 nm) are patterned by EBL and by Ar ion milling. The measurement pads are defined by EBL and followed by deposition and a lift-off process. The top 2 nm of the nanowire was partially etched before depositing the measurement pads to provide better ohmic contact between the nanowire and the contact pads. Finally, the nanotrench is defined using an etch mask designed by EBL and then followed by Ar ion milling to remove a portion of the nanowire to form the required vertical nanotrench.

4.5.2 Experimental schematics

Figure 4-15 shows a scanning electron micrograph with the measurement schematics along with the fabricated nanotrench highlighted in red color within the nanowire (nanowire width: ~ 650 nm; length: 12 µm). 10 nm (depth) permalloy is etched out to form the nanotrench with 1 µm length.

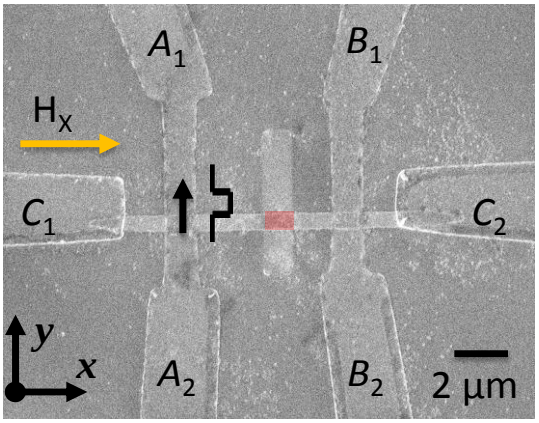

Figure 4-15: SEM micrograph with the measurement schematics. The etched out nanotrench is highlighted in red shade.

4.5.3 Domain wall generation

Anisotropic magnetoresistance (AMR) is a suitable choice for DW detection. It reduces the resistance of the nanowires due to the presence of a DW. The Oersted field generation method is utilized in this experiment to generated DWs which is discussed in detail in section 3.3.4. The following sequence is employed for DW generation and detection. First, a saturation magnetic field, H_{SAT} = 1 kOe, is applied in the +*x*-direction and reduced to zero, and then the saturation resistance, R_{SAT} is measured with a dc current of 30 μA applied across A_1B_1 contacts. Secondly, a short pulse is applied across A_1A_2 contacts to generate a DW by utilizing the Oersted field generation method [90] and simultaneously a constant injection field, H_{INJ} is applied in the –*x*-direction to push the DW to the nanotrench. Then, the resistance (R_I) across A_1B_1 contacts is measured again at zero fields. The difference between two resistance values (= $R_{SAT} - R_I$) is associated with the DW resistance (R_{DW}). Subsequently, 1 kOe is applied along the –x-direction to remove any effects from remanence. The above process is repeated to gain a statistical distribution.

R_{SAT} estimated for the nanowire shown in Fig. 4-15 is ~ 145.80 Ω. R_{DW} is recorded for repeated measurements with varying injection field, H_{INJ}. Figure 4-16 shows R_{DW} for multiple measurements in which the DW injection and detection processes are repeated many times with H_{INJ} = 30 Oe. The negative values are consistent with the presence of a DW in AMR measurements. However, the values change from measurement to measurement, which is in consistent with the reports on different types of DWs and its stochastic behavior [28].

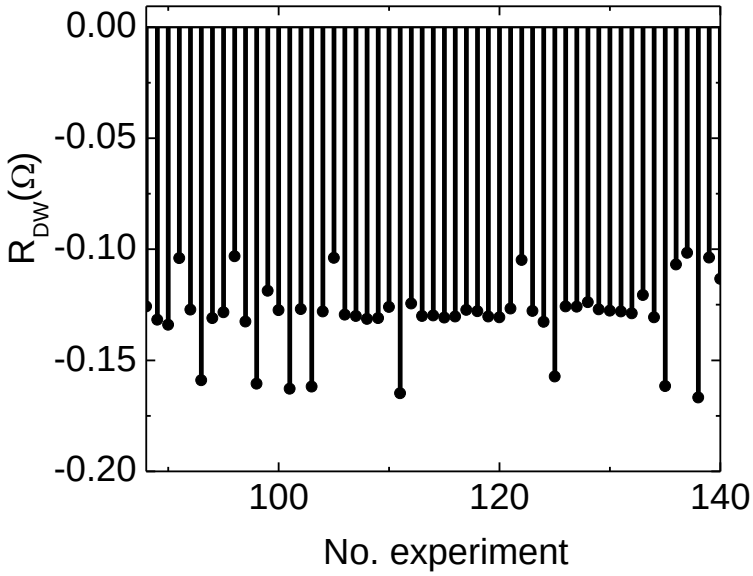

Figure 4-16: Measurements of R_{DW} in a series of experiments in which the wire is first magnetized and a DW is subsequently injected.

The H_{INJ} is varied from 0 to 40 Oe in steps and the DW generation measurements are repeated. The 2D contour plot is presented in Fig. 4-17(a). From the R_{DW} values in the contour plot, it can be observed that there are 4-distinctive areas for R_{DW} values. This is consistent with the previous reports of four different types of DWs existing in permalloy nanowires. The histogram plots shown in Fig. 4-17(b), (c), and (d) are for the H_{INJ} values of 10, 20, and 30 Oe, respectively.

For instance, the three different DW resistances (R_{DW} = -0.16, -0.13, -0.10 Ω) in Fig. 4-17(d) with H_{INJ} = 30 Oe, can be explained by the existence of transverse and vortex DWs with different chirality at the nanotrench. The high occurrence of two types of DWs could come from the anticlockwise and clockwise vortex DWs, while the relatively small occurrence values of -0.10 Ω can be attributed to the transverse DW configurations [28, 91, 92].

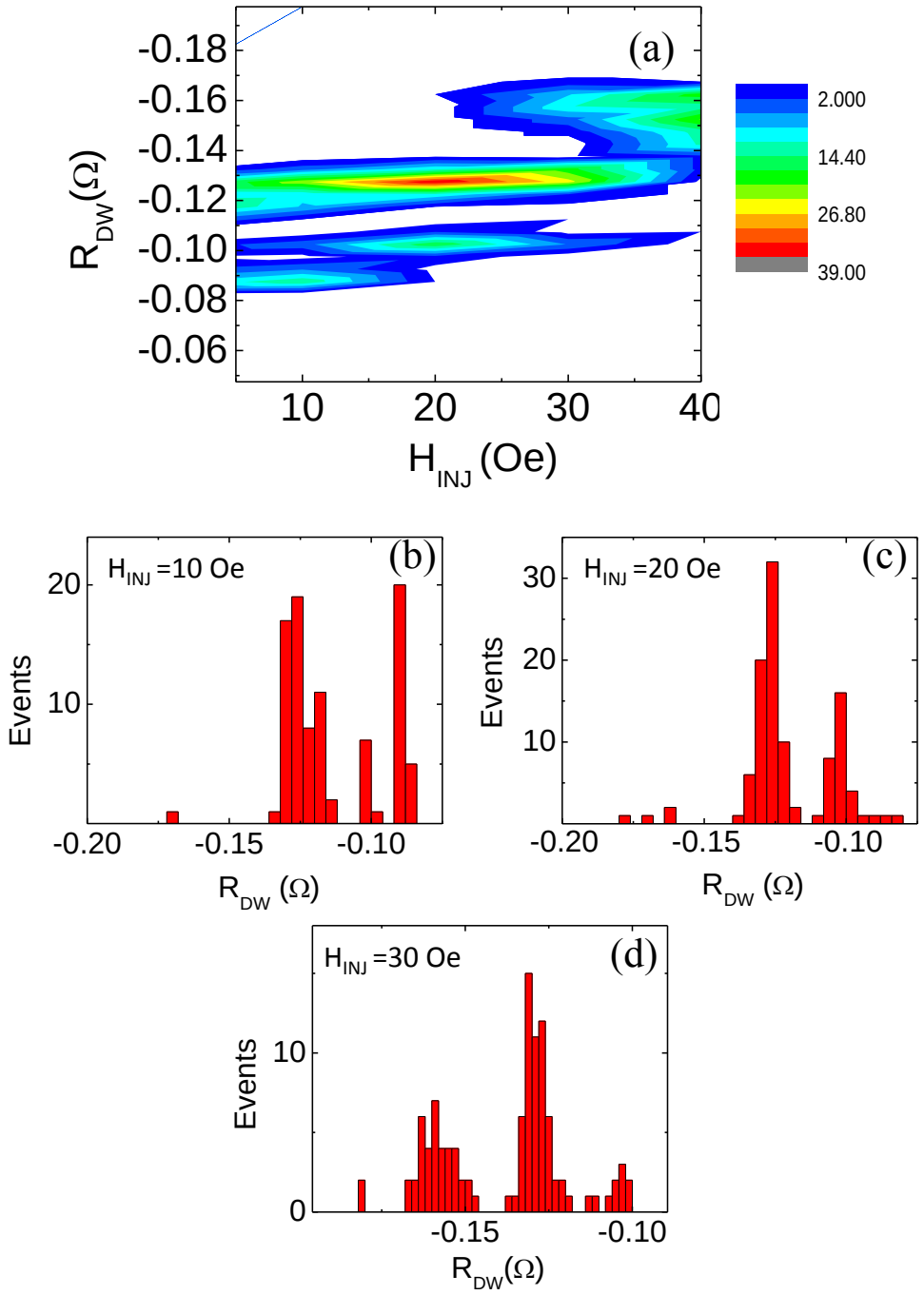

Figure 4-17: (a) Contour plot for DW resistance (R_{DW}) with respect to H_{INJ}. Four different resistance regions are visible. (b), (c), and (d) show the histogram plot for H_{INJ} = 10, 20, and 30 Oe, respectively.

4.5.4 Domain wall depinning

The depinning strength of the pinned DWs at the notch is also investigated. After a DW is pinned at the nanotrench as discussed in the previous section, the magnetic field is increased in steps of 2 Oe in the –x-direction to depin the DW from the notch. A representative depinning profile is shown in Fig. 4-18. The abrupt change in the resistance values at 52 Oe show the field at which the DW is depinned. As shown in Fig. 4-18, when the DW is removed from the nanotrench and moves out of the A_1B_1 portion, the resistance reaches the R_{SAT} value (145.80 Ω).

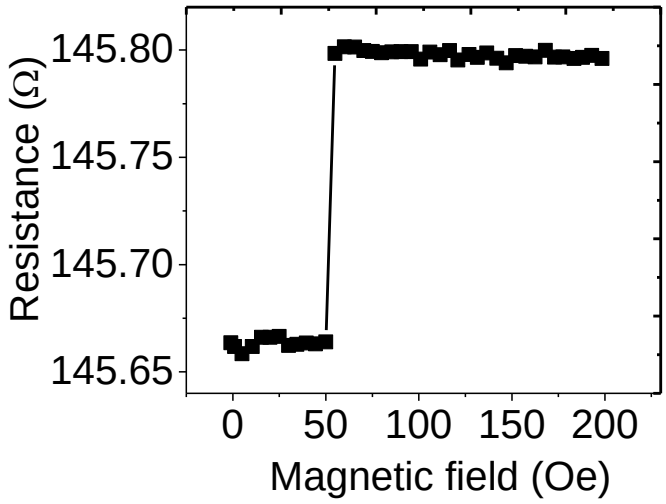

Figure 4-18: Typical DW depinning profile as a function of applied magnetic fields at the nanotrench pinning site. The abrupt change in the resistance values show the depinning field at which the DW is pushed out of the nanowire.

The histogram of depinning fields for the DWs generated at nanotrench pinning site is shown in Fig. 4-19. We can see that the DW depinning is distributed. The depinning strength is dependent on the DW type and chirality. This could be understood by the presence of different DW types generated during the DW generation process and stochastic behavior of the depinning process [74, 93].

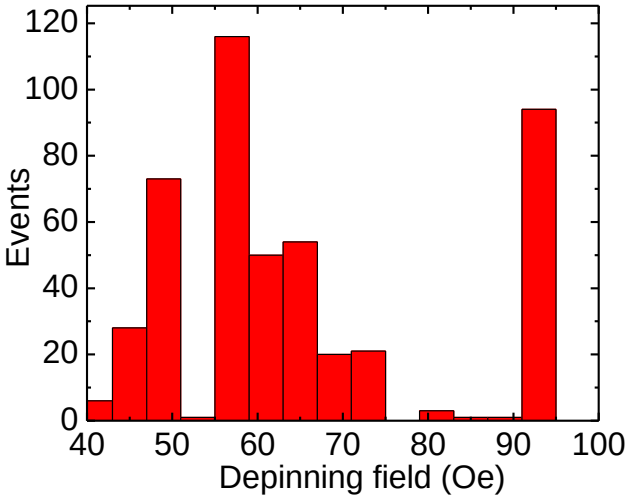

Figure 4-19: Histogram of depinning fields for the DWs generated at nanotrench pinning site.

In order to further understand the correlation of the depinning field with the types of DWs, we scrutinize the depinning results obtained with the DWs generated with H_{INJ} = 30 Oe. Figure 4-20(a) shows the histogram of the DW resistance with 3 different distinct DW configurations as discussed in section 4.5.3. The histogram of the corresponding depinning fields for the generated DWs is shown in Fig. 4-20(b). Histogram plots for $|R_{DW}| > 0.14\ \Omega$, $0.14\ \Omega > |R_{DW}| > 0.10\ \Omega$ and $|R_{DW}| < 0.10\ \Omega$, which represent 3 different DW types, are plotted separately in Fig. 4-20(c), (d), and (e), respectively. We can clearly see a DW type dependent depinning field distribution similar to the reports in V-notches [28].

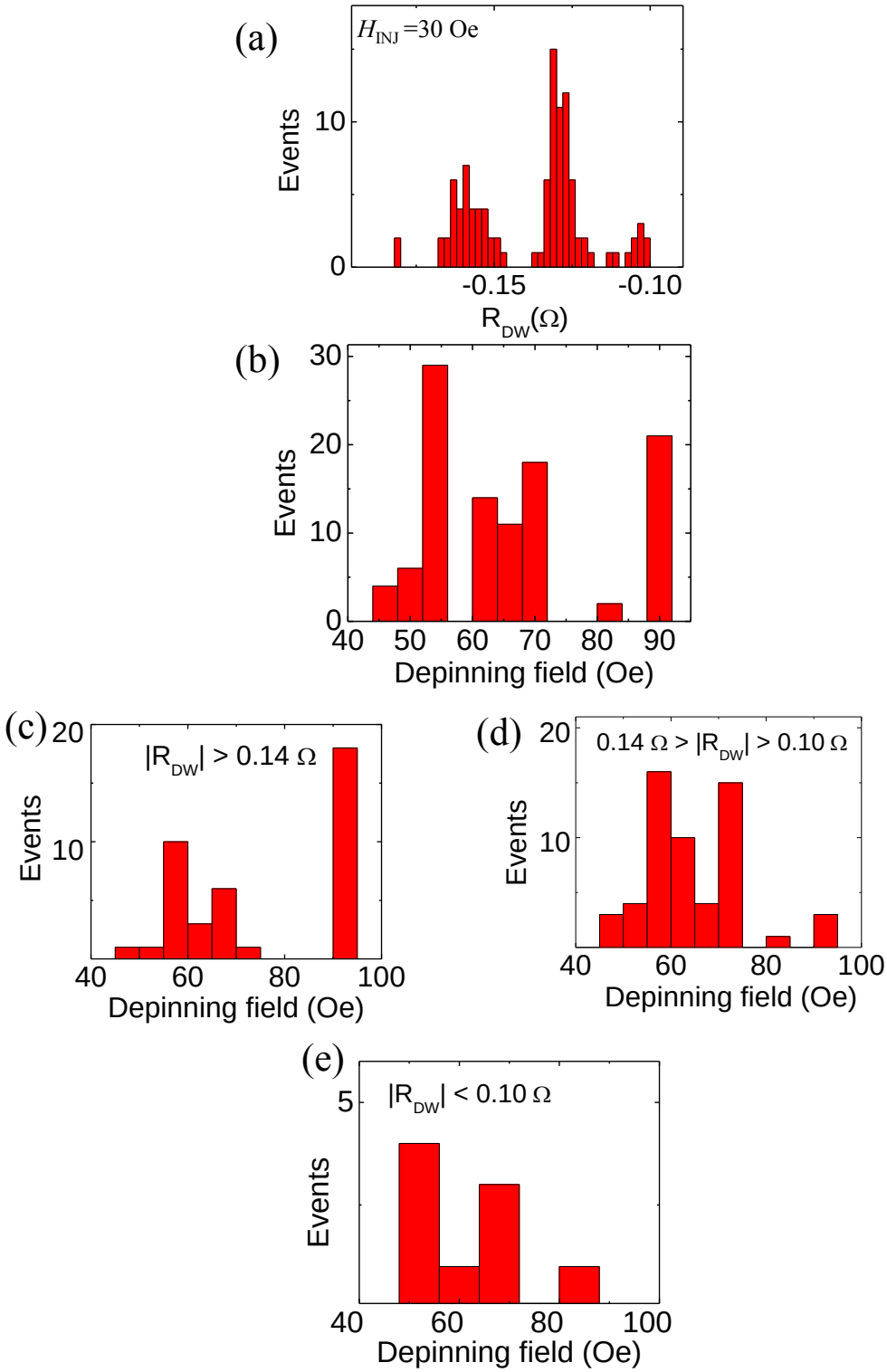

Figure 4-20: (a) Histogram of DW resistance with H_{INJ} = 30 Oe. (b) The histogram of the depinning fields for the DWs generated in (a). Histogram of depinning fields for (c) $|R_{DW}| > 0.14$ Ω, (d) $0.14\ \Omega > |R_{DW}| > 0.10\ \Omega$, and (e) $|R_{DW}| < 0.10$ Ω.

The notches with lateral constriction such as V-notch have been studied in detail in literature. Due to the lateral constriction, the vortex DW undergoes significant change in its spin structure, with changes the type of DW and even its chirality. Therefore, the potential profile of the system becomes complicated. Hayashi *et al.* presented the DW evolution at the V-notch in which the DW goes through changes such as chirality as well thereby changing the potential landscape with an increase in the magnetic field [28]. Bogard *et al.* studied the energy terms of the nanowire with increasing the magnetic field along the nanowire and thereby following the depinning profile of the lateral notch. The authors also show that the depinning strength is correlated with the potential profile [82]. Klaui *et al*. studied the depth dependence of the V-notch as shown in Fig. 4-21 [94]. As the depth of the V-notch increases, the depinning strength also increases showing similar trend as presented in section 4.3.2.

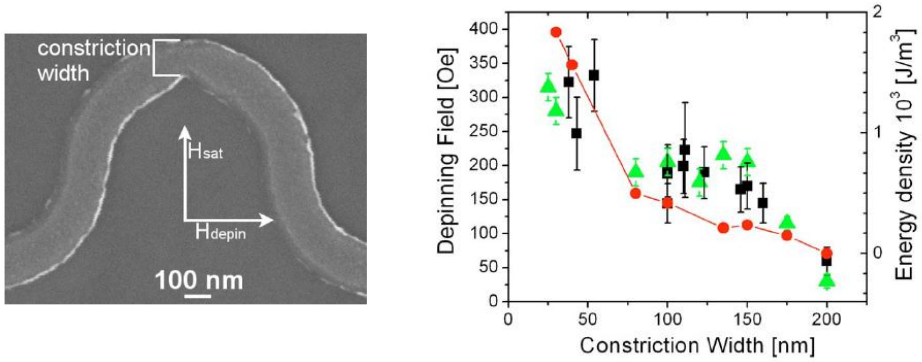

Figure 4-21: (a) SEM image of the nanowire with the constriction. (b) Depinning field with increasing constriction width [94].

4.6 Conclusions

We have successfully demonstrated DW wall pinning in the proposed vertical nanotrench pinning site. The micromagnetic simulations show that the pinning strength can be effectively controlled by the proper selection of nanotrench dimensions. Different shapes of the potential profile are observed for transverse and vortex type DWs. The symmetric nature of the nanotrench

pining site offers less complicated DW evolution at the pinning site compared to conventional the V-notches.

In permalloy nanowires with nanotrench pinning sites, both types of DWs have been experimentally shown to exist. Reliable pinning and depinning behaviors from a vertical nanotrench are observed. Compared to the lateral constrictions, our proposed method has a higher precision in defining the dimensions of the pinning sites in the sub-nanoscale.

Chapter 5 : Thermally assisted domain wall nucleation in perpendicular magnetic trilayers

5.1 Motivation

Effective DW generation and DW control plays an important role in realizing modern DW based devices. A few methodologies are used for DW generation in perpendicular systems. Oersted field assisted DW generation, nucleation pad assisted random DW generation, and anisotropy tailored DW generation are few popular choices.

In this chapter, we study thermally assisted DW generation as an alternative method by introducing Joule heating in a well-defined portion of the nanowire. Our method reduces one lithography step compared to the Oersted field generation process, while offering an efficient and reliable process to selectively generate DWs at predetermined locations with greater control.

5.2 Introduction

DWs in perpendicular magnetic anisotropy (PMA) systems have advantages compared to the in-plane anisotropy systems. In particular, the DWs in PMA systems are narrow, leading to a higher storage density, for example, 4.2 nm in Pt/Co/AlOx system [95], compared to up to a few hundred nanometers in the in-plane (permalloy) system [96]. Recent developments in PMA trilayer systems [97, 98] show their thin layer thicknesses can reduce the operation current for DW based devices. In addition, the critical current density for current induced DW motion can be reduced by tuning the anisotropy through layer stacking [99]. Moreover, the spin Hall effect and the Rashba effect in these systems offer additional ability to manipulate the spin orbit induced torques [14, 95].

Effective DW generation and DW control plays an important role in realizing modern DW based devices. A few methodologies are used for DW generation in perpendicular systems. Figure 5-1(a) shows random DW generation by using a large magnetic reservoir. In this popular approach, the reversal process depends on randomly distributed pinning sites on a large magnetic pad to nucleate DWs in an attached wire [100]. Utilizing the Oersted field is a common approach where a conductor is placed across a magnetic layer, which can be reversed by the Oersted field generated by a current pulse through the conductor [28, 101] as shown in Fig. 5-1(b). Figure 5-1(c) shows the schematics of an anisotropy tailored DW generation method, where a number of magnetic layers is etched out to produce difference in perpendicular anisotropy [78]. The sign of the anisotropy can be locally changed by partially etching the MgO layer in CoFeB/MgO PMA system, and as a consequence, 90° domain walls can be created at the boundary of etched/non-etched region [102]. Other proposed methods include controlling the anisotropy via ion-irradiation [103] where the change/gradient in magnetic anisotropy is used to generate a DW as shown in Fig. 5-1(d). These methods introduce physical damages or locally vary the strength of the pinning sites which are not preferred in some device applications.

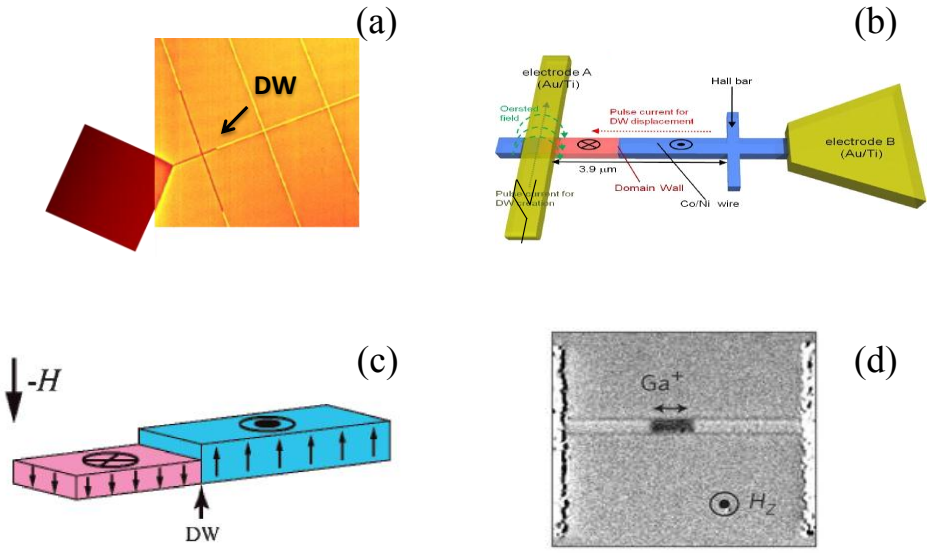

Figure 5-1: Domain wall generation methods in perpendicular anisotropy systems. (a) Nucleation pad assisted [100]. (b) Oersted field [101]. (c) Anisotropy tailored by controlling multilayers [78]. (d) Ion irradiation [103].

Energy assisted magnetization reversal has been studied extensively for applications in magnetoresistive random access memory (MRAM), spin valves, and bit patterned media where external energy is supplied to the system in the form of heat [104-106] or microwaves [107]. Thermal effects could be also utilized to reduce the pinning field [108] and the critical current density in current induced DW motion [109]. A recent study of energy assisted DW generation demonstrates the energy injection in the form of microwaves [110] into the nanowire, hence reducing the nucleation field. Mahdi *et al.* presented spin wave assisted DW motion [83]. Heat assisted magnetic recording (HAMR) is the emerging scheme where the high coercivity of the perpendicular anisotropy magnetic material is reduced by local laser heating [111]. The schematics and the working principle of HAMR are shown in Fig. 5-2(a) and (b).

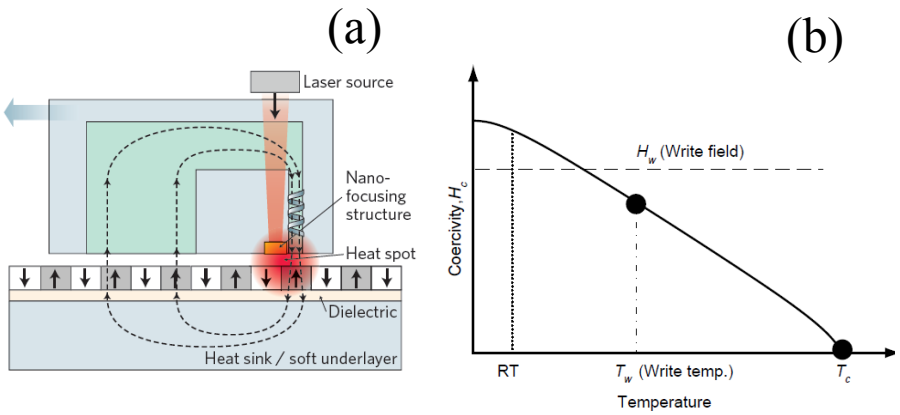

Figure 5-2: (a) Schematics of heat assisted magnetic recording (HAMR) in media. (b) Working principle of HAMR. The coercivity is reduced by increasing the temperature to enable writing in lower field [111].

5.3 Perpendicular anisotropy trilayer system – film preparation

Magnetic trilayers with two stacks are prepared with PMA as shown in Fig. 5-3. An ultrathin layer of ferromagnet is sandwiched between an oxide layer (MgO) and a heavy metal (Pt or Ta). The films are deposited on Si/SiO_2 substrates. The metal layers were deposited by dc magnetron sputtering at 1.5 mTorr Ar and MgO was RF sputtered at 2.2 mTorr Ar.

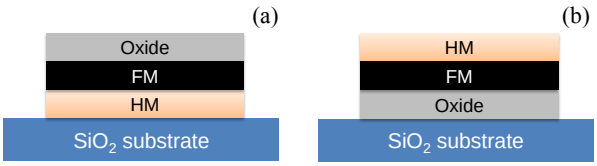

Figure 5-3: Trilayer structures studied for perpendicular anisotropy. (a) Heavy metal is at the bottom. (b) Heavy metal is on top.

The deposition conditions such as the deposition pressure and power are optimized to generate PMA films. Figure 5-4 shows the SQUID measurements for Pt (5 nm)/CoFeB (t nm)/MgO (2nm) in the out-of-plane direction at room temperature. The samples were post annealed at 600 °C for one hour in vacuum conditions. The coercivity of the film increases with increasing the thickness of CoFeB up to 14 Å. A further increase in CoFeB thickness results in the reduction of coercivity as well as the squareness of the loop from which we can infer that the perpendicular anisotropy also decreases. This observation also confirms that the perpendicular anisotropy originates from the interfacial effect.

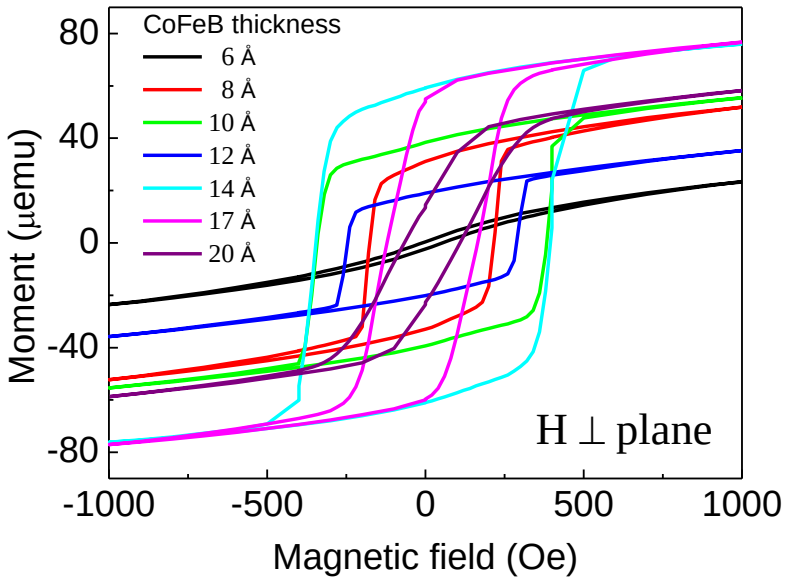

Figure 5-4: SQUID measurements on CoFeB trilayer films in the out-of-plane measurements. The thickness of the ferromagnetic layer is changed from 6 to 20 Å.

Three trilayer films exhibiting strong PMA presented in this chapter are as follows.

Sample A : Pt (2 nm)/$Co_{60}Fe_{20}B_{20}$ (0.8 nm)/MgO (2 nm)
Sample B : MgO (2 nm)/$Co_{60}Fe_{20}B_{20}$ (1.4 nm)/Ta (4 nm)/MgO (4 nm)
Sample C : Pt (2 nm)/$Co_{60}Fe_{20}B_{20}$ (0.8 nm)/MgO (2 nm)/SiO_2 (4 nm)

Sample A and B have effective perpendicular anisotropy fields ($H_{\perp}^{eff}$) of 5.2 kOe and 5.6 kOe, respectively, at 200 K, while sample C shows 9.6 kOe at 300 K. The methodology to extract perpendicular anisotropy from Hall signals is described in section 5.8.

5.4 Experimental schematics

Figure 5-5 shows a SEM image of a device structure with a 600 nm wide nanowire with the same width as the Hall bars. The nanowires are patterned by EBL followed by Ar ion milling. The Hall bars are placed 8 µm apart. Contact electrodes are patterned by photolithography followed by Ta (5 nm)/Cu (105 nm) deposition. The oxide layers are removed by Ar ion milling before depositing the contact pads to improve the electrical conductivity.

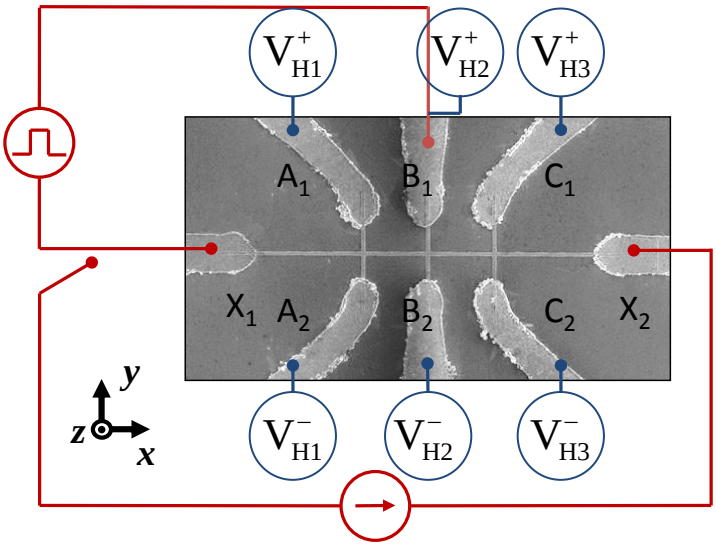

Figure 5-5: SEM micrograph of a 600 nm wide nanowire with 3 Hall bars placed 8 µm apart from each other. A dc-current is used to detect anomalous Hall signals across the three Hall bars.

A dc current source is connected to X_1X_2 and voltmeters are connected across three Hall bars (A_1A_2, B_1B_2, and C_1C_2) as shown in Fig. 5-5 to locally probe the state of magnetization utilizing the anomalous Hall effect (AHE) [100]. The pulse generator is connected across X_1B_1, while the nanovoltmeter is connected to A_1A_2 for current pulsing experiments. The magnetic field is applied in the out-of-plane of the film direction (*z*-direction).

5.5 Thermally assisted domain wall nucleation

Sample A [Pt (2 nm)/$Co_{60}Fe_{20}B_{20}$ (0.8 nm)/MgO (2 nm)] is used for the studies in this section. The measured Hall resistances of VH_1, VH_2, and VH_3 are shown in Fig. 5-6 with an input *dc* current of 10 μA and at 6 K. The nanowire shows a coercivity (H_C) of 2445 Oe. The sharp switching of the Hall signals with the same switching field shows that there is no DW formation or strong pinning during the switching process. In all three Hall bars, the two magnetization states show a change of ~ 8 Ω. The small offset in the Hall resistance arises from the asymmetry of the patterned Hall bars.

The temperature dependency of H_C of the device is shown in Fig. 5-7. The coercivity decreases with increasing temperature. It should be noted that the coercivity of the film and the device after fabrication are significantly different. MgO layer plays a critical part in sustaining perpendicular anisotropy in sample A. During the device making process, it undergoes degradation. Thus, the device loses its coercivity at ~ 200 K. This strong coercivity dependence on temperature can be utilized for the DW generation scheme as described in the next section.

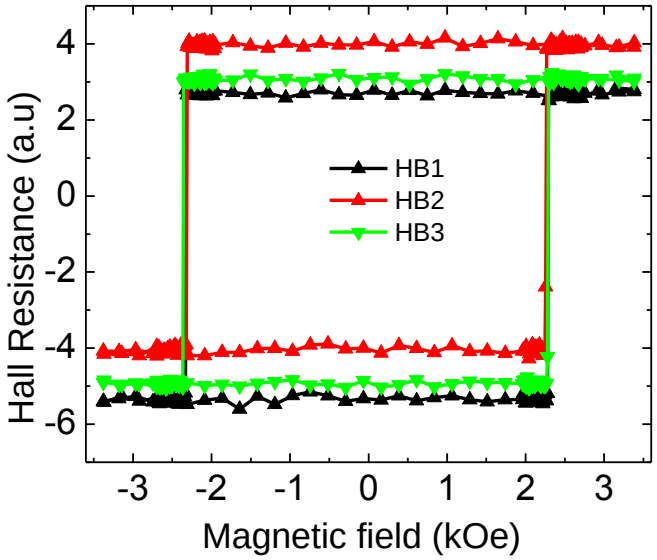

Figure 5-6: Anomalous Hall measurements across Hall bars at 6 K. The abrupt switching shows that all three Hall bars switch at the same field.

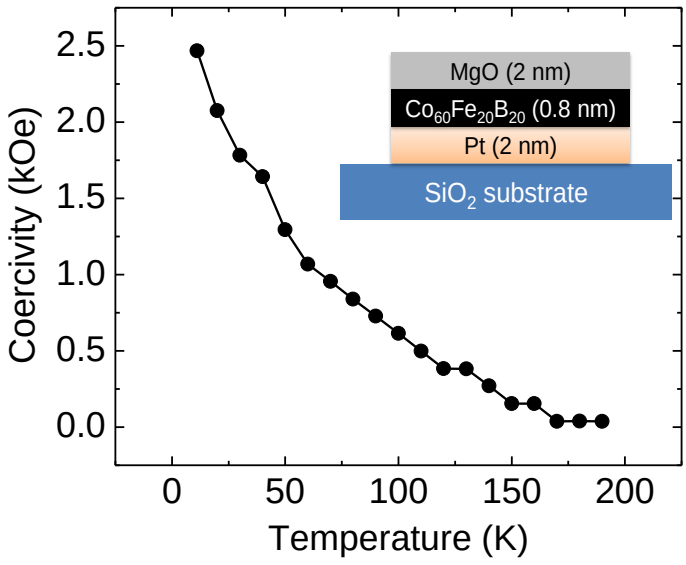

Figure 5-7: Temperature dependence of the coercivity of the nanowire in the out-of-plane direction. Inset shows the trilayer stack.

The concept of the proposed thermally assisted DW generation process is described in Fig. 5-8. An assist field is chosen smaller than the coercivity as indicated as a dashed line in Fig. 5-8(a), and the temperature increases until the coercivity equals the assist field as shown Fig. 5-8(b).

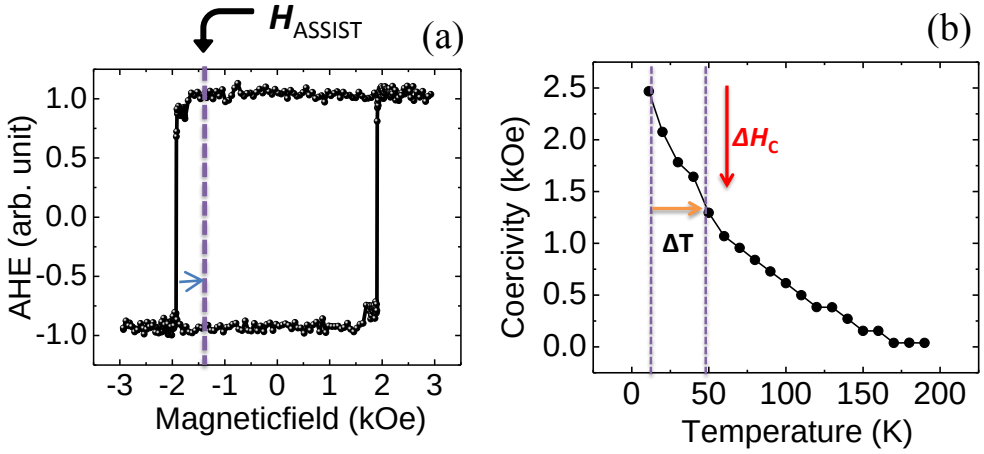

Figure 5-8: Working mechanism of the thermally assisted DW generation. (a) The Hall loop at 6 K. The set assist field is indicated by the dotted lines. (b) The temperature dependency of the coercivity. The arrows show the temperature increase and its corresponding decrease in coercivity.

A schematic diagram to generate thermally assisted DWs is shown in Fig. 5-9(a) and the expected signals are sketched in Fig. 5-9(b). A Keithley 6221/2182A combination is used to apply current pulses and to measure the Hall voltage simultaneously. First, the device is saturated by applying a strong magnetic field H_{SAT} = 4 kOe along the +z-direction and brought back to zero field. The state of magnetization is probed by measuring the Hall signal across 3 Hall bars (VH_1, VH_2, and VH_3). All three readings initially show a high state (magnetization in the +z-direction) as shown in Fig. 5-9(b). Then, a constant assist field H_{ASSIST}, which is smaller than the H_C in order not to switch the magnetization, is applied along the –z-direction. While keeping the field constant at H_{ASSIST}, the current is swept with increasing pulse amplitudes across X_1B_1 to induce local Joule heating in a part of the nanowire highlighted in red in Fig. 5-9(a). Due to an increase of the temperature in this nanowire portion, the local coercivity reduces. When the reduced coercivity equals to the external field, H_{ASSIST}, the magnetization in the heated segment reverses. VH_1 and VH_2 switches to a low state (–z-direction), while VH_3 remains in the high-state (+z-direction), thereby generating a DW at the junction of the second Hall bar. Finally, the device is saturated in the opposite direction by applying –4 kOe in order to remove any remanence and reset to the opposite state.

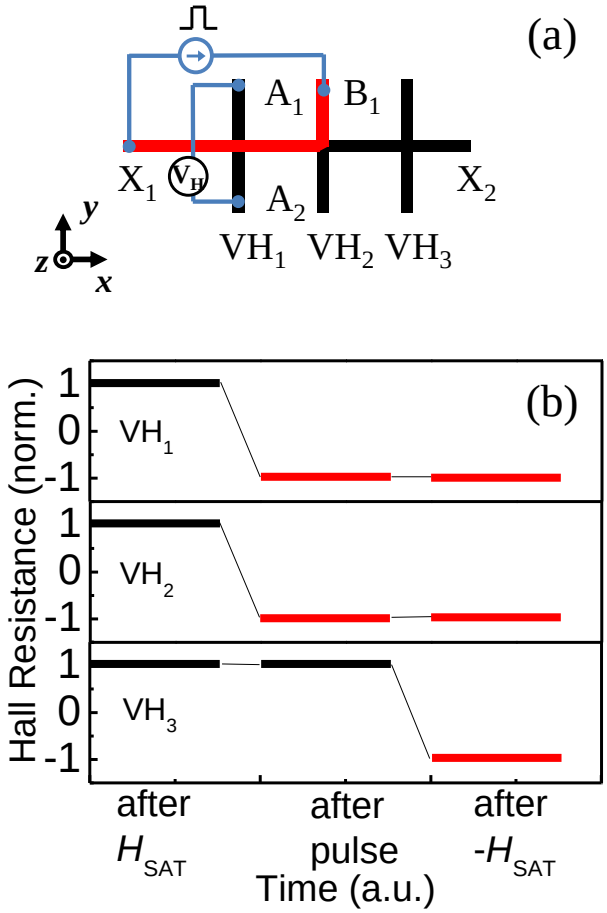

Figure 5-9: (a) Device structure with measurement schematics. The red color highlights the heated portion of the nanowire. (b) Hall bar readings show the state of magnetization. Black and red colors indicate opposite directions of magnetization state.

The distribution of the switching process is studied by repeatedly observing the switching behavior, employing the above described procedure. Current pulses with a pulse width of 1 ms and a pulse interval of 5 s are applied across X_1B_1, while monitoring the Hall resistance VH_1. The pulse interval of 5 s is sufficient to bring the wire temperature back to pre-pulse state. Figure 5-10(a) shows the magnetization switching at 6 K from a low- to high-state with H_{ASSIST} = 2037.5 Oe along the *z*-direction, compared to Fig. 5-10(c), which shows the opposite sequence of a high- to low-state with H_{ASSIST} = -2037.5 Oe at the same temperature. The current amplitude is swept from 200 µA to 350 µA and the switching is clearly represented by the abrupt change of the Hall resistance. In both sequences, we can see a switching

distribution, since it involves a thermal activation process. The histograms of the switching events are presented in Fig. 5-10(b) and 5-10(d), respectively for each sequence. We further analyze the statistical distribution of the switching process. The switching distribution has a mean value (standard deviation) of 296.6 (27.7) μA and 294 (20.8) μA for each sequence, respectively. In our experimental geometry, 296.6 μA corresponds to a current density of 1.765×10^{11} A/m^2. From the switching experiments, we can assume that the coercivity of the device should be reduced from 2445 (H_C) to 2037.5 Oe (H_{ASSIST}) by Joule heating. The corresponding effective temperature increase required to reduce the coercivity is found to be ~ 11 K from Fig. 5-7. The cumulative probability of switching is also shown in Fig. 5-10(b) and 5-10(d), respectively for each case. Above a certain amplitude of current pulse, the probability reaches to 100%.

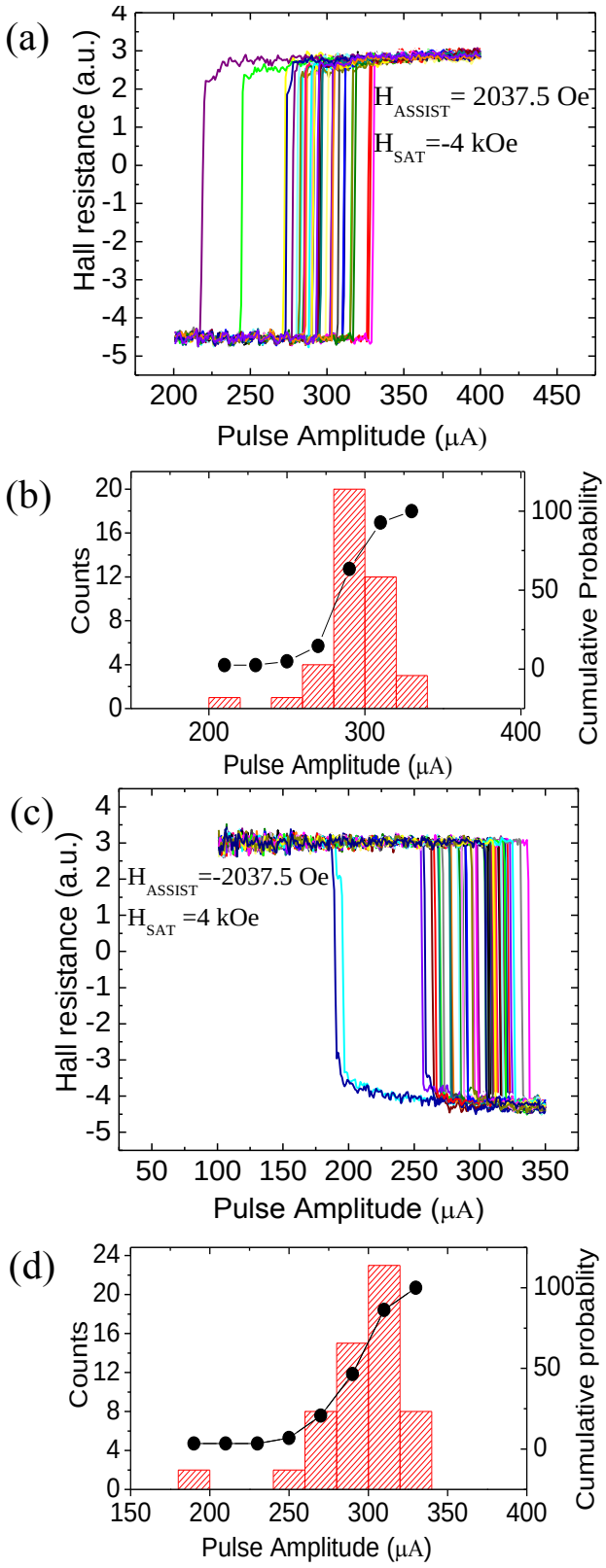

Figure 5-10: (a) AHE measurements across VH_1 for the pulse with 1 ms pulse width applied across X_1B_1 for a positive assist field. (b) Histogram and cumulative probability of the switching processes positive assist field. (c) and (d) shows the respective AHE measurements and the histogram with cumulative probability for a negative assist field.

5.5.1 Effect of assist field

We have further studied the DW generation process with varying H_{ASSIST}. While decreasing H_{ASSIST}, the required switching amplitude increases as shown in Fig. 5-11. This shows that we need to apply more energy to the nanowire in order to compensate the low value of H_{ASSIST}. In order to show that the heat assisted reversal process is dominated by Joule heating, we examine the effect of positive and negative currents on the switching process. The switching distribution is almost the same for both cases as seen in Fig. 5-11, since Joule heating does not depend on the current polarity.

These results clearly show that the required pulse amplitude can be controlled for DW generation with a proper selection of the assist field.

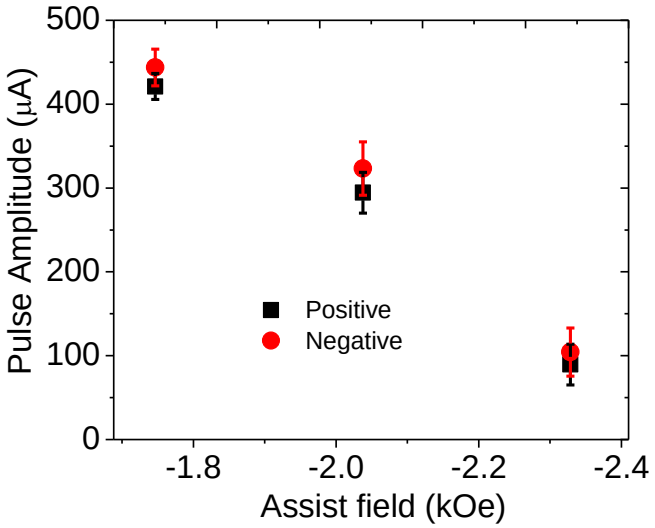

Figure 5-11: Switching pulse amplitude with 1 ms pulse width for various assist fields for positive and negative current polarities.

5.5.2 Effect of pulse width on current density

The switching current amplitude for the case of 50 μs pulse width is shown in Fig. 5-12 and the respective current density is plotted on the right *y*-axis. The required current density increases, when the current pulse width changes from 1 ms to 50 μs. It is clear that with a proper selection of the assist field and the pulse width, we can effectively control the DW generation process.

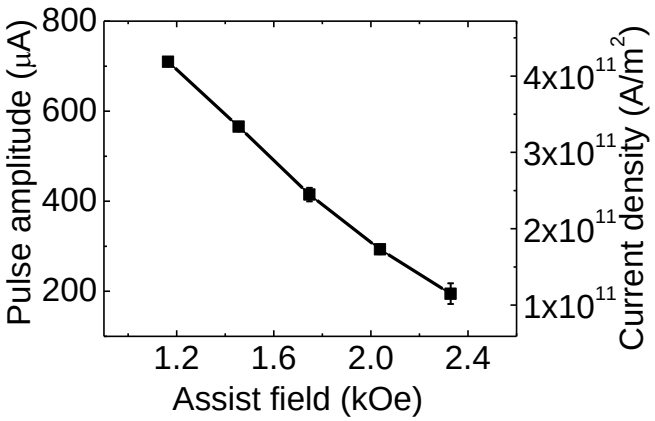

Figure 5-12: Switching pulse amplitude and the respective current density for 50 μs pulse width.

5.5.3 Domain wall nucleation in sample B

We have extended our studies to another trilayer system where magnetic material is sandwiched between MgO and Ta (sample B: MgO (2 nm)/$Co_{60}Fe_{20}B_{20}$ (1.4 nm)/Ta (4 nm)/MgO (4 nm)) to verify the applicability of the proposed method. Similar device geometry and measurement methodology are utilized as discussed for sample A. The Hall resistance of the nanowire is shown in the inset of Fig. 5-13 at 6 K. The two magnetization states show a change of ~ 29 Ω across the Hall bar due to the fact that the high resistive Ta layer gives rise to a higher Hall resistance as compared to Pt in sample A. The coercivity dependence on temperature of the nanowire is plotted in Fig. 5-13.

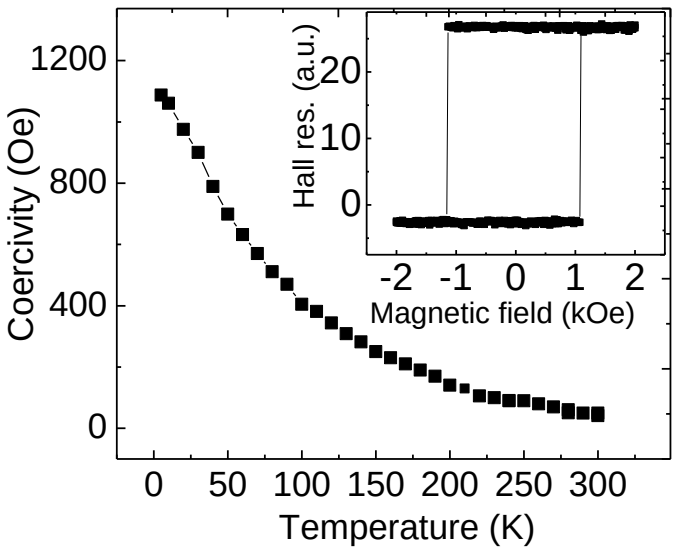

Figure 5-13: The temperature dependence of coercivity for sample B. The inset shows the Hall loop for sample B at 6 K.

The required switching current amplitude for DW generation with varying H_{ASSIST} is shown in Fig. 5-14 which is similar to the case of sample A. In this experiment, a pulse width of 1 ms with a pulse interval of 5 s is used for the experiments same as the case of sample A.

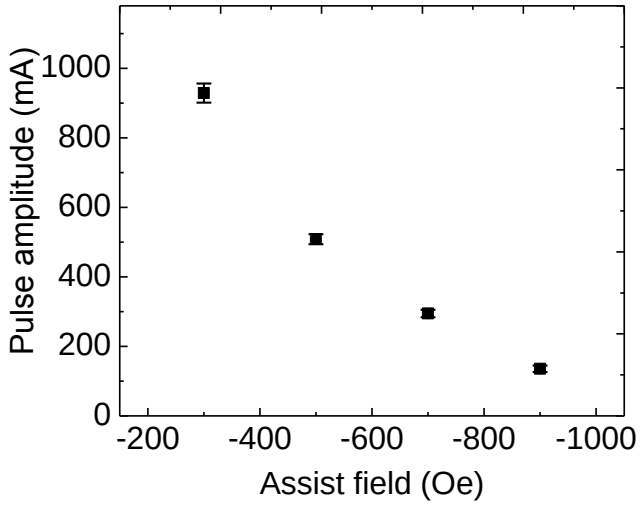

Figure 5-14: Switching pulse amplitude with 1 ms pulse width for various assist fields.

5.6 Thermal analysis on the switching process

In order to further understand the thermal switching process, we have studied the DW generation process with respect to the pulse width in sample C [Pt (2 nm)/$Co_{60}Fe_{20}B_{20}$ (0.8 nm)/MgO (2 nm)/SiO_2 (4 nm)]. The layer stack structure is engineered to have a coercivity at room temperature with the addition of a capping material (4 nm SiO_2). This capping material protects the quality of the top MgO (2 nm) layer and thus prevents the quality of the film from degradation.

The temperature versus coercive field in Fig. 5-15 shows that the coercivity of the sample C increases from 40 to 205 Oe, as the device is cooled from 300 to 200 K.

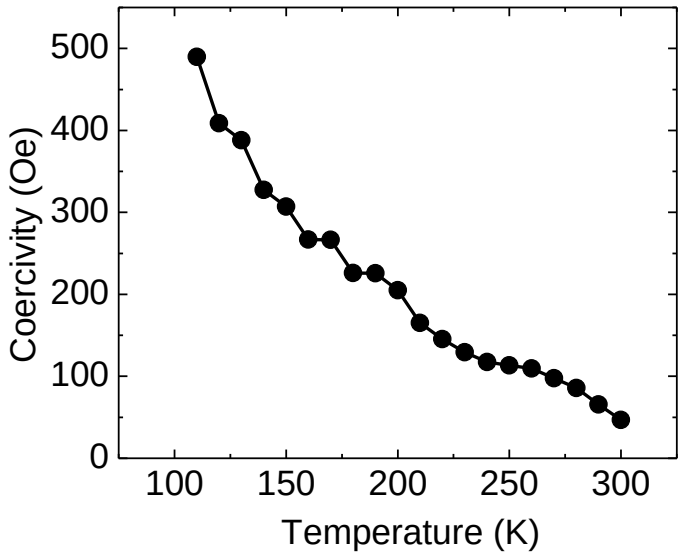

Figure 5-15: The temperature dependence of coercivity for sample C.

The switching amplitude is determined for every pulse width, ranging from 100 μs to 12 ms for a constant assist field of 25, 50, and 100 Oe at 200 K, respectively. A shorter pulse width requires a higher switching current density, while a longer pulse requires a lower switching current density. A higher H_{ASSIST} on the other hand reduces the required switching current density and thus the required temperature change.

We have analyzed the pulse width dependence using Sharrock's equation [112] which is given by

$$H_c = H_0\left\{1-\left[(1/\beta)\ln(At)\right]^n\right\} \tag{5.1}$$

where H_C is the coercivity, t is the hold time, $\beta\left(=\frac{K_U V}{K_B T}\right)$ is the thermal stability factor, $A = f_0/\ln 2$, H_0 is the intrinsic coercivity, and f_0 is the attempt frequency. In these experiments, the switching field is fixed by the external assist field ($H_C = H_{ASSIST}$). The Joule heating is effective when the applied pulse is on, therefore, the hold time can be equated with the pulse width. An increase of temperature due to the effect of Joule heating in a nanowire is given by $\Delta T \propto J^2$, where J is the current density [113]. By rearranging the equation and incorporating the Joule heating effect, the formula becomes

$$t = \frac{1}{A}\exp\left\{\left(1-\frac{H_C}{H_0}\right)^{1/n}\cdot\frac{K_U V}{K_B T}\cdot\frac{1}{\left(1+\frac{\alpha}{T}\cdot J^2\right)}\right\} \tag{5.2}$$

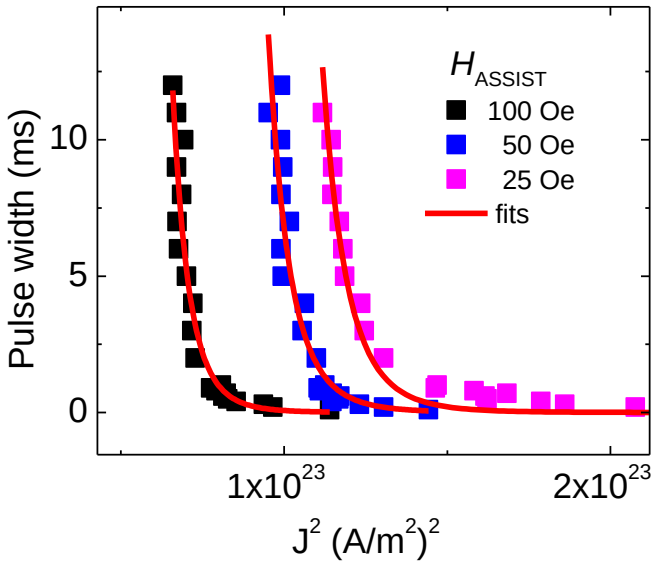

Figure 5-16: Experimental data for J^2 versus the pulse width with fits.

Fits of this equation with the experimental results are shown in Fig. 5-16. For H_{ASSIST} = 100 and 50 Oe with the constants n = 3/2, $f_0 = 10^{10}$ Hz

which are common for the perpendicular magnetic anisotropy, we obtain β = 103.68 and H_0 = 195.32. When we solve the equations for the values of H_{ASSIST} = 100 and 25 Oe, we obtain β = 105.6 and H_0 = 190.36. β has been reported to be 30 – 50 in a similar system [114]. Since K_U increases with decreasing temperature in CoFeB/MgO systems [115], β increases in our case measured at 200 K.

5.7 Domain wall depinning from the Hall-cross pinning sites

To examine the applicability of this method over a temperature range including room temperature, we have studied the DW depinning strength in sample C. The DWs are generated at different temperatures by the proposed heat assisted method with an assist field of 12 Oe as plotted in Fig. 5-17(a). Figure 5-17(b) shows a DW depinning process at 260 K across VH_2. When the DW leaves the Hall bar, a clear switching is observed in the Hall signals.

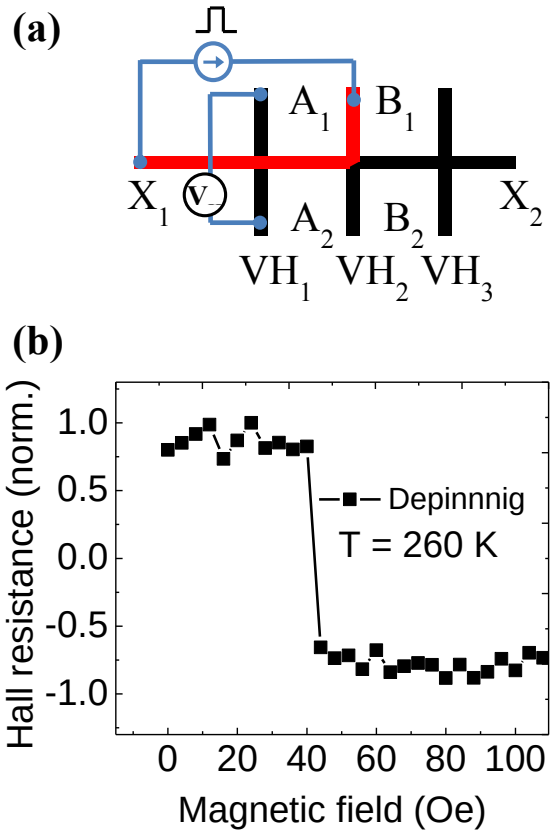

Figure 5-17: (a) Schematics of a generated DW. (b) A typical Hall resistance response of a DW depinning process at 260 K across VH_2.

The depinning field depends on the strength of the local pinning site as well as the coercivity of the material. The depinning field versus temperature for the range of 260 to 300 K is shown in Fig. 5-18 and the coercive field of the nanowire at respective temperatures is plotted as well on the right *y*-axis. We can observe that the depinning field is always lower than the coercivity of the nanowire.

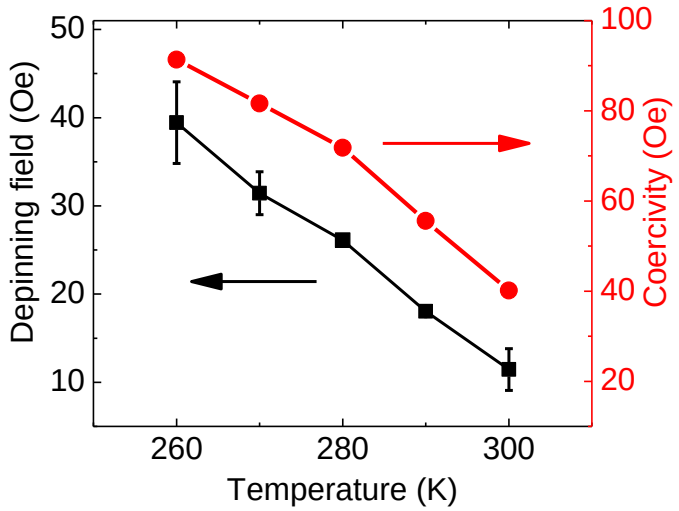

Figure 5-18: Strength of depinning fields and respective coercive fields at different temperatures.

5.8 Determination of the effective perpendicular anisotropy field

The effective perpendicular anisotropy $H_{\perp}^{eff}$ was determined by the following method [42] in sample C [Pt (2 nm)/$Co_{60}Fe_{20}B_{20}$ (0.8 nm)/MgO (2 nm)/SiO_2 (4 nm)]. Saturation magnetization fields are determined by applying in-plane magnetic fields, $H_{\text{in-plane}}$, that is the hard axis fields. Figure 5-19(a) shows a normalized anomalous Hall resistance as a function of in-plane magnetic fields. At $H_{\text{in-plane}} = 0$, the $R_{\text{Hall}} = +1$ and the magnetization decreases as the field increases. This indicates that the magnetization is tilted from the perpendicular direction to the in-plane direction. The normalized in-plane component of the magnetization is determined from normalized R_{Hall} as shown in Fig. 5-19(b). The crossing point of two intersection lines gives $H_{\perp}^{eff} = 9.6$ kOe.

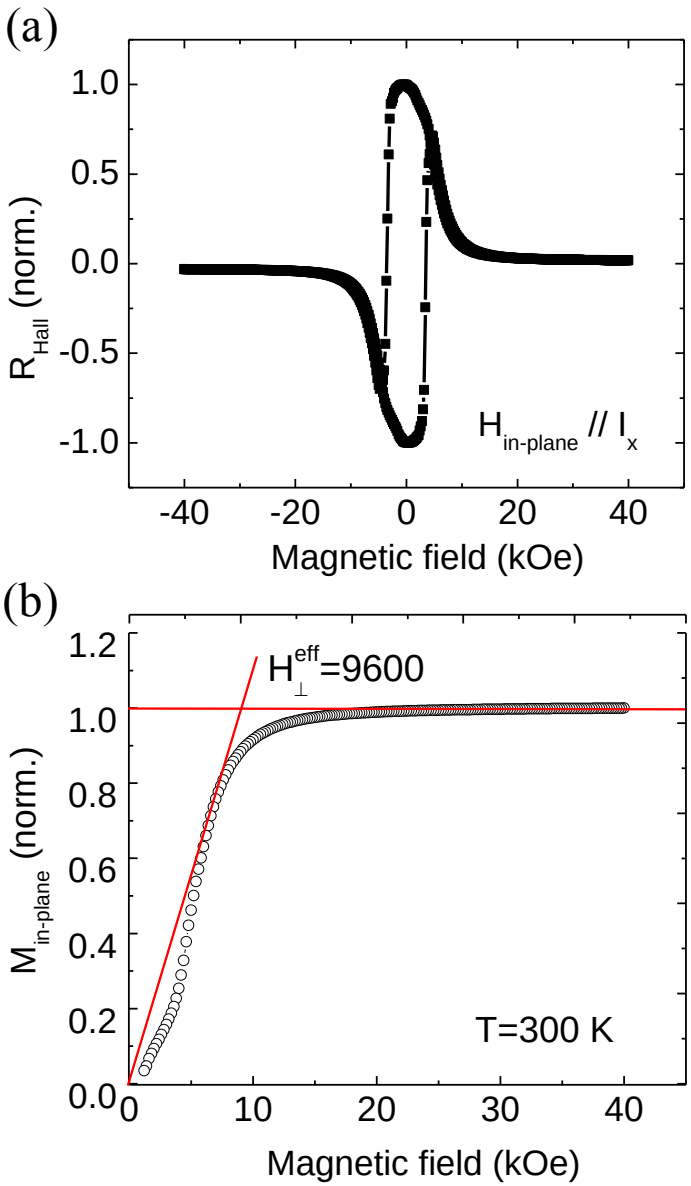

Figure 5-19: (a) In-plane magnetic field $H_{\text{in-plane}}$ dependence of the normalized Hall resistance in sample A. (b) The normalized in-plane component of the magnetization is determined from normalized R_{Hall}.

5.9 Conclusions

We have studied thermally assisted DW generation in perpendicular nanowires as an alternative approach to generate magnetic DWs. The required current density to generate DWs can be effectively controlled by the proper selection of the pulse width and the constant assist field, which is applied during the current pulse. We can selectively generate a DW at a predefined location in PMA nanowires with great reproducibility, which is challenging with tranditional procedures based on random nucleation sites. The proposed method can be extended to generate any desired number of DWs in a single nanowire with relative ease compared to the Oersted field generation method.

Chapter 6 : Magnetocapacitance in ferromagnetic nanowires

6.1 Motivation

Various techniques are used for detecting magnetization reversal. Electrical measurements are superior among them due to its direct industrial applications. Capacitance measurements are widely recognized for characterization in microelectronics. However, it is not explored for magnetization reversal applications in ferromagnetic nanowires.

In this chapter, we study magnetocapacitance in ferromagnetic nanowires with in-plane and out-of-plane anisotropy, and propose magnetocapacitance as a tool for probing magnetic reversal. Our demonstration of magnetocapacitance will be useful for the characterization of the magnetic DW devices.

6.2 Introduction

Optical methods such as magneto optical Kerr effect (MOKE) [15] and magnetic soft x-ray microscopy [74] are often used for the study of DW dynamics. Magnetic force microscopy (MFM) is a probe based technique for imaging DW configurations [7]. Scanning electron microscopy with polarization analysis (SEMPA) is an electron based techniques for probing the surface magnetic microstructure of DWs [116]. While each technique has its own advantages, electrical transport measurements are preferred due to their higher temporal and spatial resolutions, leading to direct device applications. Especially, anisotropic magnetoresistance (AMR), giant magnetoresistance (GMR), and tunneling magnetoresistance (TMR) have been extensively utilized to detect magnetic DWs [28, 35]. For example, AMR is widely used in Ni enriched alloys for the detection of the magnetic DW dynamical properties including the DW velocity, depinning current, and Walker-breakdown field

[28]. Anomalous Hall effect (AHE) is another widely used electrical technique with an out-of-plane magnetic anisotropy, where the DW width is very small [11].

Probe of capacitance provides another method of characterizing the materials and devices. For example, magnetocapacitance (MC) is a phenomenon widely studied in multiferroic materials where the capacitive variation of the multiferroic material in response to external magnetic fields is studied. The magnetic field affects the magnetic ordering and due to the inherent coupling between the ferroelectric and ferromagnetic orders in the multiferroic system, the magnetic signal is reflected in the MC [117]. Spin capacitance occurs due to the accumulation of spin polarized charges at the interface of metals and oxides [118]. In magnetic tunnel junctions (MTJs) [119], the effective interfacial capacitance is due to spin and charge accumulation, and interactions between ions at the interface. The capacitance data also reflect the quality of the interfaces and tunnel barriers in MTJs [120-122].

In this chapter, we study MC in ferromagnetic nanowires such as $Ni_{19}Fe_{81}$ and Co/Pd, and propose MC as a tool for probing magnetic reversal in DW devices. Our demonstration of frequency dependent ac-impedance measurements will be useful for the characterization of the magnetic DW devices.

6.3 Experimental details

For the in-plane magnetic anisotropy, thin films with the structure of Ta (5 nm)/$Ni_{81}Fe_{19}$ (30 nm)/Ta (5 nm) were deposited on Si/SiO_2 substrates by dc-magnetron sputtering with a base pressure of 1×10^{-9} Torr. Semicircular magnetic nanowires with widths of 200 – 900 nm and a radius of 50 μm were defined by electron beam lithography and subsequent argon ion milling. Contact pads were defined by a second EBL step followed by the deposition of Ta (3 nm)/Cu (110 nm) and lift-off process. A top view scanning electron microscopy (SEM) image is shown in Fig. 6-1. In order to nucleate a DW, a bias magnetic field of 750 Oe was initially applied along the *y*–direction and subsequently reduced to zero.

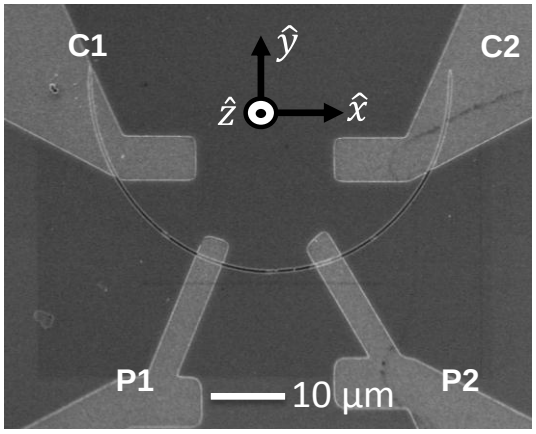

Figure 6-1: SEM micrograph of an 800 nm wide nanowire with electrical leads.

Figure 6-2 shows a vortex type DW imaged by MFM formed at the center of the semi-circular nanowire. Impedance measurements were performed by using an Agilent E4980A precision LCR meter. Standard open and short corrections were performed for calibration to compensate the effect of stray capacitance and inductance from the measurement probes and the coaxial wires.

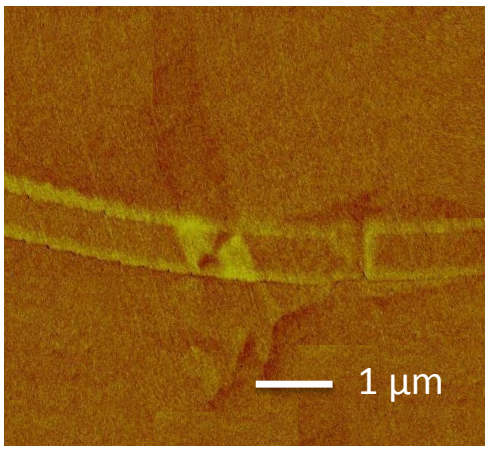

Figure 6-2: MFM image of a vortex domain wall formed at the center of the semi-circular nanowire.

6.4 Magnetocapacitance in permalloy nanowires

The magnetic field was swept along the *y*–direction during the measurements and ac-impedance measurements were performed for excitation amplitude of 0.125 V and frequency of 500 kHz. The voltage was applied

across the C_1C_2 ports and measurements were performed across the P_1P_2 ports as indicated in Fig. 6-1.

Figure 6-3(a) shows the resistance versus magnetic field (R-H) measurements for a nanowire with a width of 800 nm. This is a typical AMR behavior [123], which depends on the angle between the local direction of current and the magnetization. When the saturation magnetic field is applied along the *y*–direction, the current is perpendicular to the magnetization. When the external magnetic field decreases from the positive saturation field, the magnetization aligns along the nanowire due to its shape anisotropy leading to the formation of a DW in the center of the nanowire. When the external magnetic field switches to negative polarity and gradually increases to overcome the shape anisotropy, the DW is destroyed, and is seen as the kink points in the curve.

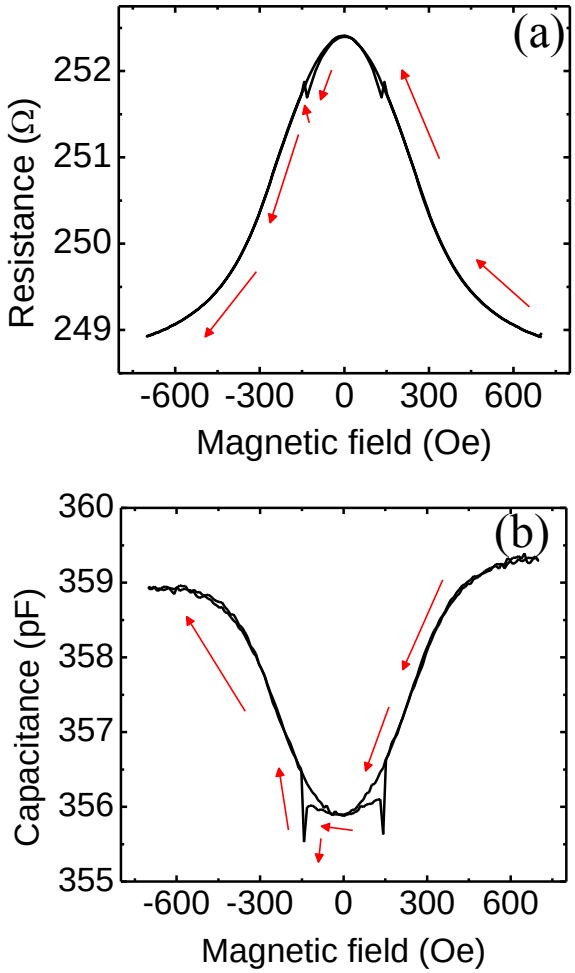

Figure 6-3: (a) Resistance of the nanowire under ac-impedance measurements across P_1P_2. (b) Capacitance measurement across P_1P_2.

Interestingly, the capacitance versus magnetic field (C-H) measurements in Fig. 6-3(b) show that the magnetization states clearly affect the capacitive components, as the kink at the point of DW extinction is clearly visible in the capacitance measurements. The capacitance behavior is similar to the inverse of resistance (1/R). We can compare the ratio of MR with the following relation

$$MR = \frac{R_{max} - R_{sat}}{R_{sat}} \tag{6.1}$$

$$MC = \frac{C_{min} - C_{sat}}{C_{sat}} \tag{6.2}$$

where R_{max} and R_{sat} are the maximum resistance and saturated resistance, respectively and C_{min} and C_{sat} are the minimum capacitance and saturated capacitance, respectively. For example, the MR ratio in Fig. 6-3(a) is 1.39%, while the MC ratio in Fig. 6-3(b) is -0.89%.

6.4.1 Nanowire width dependence of magnetocapacitance

We have also studied the ratio of MR and MC in nanowires with different widths, ranging from 200 to 900 nm, as shown in Fig. 6-4. The MR and MC ratio is relatively constant around 1.45% and -0.9%, respectively, regardless of the width of nanowires. These experiments demonstrate that the capacitive response of the nanowire system can be effectively used for the detection of magnetic reversal and formation of DW.

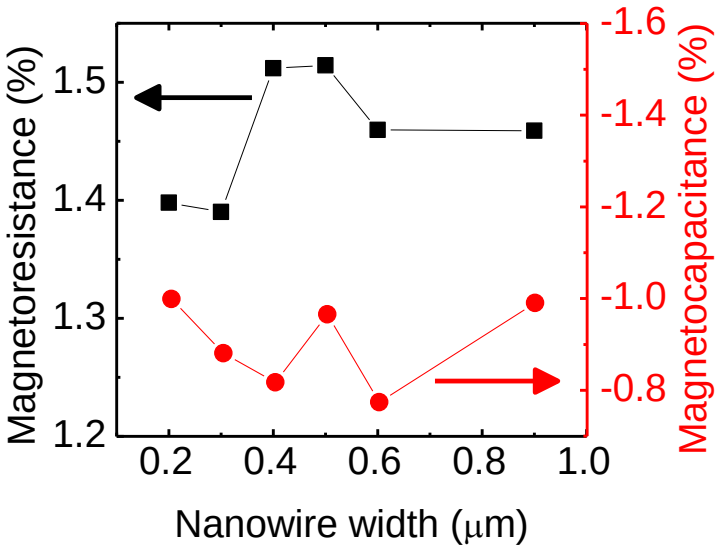

Figure 6-4: Magnetoresistance and magnetocapacitance ratio for various widths of nanowires.

6.5 Cole-cole plot

The vector locus of the resistance (R) and reactance (X) components from the impedance measurements ($Z = R + jX$) with various frequencies in the range of 50 Hz to 2 MHz show a semi-circle trajectory located in the fourth quadrant for a 600 nm wide nanowire. Absolute value of reactance is plotted in Fig. 6-5 along with the semi-circular fit at zero magnetic field. This confirms that the device behaves like a capacitive system in the measured frequency range.

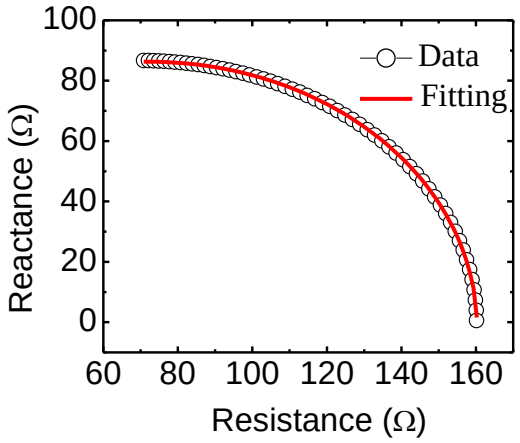

Figure 6-5: *R-X* plot for the frequency range 50 Hz – 2 MHz. The absolute *X* component is plotted with a circular fit.

6.6 Equivalent circuit model

The capacitive behavior of the nanowire system can be understood by the modified Maxwell-Wagner capacitance model [124-126]. This model states that any clustered capacitive system can be modeled by two leaky capacitors in series with one of the leakage components being magnetically tunable. In the present case, the tunable component is the resistive component which arises from AMR.

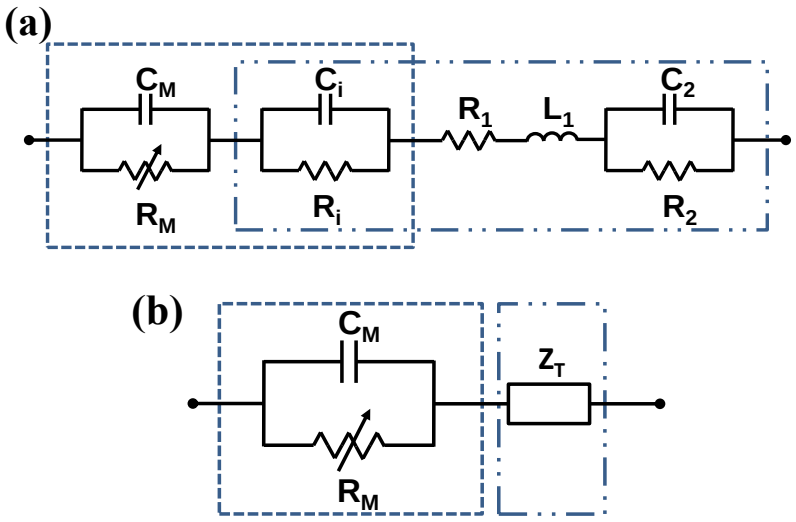

Figure 6-6: (a) Equivalent circuit for the measurement set up with two leaky capacitors representing the nanowire and the rest corresponding to the other effects arising from the coaxial line and contacts. (b) Simplified equivalent circuit with the field dependent components (C_M and R_M) and others (Z_T).

The equivalent circuit based on the Maxwell-Wagner model is shown in Fig. 6-6(a), which is divided into parts – the magnetic nanowire and the rest of the measurement path, which includes the line and contacts. The nanowire element can be described by C_M, C_i, R_M, and R_i. C_M and R_M are capacitance and resistance, respectively, which depend on magnetic field, while C_i and R_i are field independent capacitance and resistance, respectively. The contact resistance and other parasitic effects can be modeled as shown in Fig. 6-6(a) into a series resistance (R_1) with inductor (L_1) which is in series with a parallel capacitor (C_2) and resistor (R_2), where R_1, L_1, C_2, and R_2 are not sensitive to the magnetic field. In order to further quantify the MC, this equivalent circuit has been simplified into two parts; one is depending on the field and the others

are not dependent on the magnetic field. The magnetically non-dependent part can be expressed as equivalent impedance Z_T as shown in Fig. 6-6(b). The magnetically independent part can be removed by deducting the impedances at different magnetic fields mentioned above. Change in the impedance, ΔZ, can be expressed as $\Delta Z = \Delta R + j\Delta X$, where $\Delta R = R_{H=0} - R_{H=500}$, $\Delta X = X_{H=0} - X_{H=500}$.

$$\Delta R = \left(\frac{R_{M0}}{1+4\pi^2 f^2 R_{M0}{}^2 C_{M0}{}^2} - \frac{R_{Mh}}{1+4\pi^2 f^2 R_{Mh}{}^2 C_{Mh}{}^2} \right) \tag{6.3}$$

$$\Delta X = -2\pi f \left(\frac{C_{M0} R_{M0}{}^2}{1+4\pi^2 f^2 R_{M0}{}^2 C_{M0}{}^2} - \frac{C_{Mh} R_{Mh}{}^2}{1+4\pi^2 f^2 R_{Mh}{}^2 C_{Mh}{}^2} \right) \tag{6.4}$$

where R_{M0} and C_{M0} are resistance and capacitance at H = 0, respectively, and R_{Mh} and C_{Mh} are resistance and capacitance at H = 500 Oe, respectively.

Impedance spectroscopy (IS) was performed from 50 Hz to 2 MHz at two different magnetic fields, 0 and 500 Oe. Figure 6-7 show R components of the IS of a 600 nm wide nanowire at different magnetic fields. The inset shows ΔR with fits. The fitting curve can be derived by Eq. (6.3) as a function of frequency (f).

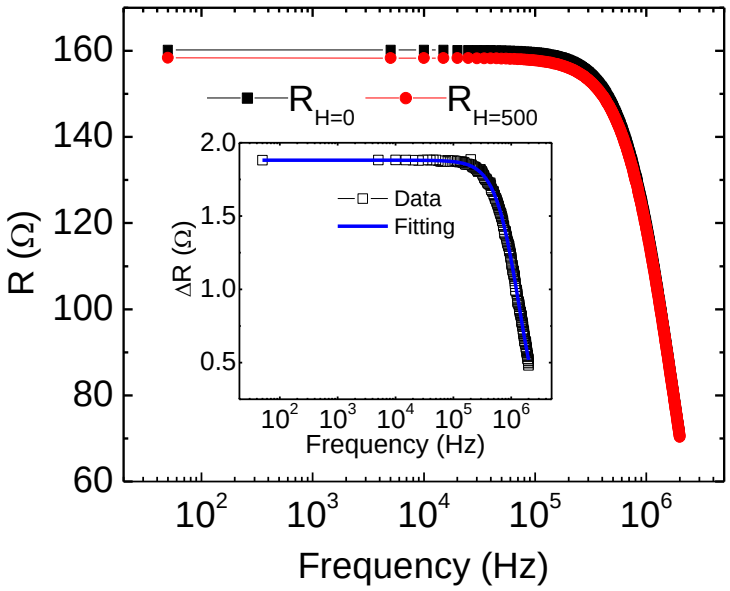

Figure 6-7: R component of impedance spectroscopy (IS) at two different magnetic fields. The insets show ΔR with fits.

Figure 6-8 show X component of the IS of the same nanowire at different magnetic fields (H = 0 and 500 Oe.). The inset shows ΔX with fits.

The fitting curves can be derived by Eq. (6.4) as a function of frequency (f). Both fittings for ΔR and ΔX give comparable fitting values as summarized in Table 6-1.

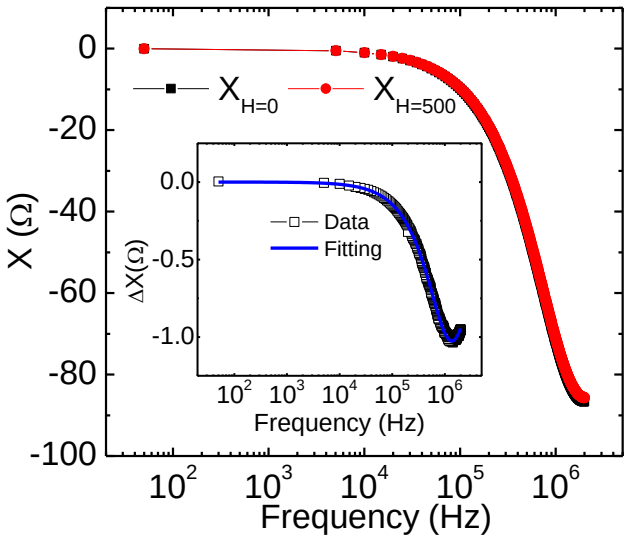

Figure 6-8: X component of impedance spectroscopy (IS) at two different magnetic fields. The insets show ΔX with fits.

	Fitting for ΔR	Fitting for ΔX
C_{M0} (nF)	558.57	562.69
C_{Mh} (nF)	562.94	567.61
R_{M0} (Ω)	159.56	160
R_{Mh} (Ω)	157.68	158.02

Table 6-1: Fitting parameters from the ΔR and ΔX.

6.7 Angular dependence of magnetocapacitance

We also study the angular dependency of the magnetocapacitance of the nanowire. The coordinate system and the angle θ used for the description are plotted in the inset of Fig. 6-9(a).

The ΔR and its corresponding ΔC are shown in Fig. 6-9(a) and (b), respectively. As the angle θ increases, MR decreases and the ratio becomes very small at 90°. However, for the MC, the ratio becomes in the opposite

sense with a higher magnitude. This feature can be implemented for magnetization reversal techniques where MR values are negligible.

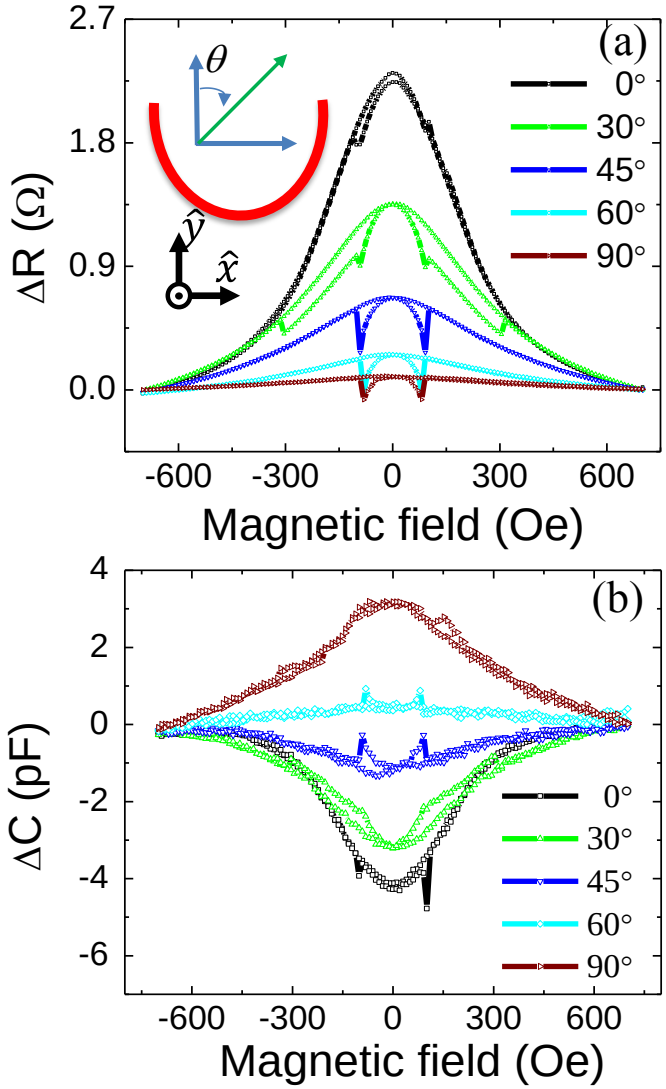

Figure 6-9: (a) Angular dependence of resistance. (b) Angular dependence of magnetocapacitance for various angles.

6.8 Magnetocapacitance in perpendicular anisotropy nanowires

To further expand the application of this capacitive detection technique for DW studies, we have also tried Co/Pd multilayers with out-of-plane magnetic anisotropy.

6.8.1 Experimental details

Nanowires were patterned with EBL followed by argon ion milling of sputter-deposited thin film having the structure of Ta (4 nm)/Ru (20 nm)/[Pd (0.7 nm)/Co (0.2 nm)]$_{22}$/Ta (4 nm) on a glass substrate. The stack structure is illustrated in Fig 6-10(a). A second photolithography step was used to define Ta (5 nm)/Cu (100 nm) contacts. The vibrating sample magnetometer (VSM) measurements show that the coercivity of the thin film is about 1 kOe as shown in Fig. 6-10(b). The anomalous Hall measurement schematics are shown in Fig. 6-10(c). Figure 6-10(d) shows the anomalous Hall signals across the C_1C_2 ports. For the applied field in the *z*-direction, the nanowire shows a square hysteresis with a coercive field of about 2 kOe at 6 K.

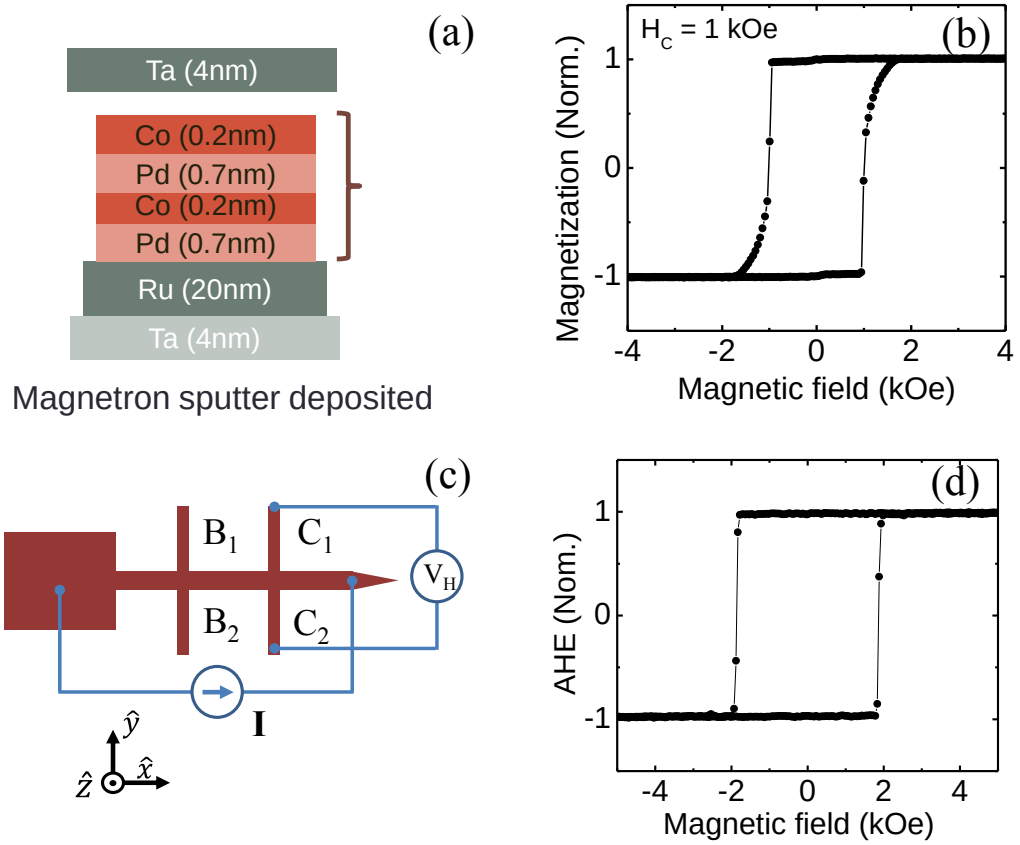

Figure 6-10: (a) Stack structure of Co/Pd multilayer film. (b) VSM measurements on Co/Pd thin film at room temperature. (c) Schematics of the measurement setup for Hall measurements. (d) Normalized anomalous Hall effect measurements at 6 K.

6.8.2 Measurement details

The schematics for the capacitance measurements are illustrated in Fig. 6-11 on the SEM image. The width of the nanowire and the Hall bar was defined to be 600 nm and the length of the nanowire is 35 µm.

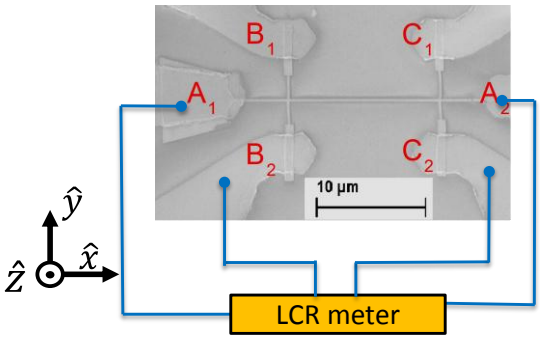

Figure 6-11: SEM image with measurement schematics for capacitance measurement.

Figure 6-12(a) shows the *R-H* measurements across B_2C_2 ports with the applied magnetic field in the *z*-direction. The MR reversal process can be understood by electron–magnon scattering processes [127, 128]. When the magnetic and anisotropy fields are antiparallel, the anisotropy field tries to maintain the magnetization direction, while the magnetic field destabilizes the magnetization, thus increasing the magnon population. Therefore, in the antiparallel case, the MR linearly increases until the magnetization is switched by the external magnetic field. When the magnetic field and the magnetization are parallel, increasing the magnetic field decreases the magnon population, therefore, the MR linearly decreases with increasing fields as can be observed. In Fig. 6-12(b) the MC measurements clearly depict the magnetization reversal process and as similar to the NiFe case, the MC measurements show an inverse trend to that of the MR measurements with the same switching fields. It is clear that the MC effect is correlated with the MR effect. The ratio of MR and MC is 0.052% and -0.017%, respectively. Even though the MC effect is small, our observation confirms that MC can be used as a tool to detect magnetization reversal not only in in-plane materials but also in out-of-plane systems.

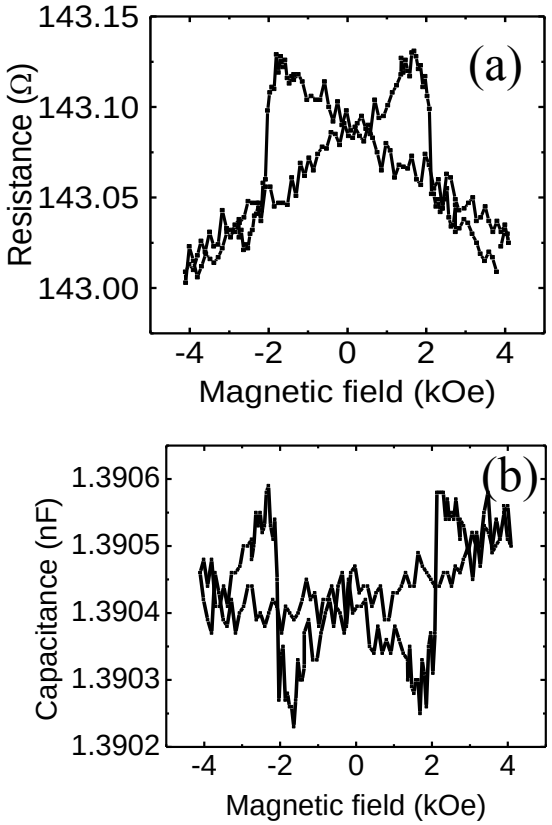

Figure 6-12: (a) Resistance of the nanowire under ac-impedance measurements across B_2C_2. (b) Capacitance across B_2C_2.

In the multiferroic systems, external magnetic field affects the magnetic ordering and due to the inherent coupling between the ferroelectric and ferromagnetic orders, the magnetic signal is reflected in the MC [117]. However, the systems we studied are metallic in nature and such effects are not possible. Moreover, spin capacitance arises due to the accumulation of spin polarized charges at the interface of metals and oxides [118]. Also, in MTJs, the interfacial capacitance is due to spin and charge accumulation, and interactions between ions at the interface [119]. Similarly, in our systems the magnetocapacitance could arise from the complex interfaces formed at the adjacent metallic boundaries.

6.9 Conclusions

We study the magnetocapacitance effect in magnetic nanowires of both in-plane and out-of-plane anisotropy systems. The C-H measurements reveal the same details of the magnetization as that of R-H measurements except that

they are in the opposite sense. Based on the Maxwell-Wagner model, we attribute the origin of the MC to the MR effect. These measurements open up the possibility of detecting magnetization reversal and an alternative method to study DW motion, especially for a system in which the resistance of nanowires is huge, resulting in the noisy resistance data, but with a sizable capacitance value.

Chapter 7 : Conclusions and future works

7.1 Conclusions

In this thesis, magnetic nanowires of both in-plane and out-of-plane are investigated for domain wall device applications. Important aspects in enabling the domain wall based devices such as domain wall generation, propagation, and detection are studied. For the case of in-plane, permalloy is studied, and for the latter CoFeB trilayer structures as well as Co/Pd multilayer structures are utilized.

The control of domain wall in nanowires is crucial for device applications. An alternative approach to pin a domain wall is investigated. The pinning sites are created by etching out a selected portion of the magnetic nanowire, thus forming a vertical nanotrench across the whole width of the nanowire in contrast to the conventional approaches with a lateral trench across the small portion of the nanowire. The experimental results in permalloy nanowire show reliable pinning and depinning behaviors from a vertical nanotrench. Also, both the vortex and transverse domain walls are observed at the nanotrench pinning sites. Analysis based on energy landscape further confirms the correlation between the dimensions of the nanotrench and the pinning potential.

An alternative method to generate DWs at predefined positions along the nanowire with the assistance of Joule heating is investigated in perpendicular anisotropy trilayers such as Pt/CoFeB/MgO and Ta/CoFeB/MgO. The nanowire coercivity (H_C) is reduced by the Joule heating, and when the assist field overcomes H_C, the part of nanowire which experiences Joule heating reverses. The statistical analysis shows that this method allows to selectively generating a DW at a predefined location in PMA nanowires with great reproducibility, which is challenging with conventional procedures based on random nucleation sites.

Magnetic domain wall induced capacitance variation is investigated as

a tool for the detection of magnetic reversal in magnetic nanowires for in-plane (NiFe) and out-of-plane (Co/Pd) magnetization configurations. The switching fields in the capacitance measurements match with that of the magnetoresistance measurements in the opposite sense. The capacitive behavior of the nanowire system is analyzed based on the modified Maxwell-Wagner capacitance model. The origin of the magnetocapacitance has been attributed to magnetoresistance. This magnetocapacitance detection technique can be useful for magnetic domain wall studies for a system in which the magnetoresistance measurements are not preferred due to a high resistance value.

The studies presented in this thesis can be extended for future works. Oscillators based on DWs are proposed for nanoscale microwave generators with possible applications in telecommunication or for rf-assisted writing in magnetic hard drives [24, 129-131]. The DW could be pinned at the demonstrated nanotrench in permalloy. With proper selection of the nanotrench dimensions, the DW can be set to oscillate between the two walls of the nanotrench and also different eigen-frequencies could be expected from these bounded oscillations. Furthermore, the nanotrench concept could be extended for PMA material systems with multilayer structures. Since the DWs in PMA systems are narrow, the notch dimensions could be controlled to very small dimensions.

Recent studies have demonstrated the electric field control of DW motion [40, 41]. The trilayer systems developed for the studies presented in the thesis could be extended for such electric field modulation on DW motion. It would be interesting to study the effect of different stack structures as well the temperature effect on the trilayer systems.

There is renewed interest in domain wall based devices following the observation of current induced spin-orbit torques in metallic systems. There have been a few studies of current induced switching experiments in the tri-layer systems where an ultra-thin magnetic layer is sandwiched between a heavy metal and an oxide layer. However, the underlying physics is still under debate. While the domain wall studies have only focused on utilizing the perpendicular anisotropy systems, the in-plane anisotropy systems have been over looked. We can study the domain wall dynamics in the presence of

various materials in in-plane systems which could help to uncover the underlying physics of the spin orbit induced effective fields. Furthermore, the spin Hall effect and the possible Rashba scenario on the DW motion could also be studied in the systems presented in chapter 5.

There have been proposals for spin capacitor as well as spin transistors [132, 133]. However, this area of research is not widely explored. The magnetocapacitance presented in the thesis could be extended for different multilayer systems. Moreover, spin capacitance could be also studied in such systems with metallic interfaces. It would be interesting to study the interfacial spin capacitance in metallic interfaces which could open up new areas of research.

References

[1] B. Dieny *et al.*, Phys. Rev. B. **43**, 1297 (1991).
[2] S. S. P. Parkin, N. More, and K. P. Roche, Phys. Rev. Lett. **64**, 2304 (1990).
[3] M. N. Baibich *et al.*, Phys. Rev. Lett. **61**, 2472 (1988).
[4] S. Parkin *et al.*, Proc. IEEE **91**, 661 (2003).
[5] S. Yuasa *et al.*, Nat. Mater. **3**, 868 (2004).
[6] J. S. Moodera *et al.*, Phys. Rev. Lett. **74**, 3273 (1995).
[7] S. S. Parkin, M. Hayashi, and L. Thomas, Science **320**, 190 (2008).
[8] D. A. Allwood *et al.*, Science **309**, 1688 (2005).
[9] M. Hayashi *et al.*, Science **320**, 209 (2008).
[10] E. Saitoh *et al.*, Nature **432**, 203 (2004).
[11] T. Koyama *et al.*, Nat. Mater. **10**, 194 (2011).
[12] I. M. Miron *et al.*, Nat. Mater. **10**, 419 (2011).
[13] E. Martinez, J. Appl. Phys. **111**, 07d302 (2012).
[14] L. Q. Liu *et al.*, Science **336**, 555 (2012).
[15] G. S. Beach *et al.*, Nat. Mater. **4**, 741 (2005).
[16] L. Thomas *et al.*, IEEE IEDM **24**, 21 (2011).
[17] A. J. Annunziata *et al.*, IEEE IEDM **24**, 31 (2011).
[18] H. P. Trinh *et al.*, IEEE T. Circuits-I **60**, 1469 (2013).
[19] R. Schafer, and A. Hubert, J. Phys. IV **8**, 283 (1998).
[20] J. H. Vanvleck, Rev. Mod. Phys. **17**, 27 (1945).
[21] H. Kronmüller, and M. Fähnle, *Micromagnetism and the microstructure of ferromagnetic solids* (Cambridge University Press, New York, 2003), pp. xv.
[22] Y. K. Kim, and T. J. Silva, Appl. Phys. Lett. **68**, 2885 (1996).
[23] J. Miltat, G. Albuquerque, and A. Thiaville, Spin Dynamics in Confined Magnetic Structures I **83**, 1 (2002).
[24] T. L. Gilbert, IEEE. T. Magn. **40**, 3443 (2004).
[25] B. Hillebrands, and A. Thiaville, *Spin dynamics in confined magnetic structures III* (Springer, Berlin ; New York, 2006), pp. xiv.
[26] S. Ladak *et al.*, New J. Phys. **14**, 045010 (2012).
[27] R. D. McMichael, and M. J. Donahue, IEEE T. Magn. **33**, 4167 (1997).
[28] M. Hayashi *et al.*, Phy. Rev. Lett. **97**, 207205 (2006).
[29] N. Wiese *et al.*, Europhys. Lett. **80**, 57003 (2007).
[30] Z. Li, and S. Zhang, Phys. Rev. Lett. **92**, 207203 (2004).
[31] A. Thiaville *et al.*, Europhys. Lett. **69**, 990 (2005).
[32] M. Tsoi, R. E. Fontana, and S. S. P. Parkin, Appl. Phys. Lett. **83**, 2617 (2003).
[33] J. Grollier *et al.*, Appl. Phys. Lett. **83**, 509 (2003).
[34] C. K. Lim *et al.*, Appl. Phys. Lett. **84**, 2820 (2004).
[35] T. Ono *et al.*, Science **284**, 468 (1999).
[36] M. Jamali, K. J. Lee, and H. Yang, New J. Phys. **14**, 033010 (2012).
[37] H. Kronmüller, and S. S. P. Parkin, *Handbook of magnetism and advanced magnetic materials* (John Wiley & Sons, Hoboken, NJ, 2007).
[38] M. Klaui *et al.*, Phys. Rev. Lett. **94**, 106601 (2005).
[39] T. Koyama *et al.*, Appl. Phys. Lett. **98**, 192509 (2011).
[40] A. M. Sahadevan *et al.*, Phys. Rev. B. **87**, 014425 (2013).
[41] A. J. Schellekens *et al.*, Nat. Commun. **3**, 847 (2012).
[42] D. Chiba *et al.*, Nat. Commun. **3**, 888 (2012).
[43] U. Bauer, S. Emori, and G. S. D. Beach, Appl. Phys. Lett. **100**, 192408 (2012).
[44] U. Bauer, S. Emori, and G. S. D. Beach, Nat. Nanotechnol. **8**, 411 (2013).
[45] I. M. Miron *et al.*, Nat. Mater. **9**, 230 (2010).

[46] T. Suzuki *et al.*, Appl. Phys. Lett. **98**, 142505 (2011).
[47] J. Kim *et al.*, Nat. Mater. **12**, 240 (2013).
[48] L. Q. Liu *et al.*, Phys. Rev. Lett. **109**, 096602 (2012).
[49] K. S. Ryu *et al.*, Nat. Nanotechnol. **8**, 527 (2013).
[50] S. Emori *et al.*, Nat. Mater. **12**, 611 (2013).
[51] A. Brataas, Nat. Nanotechnol. **8**, 485 (2013).
[52] *Please refer to http://math.nist.gov/oommf/*.
[53] T. Gerhardt, A. Drews, and G. Meier, J. Phys-Condens. Mat. **24**, 024208 (2012).
[54] E. Schlömann, J. Appl. Phys. **44**, 1837 (1973).
[55] E. Martinez, J. Phys-Condens. Mat. **24**, 024206 (2012).
[56] D. E. Harrison, Phys. Rev. **102**, 1473 (1956).
[57] Please refer to http://www.arzuffisrl.it/sputtering.htm.
[58] X. P. Qiu *et al.*, AIP Adv. **2**, 032121 (2012).
[59] Please refer to http://www.ajaint.com/.
[60] Please refer to http://www.suss.com.
[61] Please refer to http://www.azem.com/en/Products/Litho-technology/Photoresist%20Developers.aspx.
[62] M. Altissimo, Biomicrofluidics **4**, 026503 (2010).
[63] Please refer to http://www.raith.com.
[64] Please refer to http://www.ionbeammilling.com/about_the_ion_milling_process.
[65] Please refer to http://blog.brukerafmprobes.com/category/guide-to-spm-and-afm-modes/.
[66] D. Lacour *et al.*, Appl. Phys. Lett. **84**, 1910 (2004).
[67] M. Seifert *et al.*, J. Phys. D: Appl. Phys. **45**, 175001 (2012).
[68] Please refer to http://hyperphysics.phy-astr.gsu.edu/hbase/solids/squid.html.
[69] http://www.qdusa.com/.
[70] J. Yang *et al.*, Phys. Rev. B. **77**, 014413 (2008).
[71] L. Thomas *et al.*, Science **315**, 1553 (2007).
[72] D. McGrouther *et al.*, Appl. Phys. Lett. **91**, 022506 (2007).
[73] M. Hayashi *et al.*, Phy. Rev.Lett. **97**, 207205 (2006).
[74] G. Meier *et al.*, Phys. Rev. Lett. **98**, 187202 (2007).
[75] L. Thomas *et al.*, Appl. Phys. Lett. **87**, 262501 (2005).
[76] T. J. Silva *et al.*, Phys. Rev. Lett. **85**, 7849 (1999).
[77] J. C. Mallinson, *The foundations of magnetic recording* (Academic Press, Boston, 1993), pp. xv.
[78] H. Tanigawa *et al.*, Appl. Phys. Express **1**, 011301 (2008).
[79] S. S. P. Parkin, M. Hayashi, and L. Thomas, Science **320**, 190 (2008).
[80] A. Yamaguchi *et al.*, Phys. Rev. Lett. **92**, 077205 (2004).
[81] D. A. Allwood, G. Xiong, and R. P. Cowburn, Appl. Phys. Lett. **85**, 2848 (2004).
[82] L. K. Bogart *et al.*, Phys. Rev. B. **79**, 054414 (2009).
[83] M. Jamali, H. Yang, and K. J. Lee, Appl. Phys. Lett. **96**, 242501 (2010).
[84] M. Y. Im *et al.*, J. Phys-Condens. Mat. **24**, 024203 (2012).
[85] A. Kunz, and J. D. Priem, IEEE T. Magn. **46**, 1559 (2010).
[86] A. Vogel *et al.*, Appl. Phys. Lett. **98**, 202501 (2011).
[87] M. A. Basith *et al.*, Appl. Phys. Lett. **100**, 232402 (2012).
[88] M. Klaui *et al.*, Phys. Rev. Lett. **90**, 097202 (2003).
[89] M. Klaui, J. Phys-Condens. Mat. **20**, 313001 (2008).
[90] M. Hayashi *et al.*, Nat. Phys. **3**, 21 (2007).
[91] F. U. Stein *et al.*, Appl. Phys. Lett. **100**, 192403 (2012).
[92] M. Munoz, and J. L. Prieto, Nat. Commun. **2**, 562 (2011).
[93] X. Jiang *et al.*, Nat. Commun. **1**, 25 (2010).
[94] M. Kläui *et al.*, Appl. Phys. Lett. **87**, 2042542 (2005).

[95] I. M. Miron *et al.*, Nat. Mater. **10**, 419 (2011).
[96] D. Backes *et al.*, Appl. Phys. Lett. **91**, 112502 (2007).
[97] J. Kim *et al.*, Nat. Mater. **12**, 240 (2013).
[98] L. Liu *et al.*, Phys. Rev. Lett. **109**, 096602 (2012).
[99] S. Emori, and G. S. D. Beach, Appl. Phys. Lett. **98**, 132508 (2011).
[100] F. Cayssol *et al.*, Phys. Rev. Lett. **92**, 107202 (2004).
[101] N. Ohshima *et al.*, J. Phys-Condens. Mat. **23**, 382202 (2011).
[102] M. Hayashi *et al.*, Appl. Phys. Lett. **100**, 192411 (2012).
[103] J. H. Franken, H. J. M. Swagten, and B. Koopmans, Nat. Nanotechnol. **7**, 499 (2012).
[104] I. L. Prejbeanu *et al.*, J. Phys-Condens. Mat. **19**, 165218 (2007).
[105] K. Yagami *et al.*, IEEE T. Magn. **41**, 2615 (2005).
[106] R. E. Rottmayer *et al.*, IEEE T. Magn. **42**, 2417 (2006).
[107] T. Moriyama *et al.*, Appl. Phys. Lett. **90**, 152503 (2007).
[108] J. P. Attane *et al.*, Phys. Rev. Lett. **96**, 147204 (2006).
[109] D. Ravelosona *et al.*, Phys. Rev. Lett. **95**, 117203 (2005).
[110] M. Hayashi, Y. K. Takahashi, and S. Mitani, Appl. Phys. Lett. **101**, 172406 (2012).
[111] L. Pan, and D. B. Bogy, Nat. Photonics **3**, 186 (2009).
[112] M. P. Sharrock, J. Appl. Phys. **76**, 6413 (1994).
[113] K. J. Kim *et al.*, Appl. Phys. Lett. **92**, 192509 (2008).
[114] H. Sato *et al.*, IEEE Magn. Lett **3**, 3000204 (2012).
[115] M. Yamanouchi *et al.*, IEEE Magn. Lett **2**, 3000304 (2011).
[116] S. H. Chung *et al.*, Phys. Rev. B. **81**, 024410 (2010).
[117] T. Kimura *et al.*, Phys. Rev. B. **67**, 180401 (2003).
[118] J. M. Rondinelli, M. Stengel, and N. A. Spaldin, Nat. Nanotechnol. **3**, 46 (2008).
[119] H. Kaiju *et al.*, J. Appl. Phys. **91**, 7430 (2002).
[120] P. Padhan *et al.*, Appl. Phys. Lett. **90**, 142105 (2007).
[121] Y. M. Chang *et al.*, J. Appl. Phys. **107**, 093904 (2010).
[122] A. M. Sahadevan *et al.*, Appl. Phys. Lett. **101**, 162404 (2012).
[123] T. Taniyama *et al.*, Phys. Rev. Lett. **82**, 2780 (1999).
[124] G. Catalan, Appl. Phys. Lett. **88**, 102902 (2006).
[125] W. C. Chien *et al.*, J. Appl. Phys. **105**, 033915 (2009).
[126] W. C. Chien *et al.*, IEEE T. Magn. **42**, 2624 (2006).
[127] A. P. Mihai *et al.*, Phys. Rev. B. **77**, 060401 (2008).
[128] V. D. Nguyen *et al.*, Phys. Rev. Lett. **107**, 136605 (2011).
[129] E. Martinez, L. Torres, and L. Lopez-Diaz, Phys. Rev. B. **83**, 174444 (2011).
[130] T. Ono, and Y. Nakatani, Appl. Phys. Express **1**, 061301 (2008).
[131] M. Jamali *et al.*, Appl. Phys. Lett. **101**, 062401 (2012).
[132] S. Datta, Appl. Phys. Lett. **87**, 013115 (2005).
[133] R. Ramesh, Nat. Nanotechnol. **3**, 7 (2008).

Publications

- **Kulothungasagaran Narayanapillai** and Hyunsoo Yang, "*Control of domain wall motion at vertically etched nanotrench in ferromagnetic nanowires*", Applied Physics Letters **103**, 252401 (2013).
- **Kulothungasagaran Narayanapillai**, Jan Rhensius, Qiu Xuepeng, and Hyunsoo Yang, "*Thermally assisted domain wall nucleation in perpendicular anisotropy trilayer nanowires*", Journal of Physics D: Applied Physics (accepted).
- Mahdi Jamali*, **Kulothungasagaran Narayanapillai***, Xuepeng Qiu, Li Ming Loong, Aurelien Manchon, and Hyunsoo Yang, "*Spin-orbit torques in Co/Pd multilayer nanowires*", Physical Review Letters **111**, 246602 (2013).
- **Kulothungasagaran Narayanapillai**, Mahdi Jamali, and Hyunsoo Yang, "*Observation of magnetocapacitance in ferromagnetic nanowires*", Applied Physics Letters **101**, 052401 (2012).
- Xuepeng Qiu, **Kulothungasagaran Narayanapillai**, Yang Wu, Praveen Deorani, Xinmao Yin, Andrivo Rusydi, Kyung-Jin Lee, Hyun-Woo Lee, Hyunsoo Yang, "*A new route to spin-orbit torque engineering via oxygen manipulation*", arXiv:1311.3032 (2013).
- Mahdi Jamali, Jae Hyun Kwon, **Kulothungasagaran Narayanapillai**, and Hyunsoo Yang, "*Detection of domain wall eigenfrequency in infinity-shaped magnetic nanostructures*", Applied Physics Letters **101**, 062401 (2012).
- Xue Peng Qiu, Young Jun Shin, Jing Niu, **Narayanapillai Kulothungasagaran**, Gopinadhan Kalon, Caiyu Qiu, Ting Yu, and Hyunsoo Yang, "*Disorder-free sputtering method on graphene*", AIP Advances **2**, 032121 (2012).
- Young Jun Shin, Gopinadhan Kalon, **Kulothungasagaran Narayanapillai**, Alan Kalitsov, Charanjit Singh Bhatia and Hyunsoo Yang, "*Stochastic nonlinear electrical characteristics of graphene*", Applied Physics Letters, **102**, 033101, (2013).